Okinawa Institute of Science and Technology
Graduate University

Thesis submitted for the degree

Doctor of Philosophy

Coherent control of charged particle systems strongly interacting with microwave photons

by

Jiabao Chen

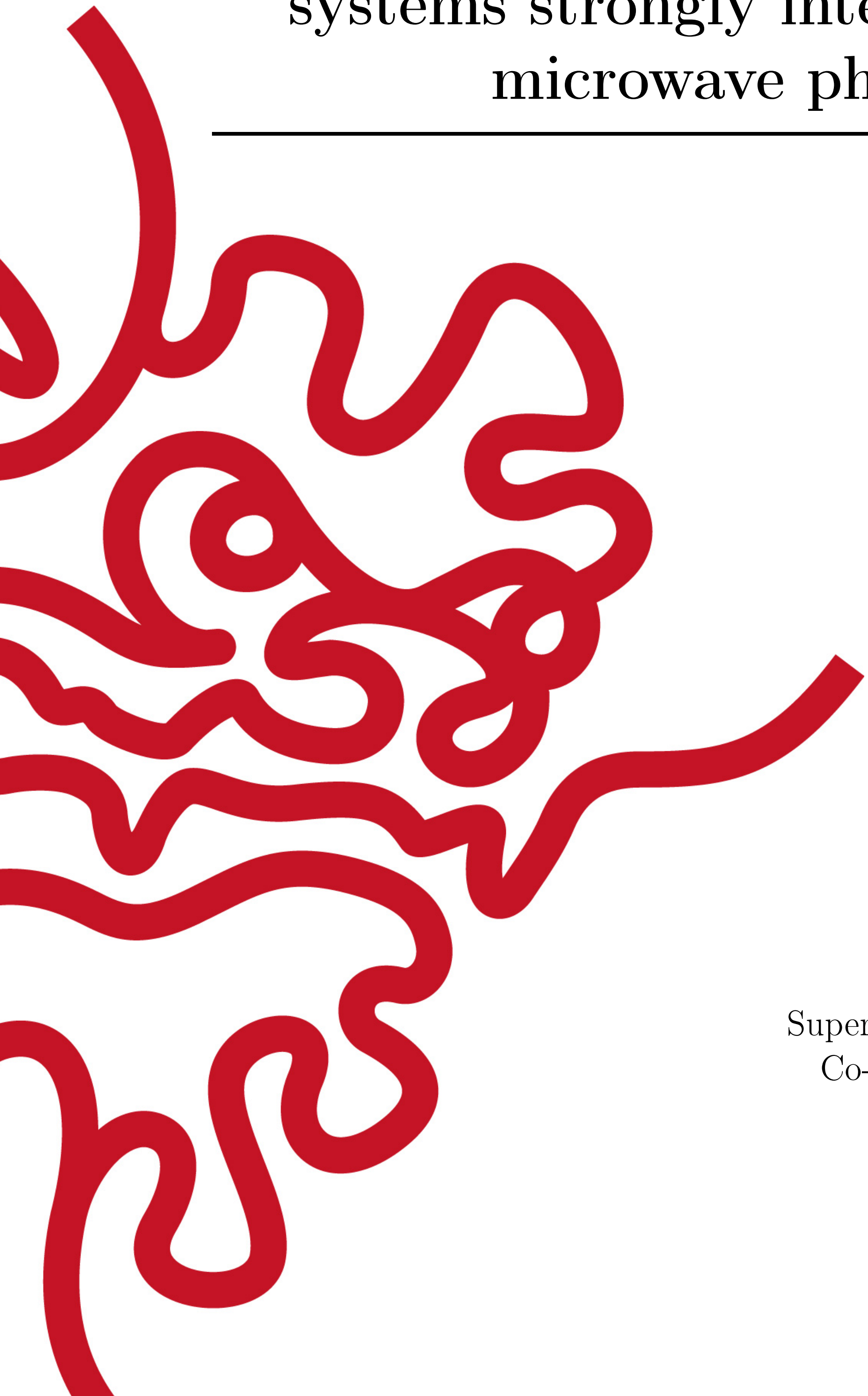

Supervisor: **Denis Konstantinov**
Co-Supervisor: **Thomas Busch**

August, 2019

Declaration of Original and Sole Authorship

I, Jiabao Chen, declare that this thesis entitled *Coherent control of charged particle systems strongly interacting with microwave photons* and the data presented in it are original and my own work.

I confirm that:

- No part of this work has previously been submitted for a degree at this or any other university.
- References to the work of others have been clearly acknowledged. Quotations from the work of others have been clearly indicated, and attributed to them.
- In cases where others have contributed to part of this work, such contribution has been clearly acknowledged and distinguished from my own work.
- None of this work has been previously published elsewhere, with the exception of the following:

  1) Jiabao Chen, A. A. Zadorozhko, and Denis Konstantinov. "Strong coupling of a two-dimensional electron ensemble to a single-mode cavity resonator." Physical Review B 98.23 (2018): 235418.

  2) Jiabao Chen, Denis Konstantinov, and Klaus Mølmer. "Adiabatic preparation of squeezed states of oscillators and large spin systems coupled to a two-level system." Physical Review A 99.1 (2019): 013803.

Date: June, 2019
Signature:

Jiabao Chen

Abstract

Coherent control of charged particle systems strongly interacting with microwave photons

Coherent control of charged particle systems using electromagnetic field is an exciting area of research that can lead to new elements for quantum technologies. However, the choice of a suitable system to realize such applications is limited because of the often unavoidable presence of dissipation and decoherence. One condensed matter system where these problems are minimised is the system of surface electrons on liquid helium. This thesis aims to contribute to achieving coherent control of the quantum states of orbital motion of electrons on helium using quantized electromagnetic field in an optical resonator. In particular, I have studied the strong coupling regime of interaction between the cyclotron motion of electrons and the microwave photons in a Fabry-Perot resonator and provided a detailed analysis of experiments carried out in the Quantum Dynamics Unit at OIST using both classical and quantum formalisms. The agreement between both formalisms demonstrated the mean-value nature of the observed normal mode splitting phenomenon. As a theoretical proposal, I have studied the generation of squeezed states and spin-squeezed states of a harmonic oscillator and of an ensembles of two-level-systems, respectively, which is strongly coupled to a two-level system. In this work I will discuss a special case of the Jaynes-Cummings model driven by an external field and its analogue in which a two-level system is coupled to a collective large spin. This can be seen as a relevant proposal for electrons on helium with coupling between their cyclotron motion and the surface-bound states. Finally, I have studied the surface electrons on helium with a coupling introduced by an in-plane magnetic field. I have shown that this leads to a renormalization of the energy spectrum of coupled orbital motion and have made a number of predictions which were confirmed in a subsequent experiment. This work therefore opens doors to explore the physics in the strong coupling regime between the electrons' surface-bound states and photons in microwave resonators.

Acknowledgment

I am grateful that I can work among so many wonderful people during the years of my graduate study. Firstly, I would like to express my sincere gratitude to my PhD supervisor Prof. **Denis Konstantinov** for the knowledge, support, patience, and kind guidance. He have shown me how to be a good physicist and made rooms for me to learn from mistakes. I would also like to thank my co-supervisor Prof. **Thomas Busch** who gave me insightful advice in the research, career and etc. In plenty different aspects, they helped me learn and grow a lot.

Next, my gratitude goes to Prof. **Klaus Mølmer** in Aarhus University for hosting me as a visiting PhD student and sharing his profound insights in physics. Our work during this visit is part of this thesis.

I thank Dr. **Oleksiy Zadorozhko** for his excellent works in the experiments. I would also like to thank my colleagues in the *Quantum Dynamics Unit*, the *Quantum System Unit* in OIST and the *Mølmer Group* in Aarhus University for many meaningful discussions and joy.

I thank Prof. **David Dorfan** for giving me advice and encouragement to pursuit my passion in physics at the beginning of my PhD. I would also like to thank my friends in Okinawa and Aarhus, who made this long journey truly unforgettable. Last but not the least, I would like to thank my parents for their kind supports throughout the years.

Finally, my gratitude goes to OIST, for making these possible.

Abbreviations

2DEG	two-dimensional electron gas
2DES	two-dimensional electron systems
AMO	Atomic, Molecular, and Optical physics
CP	Circularly Polarized
CR	Cyclotron Resonance
CSS	Coherent Spin State
EM	ElectroMagnetism
FB	Fabry-Pérot
JCM	Jaynes-Cummings model
HO	Harmonic Oscillator
LHCP	Left-Hand-Circularly-Polarized
QED	Quantum ElectroDynamics
cQED	cavity Quantum ElectroDynamics
QDs	Quantum Dots
LLs	Landau Levels
MOSFET	Metal Oxide Semi-conductor Field Effect Transistor
MW	MicroWave
RHCP	Right-Hand-Circularly-Polarized
RWA	Rotating Wave Approximation
SE	Surface State Electrons
TEM	Transverse Electro-Magnetic
TLS	Two Level Systems

Nomenclature

c	Speed of light ($2.997\ 924\ 58 \times 10^{8}$ ms^{-1})
h	Planck constant ($6.626\ 070\ 04 \times 10^{-34}$ Js)
$\hbar$	Reduced Planck constant ($1.054\ 572\ 66 \times 10^{-34}$ Js)
k_B	Boltzmann constant ($1.380\ 658 \times 10^{-23}$ JK^{-1})
Z_0	Impedance of free space ($376.730\ 313\ 461\ \Omega$)
μ_0	Permeability of free-space ($4\pi \times 10^{-7}$ Hm^{-1})
ϵ_0	Permittivity of free-space ($8.854\ 187\ 82\mathrm{F}m^{-1}$)

License and copy right information

The work contained in this thesis includes materials that have been published elsewhere. Notably, Chapters 1 and 2 include figures and text that are published in adapted and original form in the American Physical Society's journal Physical Review B and Physical Review A respectively. Copyright permission has been granted for use of these figures, and for brevity the copyright notice is given here.

Chapter 1. Reprinted excerpts and figures with permission from Jiabao Chen, A. A. Zadorozhko, and Denis Konstantinov. "Strong coupling of a two-dimensional electron ensemble to a single-mode cavity resonator." Physical Review B 98.23 (2018): 235418. Copyright (2018) by the American Physical Society.

Chapter 2. Reprinted excerpts and figures with permission from Jiabao Chen, Denis Konstantinov, and Klaus Mølmer. "Adiabatic preparation of squeezed states of oscillators and large spin systems coupled to a two-level system." Physical Review A 99.1 (2019): 013803. Copyright (2109) by the American Physical Society.

Contents

Introduction

Highly controllable synthetic quantum systems designed from the bottom up have been an active and exciting area of research in the recent decades. In these systems, the interaction between different components can often be precisely controlled by the experimentalist. By performing experiments with such systems, we can deepen our understanding towards, for example, light-matter interactions, quantum entanglement, many body physics, and unconventional phases of matter. This is not only interesting from the fundamental physics' point of view, but can also lead to applications based on the principles of quantum mechanics.

Being able to prepare and manipulate quantum states beyond the time scale of dissipation and decoherence is crucial for the development of many real-world quantum applications. This includes but is not limited to quantum computing[1–3] and quantum communication [4], quantum entanglement enhanced metrology[5–7], quantum simulations [8–11], etc. Coherent control of quantum states can be implemented in a wide variety of physical systems. In earlier years, researchers have realized it in cold atoms and ions [12–16], superconducting circuits [17, 18], semiconductor quantum dots (QDs) [19] and nano-mechanical structures [20]. In recent years, hybrid quantum systems which combine, for example, microscopic atomic systems with solid-state quantum devices, have been of considerable interest[21–24, 24, 25].

In addition to the synthetic quantum systems mentioned above, some condensed matter systems which were traditionally used to study other phenomena, have been introduced into this field of study. In particular, the surface electrons (SEs) on liquid helium, the first two-dimensional electron system (2DES) realized in the laboratory environment, has been discussed recently in the context of quantum information [26–29]. This system gains attention because of its extreme purity, thus long coherence time, as well as convenience to manipulate charged particles using an electrostatic field. Therefore, it is an attractive idea to apply some theoretical models and experimental methods similar to ones, for example, used for the Rydberg atoms or spins in QDs, to SEs on liquid helium. However, while the governing principles are universal for different systems, it is still a non-trivial task to implement the same ideas in different physical systems because they differ greatly in energy scales, interaction strength, noise levels and available experimental methods which can be applied to them.

This thesis aims at contributing to achieving coherent control of charged particle states in the electrons-on-helium system. In particular, we are interested in the coupling of the states of electron orbital motion to an optical resonator and control of this states using light. In this work, we are inspired by the cavity Quantum Electrodynamics (cQED) approach which uses the regime of strong coupling between, on the one hand, an atom or an ensemble of atoms and, on the other hand, the electromagnetic (EM) field of a cavity mode. Our purpose is to establish some basic experimental techniques for this kind of experiments, as well as to formulate necessary theoretical models for their adequate description. In addition, we consider some abstract theoretical models which potentially can be realized in the electrons-on-helium system.

In the following, we will introduce the basic physics behind 2DES formed on the surface of liquid helium and, in particular, emphasize some similarities of this system with Rydberg atoms.

Electrons hovering above liquid helium

SEs on the free surface of liquid helium were theoretically introduced by Cole and Cohen [30, 31] and, independently, by Shikin[32]. Soon after that, SEs were detected in an experiment by Sommer and Tanner [33]. Such electrons are trapped near the surface of a liquid by, on the one hand, an attractive potential from an 'image charge' under the surface due to the weak polarizability of helium atoms which constitute the liquid and, on the other hand, a potential barrier at the vapor-liquid interface due to hard-core repulsion from the helium atoms, see Fig. 1. According to quantum mechanical principles, this allows such an electron to hover above the surface of liquid helium at a distance of $\langle z \rangle \sim 10$ nm, thus forming a two-dimensional (2D) electron system.

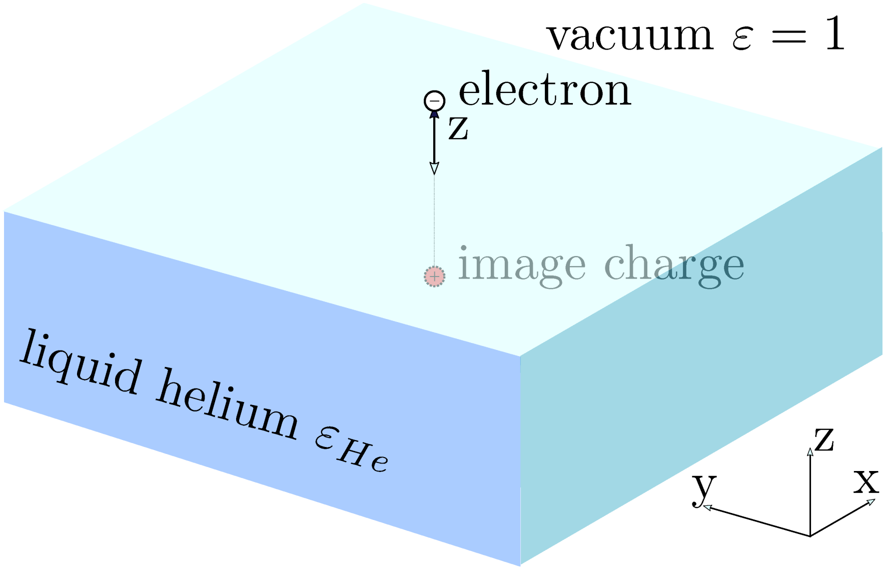

Figure 1: An electron above liquid helium

The basic quantum-mechanical Hamiltonian of a single electron above liquid helium is given by

$$H = \frac{\boldsymbol{p}^2}{2m_e} + V(\boldsymbol{r}). \tag{1}$$

where m_e is the bare electron mass. Assuming an infinitely extended flat surface of liquid helium, the potential energy of electron reads

$$V(z) = V_0\Theta(-z) - \frac{\Lambda}{z}\Theta(z), \tag{2}$$

where $V_0 \sim 1$ eV is the height of repulsive potential barrier at the vapor-liquid interface, $\Theta(z)$ is the Heaviside (step) function, and

$$\Lambda = \left(\frac{1}{4\pi\epsilon_0}\right)\left(\frac{e^2}{4}\right)\left(\frac{\epsilon_{\mathrm{He}} - 1}{\epsilon_{\mathrm{He}} + 1}\right). \tag{3}$$

Here, the Coulomb constant Λ describes the image charge in the liquid and is determined by the dielectric constant of liquid helium ϵ_{He}. The total Hamiltonian H can be separated into two parts, $H = H_z \otimes 1 + 1 \otimes H_{xy}$, which describe the orbital motion of electron in the direction perpendicular to the surface (H_z) and parallel to the surface (H_{xy}). In the z direction, the electron motion is quantized into the surface bound states, which are the eigenstates $|n\rangle$ of the Hamiltonian

$$\begin{aligned} H_z &= \frac{p_z^2}{2m_e} + V_0\Theta(-z) - \frac{\Lambda}{z}\Theta(z) \\ &= \sum E_n \, |n\rangle\langle n| \, . \end{aligned} \tag{4}$$

The energy spectrum of this motion can be easily found by making some reasonable approximations. By assuming a rigid-wall repulsive barrier at the surface, that is $V_0 \to +\infty$, the eigenfunctions $\chi_n(z) = \langle z|n\rangle$ and corresponding energy eigenvalues E_n are obtained from a simple differential equation

$$\left[-\frac{\hbar^2}{2m_e}\frac{\partial^2}{\partial z^2} - \frac{\Lambda}{z} - E_n\right]\chi_n(z) = 0, \tag{5}$$

with the boundary condition $\chi_n(z = 0) = 0$. It is clear that this equation is identical to that for the radial part of the eigenfunction (multiplied by r) of an electron with the orbital quantum number $\ell = 0$ in the hydrogen atom. Thus, we can immediately write the energy eigenvalues in the form

$$E_n = -\frac{m_e\Lambda^2}{2\hbar^2}\frac{1}{n^2} = -\frac{E_{\mathrm{r}}}{n^2}, \quad n = 1, 2, 3, \ldots, \tag{6}$$

where we introduce the effective Rydberg constant $E_{\mathrm{r}} = m_e\Lambda/(2\hbar^2)$. For liquid helium, the dielectric constant ϵ_{He} is close to unity due to the very weak polarizability of the helium atoms. Therefore, the effective Rydberg constant for electrons on helium is much smaller than the Rydberg constant for electrons in the hydrogen atoms. For two isotopes of helium, ^{3}He and ^{4}He, the values of E_{r} are given in Table 3.

The wavefuctions which satisfy the eigenvalue equation (5) are given by the well known expressions identical to those for electron in the hydrogen atom, e.g. the wave-

	^{3}He	^{4}He
Dielectric constant ϵ_{He}	1.042	1.056
Bohr radius r_{B}	10.3 nm	7.8 nm
Average distance $\langle z \rangle$	15.4 nm	11.6 nm
Rydberg constant E_{r}	36 meV (4 K)	63 meV (8 K)
$n = 1 \to 2$ transition frequency f_{12}	65 GHz	114 GHz
$n = 1 \to 2$ transition moment z_{12}	6.2 nm	4.7 nm

Table 3: The estimated effective Bohr radius, the average distance $\langle 1 | z | 1 \rangle$ from an electron in the ground state to the surface, the effective Rydberg constant, the $n = 1 \to 2$ transition frequency $f_{12} = (E_2 - E_1)/h$ and the $n = 1 \to 2$ transition moment, $\langle 1 | z | 2 \rangle$, for SE on liquid ^{3}He and ^{4}He.

functions for the two lowest eigenstates are given by

$$\begin{aligned} \chi_1(z) &= \frac{2}{a_{\mathrm{B}}^{3/2}} z \exp\left(-\frac{z}{a_{\mathrm{B}}}\right), \\ \chi_2(z) &= \frac{1}{2a_{\mathrm{B}}^{3/2}} z \left(1 - \frac{z}{2a_{\mathrm{B}}}\right) \exp\left(-\frac{z}{2a_{\mathrm{B}}}\right), \end{aligned} \tag{7}$$

where

$$r_{\mathrm{B}} = \frac{\hbar^2}{m_e \Lambda}, \tag{8}$$

is the effective Bohr radius. Again, because the dielectric constant of liquid helium is close to unity, the effective Bohr radius for electrons on helium is about two orders of magnitude larger than that for electron in Hydrogen atoms. The corresponding values for ^{3}He and ^{4}He are given in Table 3. The energy eigenvalues and probability densities $|\chi_n|^2$ for SE on liquid ^{3}He are plotted in Fig. 2.

The radiation-induced transitions between eigenstates $|n\rangle$, which we usually call the Rydberg states of SEs, were first directly observed by Grimes and Brown for electrons on ^{4}He [34]. For the resonant $n = 1 \to 2$ transition, they measured the transition frequency of about 126 GHz, which is somewhat larger than predicted by the approximate model described above, see Table 3. Similar disagreement was fond later for SEs on liquid ^{3}He [35]. Most likely, the disagreement comes from approximating a finite potential barrier $V_0 \sim 1$ eV by the rigid-wall potential.

Usually, the motion of electrons in the z direction is independent from their in-plane motion, thus each Rydberg state $|n\rangle$ is infinitely degenerate. In case of a simple Hamiltonian (1), the eigenstates of the total orbital motion of SE are the products $|n\rangle\,|p_x, p_y\rangle$, where $\langle \boldsymbol{r} | p_x, p_y \rangle = (2\pi\hbar)^{-1} \exp\left(-\mathrm{i}(p_x x + p_y y)/\hbar\right)$. The in-plane motion of SE can be quantized by applying a sufficiently strong magnetic field perpendicular to the liquid surface. This situation is one of the main subjects of this thesis, therefore I would postpone the detailed discussion of SEs subject to magnetic fields until Chapters 1 and 3.

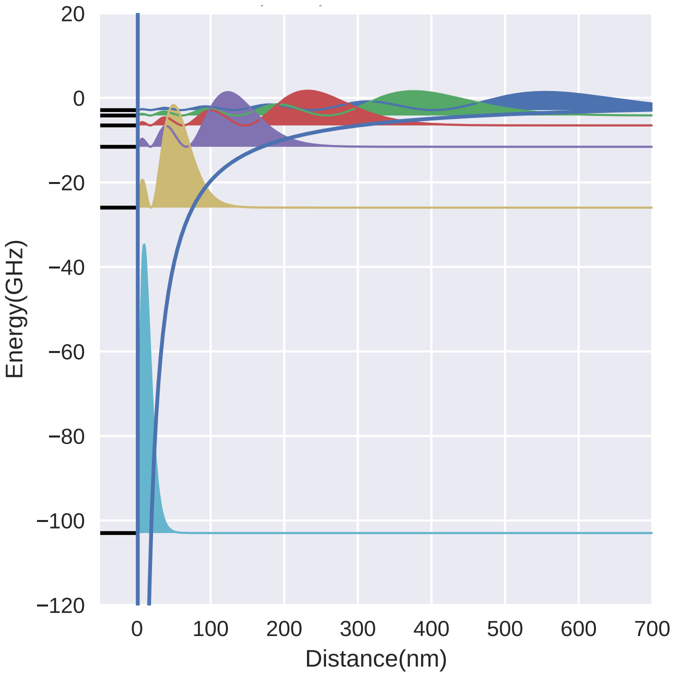

Figure 2: Energy eigenvalues (in GHz) and probability densities (in a.u.) for a surface electron on liquid ^{3}He.

Electrons on helium realize a unique 2D electron system because they are formed above an extremely clean and smooth substrate. Helium liquefies at temperatures around 4 K when all other substances solidify, therefore are frozen onto the walls of a container holding liquid helium. Thus, the free surface of liquid helium has no impurities, static irregularities or defects. At temperatures below 1 K, when the density of helium vapor atoms above the surface is negligible, the scattering of electrons is only from liquid surface excitations (ripplons) whose density decreases with cooling. Low scattering rates result, for example, in the highest electron mobility $\sim 10^4$ $\mathrm{m}^2/(\mathrm{V{\cdot}s})$ known for any 2DES so far. This unique feature of SEs attracted condensed-matter physicists for many year and many new and interesting phenomena were discovered, such as the first realization of a Wigner Solid (the crystalline phase of 2DES), discovery of novel edge magneto-plasmon modes, unconventional classical Hall effect, etc. [36, 37]. These phenomena are complementary to the physics of the Quantum Hall Effect in semiconductor-based systems, such as two-dimensional electron gas (2DEG) in Si inversion layers, GaAs/AlGaAs heterostructures and, most recently, in graphene.

However, there is another interesting aspect of this system which, to the best of my knowledge, has not been sufficiently discussed in the literature. As shown above, the Rydberg states of SEs have many similarities with the Rydberg atoms, whose quantum properties have been studied very actively for the past few decades. SEs have a relatively large transition dipole moment, see Table 3, that can rather strongly couple them to propagating or standing EM waves. The Coulomb interaction between electrons can lead to shifts in the Rydberg energy spectrum [38], thus showing effects similar to the Rydberg blockade in an ensemble of atoms [16, 39], which potentially can be used to simulate quantum many-body phenomena in these systems. Finally, the quantum states of orbital motion of SEs are shown to have rather long coherence time (10-100 μs), which makes them a promising system for quantum information processing applications [26, 29, 40].

The aim of this thesis was to make initial theoretical and experimental studies with electrons on helium in the above context. In particular, we aimed to, for the first time, coherently control Rydberg states of SEs by light. While it sounds straightforward to apply the same ideas and techniques which are used for the Rydberg atoms, for example coupling the Rydberg states of SEs to an optical cavity mode, certain technical limitations where encountered during the experiments. In particular, it was found that it is much easier to couple the EM field in our optical cavities to the in-plane motion of SEs. Therefore, some modifications of the original plan had to be made. In particular, I first studied the coupling between the in-plane quantized motion of SEs in a perpendicular magnetic field and an optical cavity mode, which will be discussed in Chapter 1. There, we demonstrated the strong coupling between an ensemble of electrons and cavity. I also developed a full theoretical framework to describe these experiments. Complementary to this, I studied a abstract theoretical model which can be potentially applied to electrons on helium and realized in our experiments. This will be described in details in Chapter 2. Finally, we studied the coupling between the in-plane motion of SEs and their Rydberg states, which ultimately will be used to couple the Rydberg states of SEs to EM field in a cavity. In particular, we realized such coupling by introducing an in-plane magnetic field. In Chapter 3, I provide a detailed theoretical analysis of the coupled orbital motion of the SEs and make a comparison between the theoretical predictions and experimental results. In the last chapter, I will conclude the whole thesis with a brief discussion of future works.

Chapter 1

Surface electrons on helium strongly coupled to a microwave resonator

In the strong coupling regime, the light stored in a cavity resonator interacts with matter at a time scale which is faster then energy dissipation and decoherence, which allows coherent control of matter using light. This chapter describes an experimental realization of the strong coupling between the cyclotron motion of two-dimensional electrons on liquid helium and an electromagnetic mode of an optical (Fabry-Perot type) resonator working in a microwave frequency range. In the experiment, the strong coupling is manifested by the normal-mode splitting in the spectrum of coupled mode-particle motion. We constructed a systematic quantum mechanical model to fully describe dynamics of this coupled system. In particular, our model uses a quantum harmonic oscillator to represent the cyclotron motion of the many-electron system, while using the standard QED description for the cavity mode. As shown, our model provides complete description of the experimental results, including a surprising feature of coupling between the electron cyclotron motion and a circularly-polarized mode that rotates in the direction opposite to the electron motion. This work has been published in [41].

1.1 Motivation

Light-matter interaction between an N-particle system and a single-mode cavity resonator is a long-standing topic in atomic physics and quantum optics. Of particular interests is the strong coupling regime in which the rate of energy exchange between particles and cavity mode exceeds the dissipation rates set by cavity losses and relaxation processes in the system. In N-particle systems, the coupling is enhanced by a factor of $\sqrt{N}$ compared to a single particle and hence makes the strong coupling regime experimentally more accessible. In experiments, the coupling strength is manifested by the normal-mode slitting in the spectrum of coupled mode-particle motion, with the splitting given by twice the $\sqrt{N}$-enhanced coupling constant [42–45]. It has been mentioned that this splitting is essentially classical effect which can be understood on the ground of two coupled damped oscillators [44, 46], and that observation of QED features require, for example, photon correlation experiments [47].

Interests in collective coupling between matter and light was recently revived and spread to a broad range of systems mainly due to its applications for hybrid quantum systems and quantum technologies [19, 48]. Motivated by proposals to use solid-state systems strongly coupled to microwave (MW) resonators for efficient quantum memory storage [49–51], any experimental works were recently reported using solid-state spin ensembles [29, 52–61]. Some recent work has been also done in the two-dimensional electron gas (2DEG) in semiconductors where the cyclotron motion of electrons in a strong perpendicular magnetic field was coupled to resonant structures [62, 63]. In most of these recent works the normal mode splitting is presented as some kind of a QED effect and treated in terms of the Jaynes-Cummings-type Hamiltonian typical for cavity QED settings. However, this might seem to be surprising in the light of the earlier work in atomic physics and quantum optics, as we mentioned earlier.

Here, we study the strong coupling between the cyclotron motion of a many-electron system formed on the surface of liquid helium and an EM mode in a microwave resonator. As was shown previously [64], the experimentally observed normal-mode splitting in the spectrum of coupled mode-particle motion can be completely accounted by a simplified theoretical model based on classical electrodynamics. Motivated by the recent interests to the strong coupling regime from the prospects of applications for quantum technologies, we constructed a full quantum mechanical model to describe our system and fully account for all experimental observations. As expected, we show that both classical and full quantum mechanical treatments are equivalent for description of the linear coupled systems studied here. Nevertheless, the proposed full quantum treatment is very convenient to use, thus can serve as a useful tool to describe our future experiments.

1.2 Theoretical background

This chapter briefly overviews the necessary theoretical background regarding QED description of EM field and quantum description of the cyclotron motion of two-dimensional electrons subject to a static magnetic field. The results derived here will be used in later sections of this Chapter. We use the hat notation for quantum mechanical operators, e.g. $\hat{A}$, to emphasize the difference between a quantum mechanical operator and an ordinary number.

1.2.1 Classical and quantum description of EM field

The electric ($\boldsymbol{E}$) and magnetic ($\boldsymbol{B}$) fields in a source-free medium obey the classical Maxwell equations (we use S.I. units):

$$\nabla \cdot \boldsymbol{D} = 0, \tag{1.1a}$$

$$\nabla \cdot \boldsymbol{B} = 0, \tag{1.1b}$$

$$\nabla \times \boldsymbol{E} = -\partial_t \boldsymbol{B}, \tag{1.1c}$$

$$\nabla \times \boldsymbol{H} = \partial_t \boldsymbol{D}. \tag{1.1d}$$

where ∂_t stands for the partial derivative with respect to time. Two additional vector fields $\boldsymbol{D} = \epsilon_0\boldsymbol{E} + \boldsymbol{P}_e$ and $\boldsymbol{H} = \boldsymbol{B}/\mu_0 - \boldsymbol{M}$ are introduced to describe the effect of medium, where $\boldsymbol{P}_e$ ($\boldsymbol{M}$) is the induced electrical (magnetic) dipole moment of the medium per unit volume and $\epsilon_0 = 8.854 \times 10^{-12}$ F/m ($\mu_0 = 4\pi \times 10^{-7}$ H/m) is the permittivity (permeability) of medium-free space (vacuum).

In a linear medium, the relation between vector fields simplify to $\boldsymbol{D} = \epsilon_0(1+\chi_e)\boldsymbol{E} = \epsilon\boldsymbol{E}$ and $\boldsymbol{B} = \mu_0(1 + \chi_m)\boldsymbol{H} = \mu\boldsymbol{H}$, where χ_e (χ_m) is called the electric (magnetic) susceptibility and ϵ (μ) is the dielectric constant (permeability) of medium. For a linear homogeneous medium, from Eq. (1.1) we can obtain a pair of the wave equations for vectors $\boldsymbol{E}$ and $\boldsymbol{B}$:

$$\nabla \times \boldsymbol{E} - \epsilon\mu\partial_t^2\boldsymbol{E} = 0, \tag{1.2a}$$

$$\nabla \times \boldsymbol{B} - \epsilon\mu\partial_t^2\boldsymbol{B} = 0. \tag{1.2b}$$

As usual, an arbitrary time dependence of the EM field can be expanded in the Fourier series. Following an adopted convention, it is convenient to consider the harmonic (with angular frequency ω) time dependence of vector fields in a complex form $\exp(-\mathrm{i}\omega t)$. Then, from the wave equations we obtain the Helmholtz equations for complex-phasor space vectors $\tilde{\boldsymbol{E}}(\boldsymbol{r})$ and $\tilde{\boldsymbol{B}}(\boldsymbol{r})$:

$$\nabla^2\tilde{\boldsymbol{E}} + \omega^2\mu\epsilon\tilde{\boldsymbol{E}} = 0, \tag{1.3a}$$

$$\nabla^2\tilde{\boldsymbol{B}} + \omega^2\mu\epsilon\tilde{\boldsymbol{B}} = 0. \tag{1.3b}$$

The complex-phasor space vectors contain information about the spatial distribution of the EM field and are related to the components of the electric and magnetic fields as $\boldsymbol{E}(\boldsymbol{r}, t) = \mathrm{Re}[\tilde{\boldsymbol{E}}(\boldsymbol{r})\exp(-\mathrm{i}\omega t)]$ and $\boldsymbol{B}(\boldsymbol{r}, t) = \mathrm{Re}[\tilde{\boldsymbol{B}}(\boldsymbol{r})\exp(-\mathrm{i}\omega t)]$.

The general solution of the Helmholtz equation, e.g. for the electric field, is given by

$$\tilde{\boldsymbol{E}} = \sum_{\boldsymbol{k},\alpha}\tilde{\boldsymbol{E}}_{\boldsymbol{k},\alpha} = \sum_{\boldsymbol{k},\alpha}\boldsymbol{E}_{\boldsymbol{k},\alpha}e^{\mathrm{i}\boldsymbol{k}\boldsymbol{r}}, \tag{1.4}$$

where $\boldsymbol{k}$ is the wave vector which defines the propagation direction for the mode $\tilde{\boldsymbol{E}}_{\boldsymbol{k},\lambda}$ and whose magnitude satisfies $k = \omega\epsilon\mu = \omega/v$, where $v = 1/\sqrt{\epsilon\mu}$ is the speed of light in medium. In addition, the index α labels two possible polarizations, that is mutual relation between different components of the field vector, for a given wave vector $\boldsymbol{k}$. From the Maxwell equation 1.1c, the corresponding solution for the magnetic field is related to $\tilde{\boldsymbol{E}}$ by

$$\tilde{\boldsymbol{B}} = (\mathrm{i}\omega)^{-1}\nabla \times \tilde{\boldsymbol{E}}. \tag{1.5}$$

The allowed solutions for the Helmholtz equations must also satisfy the boundary conditions imposed by the Maxwell equations at the interfaces between different media:

$$\boldsymbol{n}\cdot(\tilde{\boldsymbol{D}}_2-\tilde{\boldsymbol{D}}_1)=\tilde{\rho}_s, \tag{1.6a}$$

$$\boldsymbol{n}\cdot(\tilde{\boldsymbol{B}}_2-\tilde{\boldsymbol{B}}_1)=0, \tag{1.6b}$$

$$\boldsymbol{n}\times(\tilde{\boldsymbol{E}}_2-\tilde{\boldsymbol{E}}_1)=0, \tag{1.6c}$$

$$\boldsymbol{n}\times(\tilde{\boldsymbol{H}}_2-\tilde{\boldsymbol{H}}_1)=\tilde{\boldsymbol{j}}_s, \tag{1.6d}$$

where $\boldsymbol{n}$ is the unit vector normal to the interface between media 1 and 2 ($\boldsymbol{n}$ points from medium 1 towards medium 2), and $\tilde{\rho}_s$ ($\tilde{\boldsymbol{j}}_s$) is the complex-phasor of the time-dependent electrical charge (current) at the interface per unit area.

As a simple example, which is related to our later discussion, consider a monochromatic plane EM wave propagating along z direction in a source-free medium confined between two perfectly conducting infinite (xy-plane) plates located at $z=0$ and $z=L$. The general solution of the Helmholtz equation (1.3) for this case is the sum of two waves propagating in the positive and negative z directions:

$$\tilde{\boldsymbol{E}}(z)=\left(\mathbf{e}_x E_x^{(1)}+\mathbf{e}_y E_y^{(1)}\right)e^{\mathrm{i}kz}+\left(\mathbf{e}_x E_x^{(2)}+\mathbf{e}_y E_y^{(2)}\right)e^{-\mathrm{i}kz}, \tag{1.7}$$

where $\mathbf{e}_x$ and $\mathbf{e}_y$ are unit vectors in x and y directions, respectively, and $E_{x(y)}^{(1)}$ and $E_{x(y)}^{(2)}$ are arbitrary complex amplitudes. By applying the boundary condition (1.6c), that is $\tilde{\boldsymbol{E}}(0)=\tilde{\boldsymbol{E}}(L)=0$, we can find relations between complex amplitudes for the two counter-propagating waves, as well as all allowed values of k, which results in

$$\tilde{\boldsymbol{E}}(z)=2\mathrm{i}\mathbf{e}_x E_x^{(1)}\sin(kz)+2\mathrm{i}\mathbf{e}_y E_y^{(1)}\sin(kz), \tag{1.8}$$

where k must satisfy a relation $\sin(kL)=0$. The corresponding expression for the complex-phasor vector of the magnetic field can be immediately obtained from Eq. (1.5)

$$\tilde{\boldsymbol{B}}(z)=2v^{-1}\mathbf{e}_x E_y^{(1)}\cos(kz)+2v^{-1}\mathrm{i}\mathbf{e}_y E_x^{(1)}\cos(kz), \tag{1.9}$$

The above solutions describe a superposition of two standing waves with independent linear polarizations of the electric field (in x and y directions).

Sometimes it is also convenient to introduce notations for a pair of mutually orthogonal polarization vectors $\mathbf{e}_\alpha$, $\alpha=1,2$. In the above example, we can treat the unit vectors $\mathbf{e}_x$ and $\mathbf{e}_y$ as such polarization vectors corresponding to two independent linear polarizations of EM field. Alternatively, we can introduce a pair of polarization vectors according to $\mathbf{e}_\pm=(\mathbf{e}_x\mp\mathrm{i}\mathbf{e}_y)/\sqrt{2}$. It is easy to see that these vectors satisfy the orthonormality condition, $\boldsymbol{e}_\pm\mathbf{e}_\pm^*=1$, $\mathbf{e}_\pm\mathbf{e}_\mp^*=0$, and Eq. (1.7) can be represented as

$$\tilde{\boldsymbol{E}}(z)=\left(\mathbf{e}_+E_+^{(1)}+\mathbf{e}_-E_-^{(1)}\right)e^{\mathrm{i}kz}+\left(\mathbf{e}_+E_+^{(2)}+\mathbf{e}_-E_-^{(2)}\right)e^{-\mathrm{i}kz}, \tag{1.10}$$

where $E_\pm=(E_x\pm\mathrm{i}E_y)/\sqrt{2}$. Correspondingly, the standing wave solution (1.8) can be represented in the form

$$\tilde{\boldsymbol{E}}(z)=2\mathrm{i}\mathbf{e}_+E_+^{(1)}\sin(kz)+2\mathrm{i}\mathbf{e}_-E_-^{(1)}\sin(kz). \tag{1.11}$$

It is easy to check that this describes a superposition of two standing waves with independent circular polarizations of the electric field. The first term in the above equation corresponds to the electric field rotating clockwise in the xy plane, and is referred to as the left-hand-circularly-polarized (LHCP) wave. Similarly, the second term corresponds to the electric field rotating counter-clockwise in the xy plane, and is referred to as the right-hand-circularly-polarized (RHCP) wave. Thus, any vector solution for the EM field can be always represented as a linear combination of the two independent polarization vectors $\mathbf{e}_\alpha$, $\alpha = 1, 2$ (either linear or circular).

Next, we briefly review procedure that leads to the quantization of the EM field. It will be convenient to write the general solutions of Eqs. (1.2) for the $\boldsymbol{E}$ and $\boldsymbol{B}$ fields in the form

$$\boldsymbol{E}(\boldsymbol{r},t) = \sum_{\boldsymbol{k},\alpha} P_{\boldsymbol{k},\alpha}(t)\boldsymbol{E}_{\boldsymbol{k},\alpha}(\boldsymbol{r}), \tag{1.12a}$$

$$\boldsymbol{B}(\boldsymbol{r},t) = \sum_{\boldsymbol{k},\alpha} \omega_k Q_{\boldsymbol{k},\alpha}(t)\boldsymbol{B}_{\boldsymbol{k},\alpha}(\boldsymbol{r}), \tag{1.12b}$$

where $P_{\boldsymbol{k},\alpha}(t)$ and $Q_{\boldsymbol{k},\alpha}(t)$ ($\boldsymbol{E}_{\boldsymbol{k},\alpha}(\boldsymbol{r})$ and $\boldsymbol{B}_{\boldsymbol{k},\alpha}(\boldsymbol{r})$) are real-valued functions of time (position vector). It is clear that $\boldsymbol{E}_{\boldsymbol{k},\alpha}(\boldsymbol{r})$ and $\boldsymbol{B}_{\boldsymbol{k},\alpha}(\boldsymbol{r})$ satisfy the Helpmhotz equations similar to Eq. (1.3) with $\omega_k = k/\sqrt{\epsilon\mu} = kv$, while $P_{\boldsymbol{k},\alpha}(t)$ and $Q_{\boldsymbol{k},\alpha}(t)$ satisfy

$$\ddot{P}_{\boldsymbol{k},\alpha} + \omega_k^2 P_{\boldsymbol{k},\alpha} = 0, \tag{1.13a}$$

$$\ddot{Q}_{\boldsymbol{k},\alpha} + \omega_k^2 Q_{\boldsymbol{k},\alpha} = 0. \tag{1.13b}$$

Thus, the total energy stored in a volume V occupied by the EM field can be written as:

$$\mathcal{H} = \int_V \mathrm{d}V \left(\frac{\boldsymbol{E}\cdot\boldsymbol{D}}{2} + \frac{\boldsymbol{B}\cdot\boldsymbol{H}}{2} \right) = \sum_{\boldsymbol{k},\alpha} \left(\frac{P_{\boldsymbol{k},\alpha}^2}{2} + \frac{\omega_k^2 Q_{\boldsymbol{k},\alpha}^2}{2} \right) \Delta E_{\boldsymbol{k},\alpha}, \tag{1.14}$$

where $\Delta E_{\boldsymbol{k},\alpha} = \int_V \mathrm{d}V \left(\epsilon \boldsymbol{E}_{\boldsymbol{k},\alpha}^2\right) = \int_V \mathrm{d}V \left(\boldsymbol{B}_{\boldsymbol{k},\alpha}^2/\mu\right)$.

The above expression points out that we can describe the EM field by a classical Hamiltonian of a collection of harmonic oscillators each described by two continuous canonical variables $Q_{\boldsymbol{k},\alpha}, P_{\boldsymbol{k},\alpha}$. In quantum mechanics, we introduce corresponding Hermitian operators $\hat{Q}_{\boldsymbol{k},\alpha}$, $\hat{P}_{\boldsymbol{k},\alpha}$ which satisfy the commutation relation $[\omega_k \hat{Q}_{\boldsymbol{k},\alpha}, \hat{P}_{\boldsymbol{k}',\alpha'}] = i\delta_{\boldsymbol{k},\boldsymbol{k}'}, \delta_{\alpha,\alpha'}$. As usual, it is convenient to introduce the lowering/raising operators defined by

$$\hat{a}_{\boldsymbol{k},\alpha} = 2^{-1/2}\left(\omega_k \hat{Q}_{\boldsymbol{k},\alpha} + \mathrm{i}\hat{P}_{\boldsymbol{k},\alpha}\right), \tag{1.15a}$$

$$\hat{a}_{\boldsymbol{k},\alpha}^\dagger = 2^{-1/2}\left(\omega_k \hat{Q}_{\boldsymbol{k},\alpha} - \mathrm{i}\hat{P}_{\boldsymbol{k},\alpha}\right), \tag{1.15b}$$

which satisfy the bosonic commutation relations $[\hat{a}_{\boldsymbol{k},\alpha}, \hat{a}_{\boldsymbol{k},\alpha}^\dagger] = \delta_{\boldsymbol{k},\boldsymbol{k}'}, \delta_{\alpha,\alpha'}$. From Eq. (1.14), the corresponding quantum mechanical Hamiltonian reads

$$\hat{\mathcal{H}}_a = \sum_{\boldsymbol{k},\lambda} \frac{\Delta E_{\boldsymbol{k},\alpha}}{2} (\hat{a}^\dagger_{\boldsymbol{k},\lambda}\hat{a}_{\boldsymbol{k},\lambda} + \hat{a}_{\boldsymbol{k},\lambda}\hat{a}^\dagger_{\boldsymbol{k},\lambda}) = \sum_{\boldsymbol{k},\lambda} \Delta E_{\boldsymbol{k},\alpha}(\hat{a}^\dagger_{\boldsymbol{k}}\hat{a}_{\boldsymbol{k}} + 1/2). \tag{1.16}$$

Finally, it is convenient to define the vector fields $\boldsymbol{E}_{\boldsymbol{k},\alpha}$ and $\boldsymbol{B}_{\boldsymbol{k},\alpha}$ for each mode as a product of the polarization vector $\mathbf{e}_\alpha$ and some normalized complex functions of position vector, $\boldsymbol{E}_{\boldsymbol{k},\alpha} = E_{\text{vac}}\mathbf{e}_\alpha f_{\boldsymbol{k},\alpha}(\boldsymbol{r})$ and $\boldsymbol{B}_{\boldsymbol{k},\alpha} = B_{\text{vac}}\mathbf{e}_\alpha g_{\boldsymbol{k},\alpha}(\boldsymbol{r})$, such that $\int_V \mathrm{d}V\, |f_{\boldsymbol{k},\alpha}|^2 = \int_V \mathrm{d}V\, |g_{\boldsymbol{k},\alpha}|^2 = V$. To complete analogy with the quantum harmonic oscillator, we require that $\Delta E_{\boldsymbol{k},\alpha} = \hbar\omega_k$, from which we obtain $E_{\text{vac}} = \sqrt{\hbar\omega_k/(2\epsilon V)}$ and $B_{\text{vac}} = \sqrt{\mu\hbar\omega_k/(2V)}$, which are related to the r.m.s. electric and magnetic fields of vacuum.

Thus, the above quantum mechanical treatment states that the energy of each EM mode is quantized in fractions of $\hbar\omega_k$, which are often represented as fictitious bosonic particles, photons, with the raising/lowering operators for each mode playing roles of the photon creation/anihilation operators. From Eqs. (1.12), the corresponding vector operators for the electric and magnetic fields are

$$\hat{\boldsymbol{E}} = \mathrm{i} \sum_{\boldsymbol{k},\lambda} \sqrt{\frac{\hbar\omega_k}{2\epsilon V}} \Big(\mathbf{e}_\alpha f_{\boldsymbol{k},\alpha}\hat{a}_{\boldsymbol{k},\alpha} - \mathbf{e}^*_\alpha f^*_{\boldsymbol{k},\alpha}\hat{a}^\dagger_{\boldsymbol{k},\alpha}\Big), \tag{1.17a}$$

$$\hat{\boldsymbol{B}} = \sum_{\boldsymbol{k},\lambda} \sqrt{\frac{\mu\hbar\omega_k}{2V}} \Big(\mathbf{e}_\alpha g_{\boldsymbol{k},\alpha}\hat{a}_{\boldsymbol{k},\alpha} + \mathbf{e}^*_\alpha g^*_{\boldsymbol{k},\alpha}\hat{a}^\dagger_{\boldsymbol{k},\alpha}\Big). \tag{1.17b}$$

This form ensures that the operators $\hat{\boldsymbol{E}}$ and $\hat{\boldsymbol{B}}$ are Hermitian, which corresponds to real-valued classical vector fields $\boldsymbol{E}$ and $\boldsymbol{B}$. In the Heisenberg picture, the time dependence of operators comes from $\hat{a}_{\boldsymbol{k},\alpha}(t) = \hat{a}_{\boldsymbol{k},\alpha}|_{t=0}\exp(-\mathrm{i}\omega_k t)$, $\hat{a}^\dagger_{\boldsymbol{k},\alpha}(t) = \hat{a}^\dagger_{\boldsymbol{k},\alpha}|_{t=0}\exp(\mathrm{i}\omega_k t)$, as can be immediately obtained from the Hamiltonian (1.16) and the bosonic commutation relations.

Finally, it is also helpful to introduce the operator of the vector potential. Using the classical expression $\boldsymbol{E} = -\partial_t\boldsymbol{A}$, in the Heisenber picture we obtain

$$\hat{\boldsymbol{A}} = \sum_{\boldsymbol{k},\lambda} \sqrt{\frac{\hbar}{2\epsilon\omega_k V}} \Big(\mathbf{e}_\alpha f_{\boldsymbol{k},\alpha}\hat{a}_{\boldsymbol{k},\alpha}e^{-\mathrm{i}\omega_k t} + \mathbf{e}^*_\alpha f^*_{\boldsymbol{k},\alpha}\hat{a}^\dagger_{\boldsymbol{k},\alpha}e^{\mathrm{i}\omega_k t}\Big). \tag{1.18}$$

1.2.2 Cyclotron motion of two-dimensional electron systems

In two-dimensional electron systems (2DESs), the motion of electrons in one direction (we assume z direction) is quantized and all electrons occupy the lowest energy state for this motion. Such electrons can move in the 2D plane and couple to the EM field which has the electric field $\boldsymbol{E}$ lying in the xy plane. For a classical particle of charge $-e$ ($e>0$ is the elementary charge) and mass m_e, the equation of motion reads

$$m_e\partial_t\boldsymbol{v} = -e\boldsymbol{E} - m_e\boldsymbol{v}\nu, \tag{1.19}$$

where $\boldsymbol{v}$ is the particle velocity in the xy plane. In addition, we introduced a phenomenological scattering rate of electrons ν which characterizes their interaction with environment. For a many-electron system, summing over all electrons (we assume that all electrons experience the same electric field), we can write the equation of motion for the electron current density $\boldsymbol{j} = -en_s\boldsymbol{v}$, where n_s is the areal density of electrons, in the form

$$\partial_t \boldsymbol{j} = \sigma_0 \boldsymbol{E} - \nu \boldsymbol{j}, \tag{1.20}$$

where $\sigma_0 = n_s e^2\tau/m_e$ and $\tau = 1/\nu$ is the scattering time. Assuming harmonic dependence for the electric field in the form $\exp(-\mathrm{i}\omega t)$, we obtain a simple relation between the current density and driving electric field:

$$\boldsymbol{j} = \sigma(\omega)\boldsymbol{E}, \tag{1.21}$$

where the ac conductivity is given by

$$\sigma(\omega) = \frac{\sigma_0}{1 - \mathrm{i}\omega\tau}. \tag{1.22}$$

The motion of electrons in the xy plane, therefore the ac conductivity, can be strongly modified by applying a uniform static magnetic field $\boldsymbol{B}_0$ along z direction. By adding the Lorentz force in Eq. (1.19) and repeating the same steps, we obtain

$$-i\omega\tau j_x = \sigma_0 E_x + \omega_c \tau j_y - j_x, \tag{1.23a}$$
$$-i\omega\tau j_y = \sigma_0 E_y - \omega_c \tau j_x - j_y, \tag{1.23b}$$

from which we obtain

$$\begin{aligned} j_x &= \frac{\sigma_0(1 - i\omega\tau)}{(1 - i\omega\tau)^2 + \omega_c^2\tau^2} E_x + \frac{\sigma_0\omega_0\tau}{(1 - i\omega\tau)^2 + \omega_c^2\tau^2} E_y, \\ j_y &= -\frac{\sigma_0\omega_0\tau}{(1 - i\omega\tau)^2 + \omega_c^2\tau^2} E_x + \frac{\sigma_0(1 - i\omega\tau)}{(1 - i\omega\tau)^2 + \omega_c^2\tau^2} E_y, \end{aligned} \tag{1.24a}$$

where $\omega_c = eB_0/m_e$ is the cyclotron frequency. Thus, in perpendicular magnetic fields the ac conductivity becomes a symmetric tensor with elements $\sigma_{xx} = \sigma_{yy}$, $\sigma_{xy} = -\sigma_y x$, where

$$\sigma_{xx} = \frac{\sigma_0(1 - i\omega\tau)}{1 + (\omega_c^2 - \omega^2)\tau^2 - 2i\omega\tau}, \tag{1.25a}$$
$$\sigma_{xy} = \frac{\sigma_0\omega_c\tau}{1 + (\omega_c^2 - \omega^2)\tau^2 - 2i\omega\tau}. \tag{1.25b}$$

Using notations $E_\pm = E_x \pm iE_y$ and $j_\pm = j_x \pm ij_y$, which were discussed in the previous section, Eqs. (1.24) can be represented in a more convenient form

$$j_\pm = \sigma_\pm E_\pm. \tag{1.26}$$

where the ac conductivity $\sigma_\pm = \sigma_{xx} \pm i\sigma_{xy}$ is given by

$$\sigma_\pm = \frac{\sigma_0 \nu}{\nu - i(\omega \pm \omega_c)}, \tag{1.27}$$

As discussed in the previous section, the complex amplitude E_+ (E_-) corresponds to the vector of the electric field which rotates clockwise (counter-clockwise) in the xy plane. Similar situation holds for the complex amplitudes of the current density of electrons $j_\pm$. It is clear from Eq. (1.27) that the counter-clockwise rotating, that is RHCP, electric field E_- couples strongly to the motion of electrons when the frequency ω is close to the cyclotron frequency ω_c. The origin of such a cyclotron resonance (CR) is clear. In the static magnetic field $\boldsymbol{B}_0$ applied in the positive z direction, electrons undergo cyclotron motion in the xy plane in the counter-clockwise direction, thus are able to continuously gain energy from the electric field when the frequencies of their rotation are close. Contrarily, for the clockwise rotating, that is LHCP, electric field electrons gain energy from and loose energy to the field twice per every period of rotation. For this reason, the resonant mode (RHCP in the above case) is often called the CR-active mode, while the oppositely rotating (LHCP in the above case) mode is called the CR-passive mode.

Next, we briefly discuss the quantum mechanical description of the cyclotron motion of electrons. In order to describe effect of the applied static magnetic field $\boldsymbol{B}_0$, it is convenient to introduce the corresponding vector potential $\boldsymbol{A}_0$. The quantum mechanical Hamiltonian for an electron reads

$$\hat{H} = \frac{1}{2m_e}(\hat{\boldsymbol{p}} + e\hat{\boldsymbol{A}}_0)^2. \tag{1.28}$$

As is well known, the eigen states of this Hamiltonian represent the quantized states of electron orbital motion in xy plane with an equidistant energy spectrum $E_n = \hbar\omega_c(n+1/2)$, $n = 0, 1, ..$ (the Landau levels). To describe motion of a many-electron system, it is convenient to introduce the operator of kinematic momentum $\hat{\boldsymbol{\pi}} = \hat{\mathbf{p}} + e\hat{\boldsymbol{A}}_0$ defined for a single electron and use the symmetric gauge for the vector potential, $\hat{\boldsymbol{A}}_0 = (-\hat{y}B_0/2, \hat{x}B_0/2, 0)$. The commutation relation $[\hat{\pi}_x, \hat{\pi}_y] = -i\hbar e B_0$ leads to the definition of a dimensionless lowering/raising operators

$$\hat{b} = \sqrt{\frac{1}{2\hbar e B_0}}(\hat{\pi}_x - i\hat{\pi}_y), \tag{1.29a}$$

$$\hat{b}^\dagger = \sqrt{\frac{1}{2\hbar e B_0}}(\hat{\pi}_x + i\hat{\pi}_y), \tag{1.29b}$$

which satisfy the bosonic commutation relation $[\hat{b}, \hat{b}^\dagger]{=}1$. This single-particle operator can be related to a complex current density operator for a many-particle system $\hat{j}_- = 2^{-1/2}(\hat{j}_x - i\hat{j}_y)$, where $\hat{j}_x = (-e/m_e S)\sum_e \hat{\pi}_x$ and $\hat{j}_y = (-e/m_e S)\sum_e \hat{\pi}_y$. Here, the sum is over all electrons in the system, and S is the surface area occupied by the electron system. It is clear that operator $\hat{j}_-$ is the quantum mechanical analog of the classical current density j_- due to the cyclotron motion of electrons, which was discussed earlier in this section. The operators $\hat{b}$ and $\hat{j}_-$ are related by

$$\hat{j}_- = -\frac{e\omega_c l_B N}{S}\hat{b}, \tag{1.30}$$

where N is the number of particles in the system and $l_B = \sqrt{\hbar/(eB_0)}$ is the magnetic length. Thus, our treatment states that the cyclotron motion of the many-electron system can be represented by a quantum harmonic oscillator described by the lowering (raising) operator $\hat{b}$ ($\hat{b}^\dagger$), which corresponds to decreasing (increasing) the current density j_- due to the cyclotron motion by $-en_s\omega_c l_B$.

The effect of EM field on the motion of electrons can be introduced in a similar way by defining the corresponding vector potential $\boldsymbol{A}$ for the EM field and writing the Hamiltonian for the many-electron system as

$$\hat{H} = \frac{1}{2m_e}\sum_e (\hat{\boldsymbol{\pi}} + e\boldsymbol{A})^2. \tag{1.31}$$

In the full QED treatment, we replace $\boldsymbol{A}$ with the corresponding operator of the vector potential $\hat{\boldsymbol{A}}$ introduced in the previous section. The full quantum treatment will be discussed in Section 1.5.

1.3 Experimental realization of the strong coupling between 2D electrons and light

In this Section, we briefly describe experimental methods which we used to realize and study the strong coupling regime of interaction between 2DES on the surface of liquid helium and a single-mode optical resonator working in the microwave (MW) frequency range. [1]

1.3.1 Experimental setup and measurements

The main features of our experimental setup used to realize the strong coupling between the cyclotron motion of 2D electrons and an EM mode is illustrated in Fig. 1.1. 2D electron system is formed on the surface of liquid helium placed between two mirrors of a single-mode optical cavity resonator. The Gaussian beam of the cavity mode impinges the 2D electron system, thus couples to the electron cyclotron motion induced by the applied magnetic field $\boldsymbol{B}_0$. In the experiment, we used a semi-confocal Fabry-Perot (FP) resonator which consisted of a top hemispherical mirror and a bottom flat mirror. The COMSOL simulation of the resonator mode is shown in Fig. 1.2. In the experiment described here we used a resonant TEM$_{003}$ mode (angular frequency $\omega_r \approx 35.14$ GHz) with three anti-nodes of the electric field between the mirrors [65].

The physical realization of the experimental method is shown in Fig. 1.3. The experiment was done with 2D electrons on liquid ^{3}He cooled below 1 K in a vacuum-tight copper cell attached to the mixing chamber of a dilution refrigerator, see Fig. 1.3(a).

---

[1] The experimental data presented in this section were obtained by Aleksiy A. Zadorozhko who designed and performed the experiment.

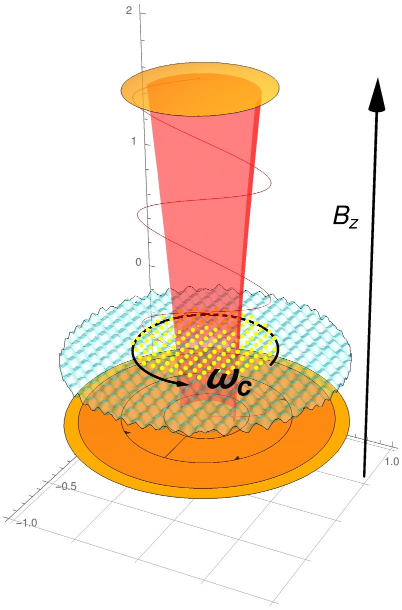

Figure 1.1: An illustration of the experimental setup used to realize the strong coupling between 2D electrons on liquid helium and a single EM mode in an optical resonator.

The design of the cell is shown in Fig. 1.3(b). The semi-confocal Fabry-Perot resonator was formed by a top spherical mirror made of copper and a bottom flat mirror made of a 0.5 μm-thick gold film evaporated on a sapphire substrate. The spherical mirror had the diameter of 35.3 mm and curvature of 30 mm. The flat mirror consisted of three concentric electrodes forming the Corbino disk with radia 7, 9.9, and 12.9 mm and 5 μm-wide gap between electrodes. The distance between two mirrors was $D = 13$ mm that determined the frequency of the resonant mode. To excite this mode, the linearly-polarized microwave radiation was supplied from a room temperature source and transmitted into the cell through a fundamental-mode (WR-28) rectangular waveguide which was vacuum-sealed with a Kapton film K, see Fig. 1.3(a). In addition, the waveguide had an infra-red filter F installed at the 4 K stage of the dilution refrigerator in order to stop the thermal radiation from the room temperature. The MW radiation was coupled from the waveguide into the cell through a Kapton-sealed 1.8 mm round aperture made in the middle of the spherical mirror, while the coupling was adjusted by the thickness of the wall of the mirror where the aperture was made.

The helium was condensed in the cell such that the liquid level was placed at a distance $h = 2.1$ mm above the flat mirror to coincide with the position of the first antinode of the cavity mode, see Fig. 1.3(c). The position of liquid level was monitored by observing the downshift of the resonant frequency of the resonator ω_r as the cell was filled with liquid and comparing it with the shift calculated using the finite element method (FEM). The electrons were produced by the thermal emission from a tungsten filament placed above the liquid surface and 2DES was created and confined on the surface above the flat mirror by applying a positive bias to the central and middle electrodes of the Corbino disk. To excite the cyclotron resonance of electrons, the

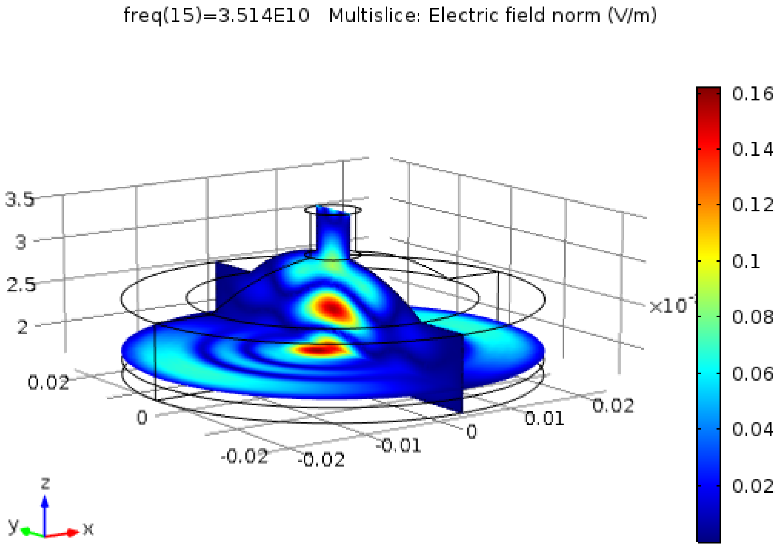

Figure 1.2: COMSOL simulation of the EM mode in a semi-confocal Fabri-Perot microwave (35.14 GHz) cavity resonator.

static magnetic field $\boldsymbol{B}_0$ was applied perpendicular to the liquid helium surface and the value of B_0 was adjusted such that the cyclotron frequency ω_c was close to ω_r. In the experiment, both ω_c and the frequency of the MW radiation $\omega/2\pi$ introduced into the cell could be varied, and either the MW power reflected from the cavity or the dc conductivity response of electrons could be measured as a function of ω_c and ω. To measure reflected power we used a pulse-modulated (at frequency $f_m =$ 10 kHz) MW signal applied to the resonator. The signal reflected from the cavity passed through a cryogenic circulator and was directed onto a cryogenic InSb detector (QMC Instruments Ltd.) operating at the temperature of the mixing chamber. The detector signal proportional to the MW power incident on it was measured by a lock-in amplifier at the modulation frequency f_m. For an empty cavity, the quality factor of the resonant TEM$_{003}$ mode was measured to be $Q \approx 10,000$.

In addition to MW power measurements, the dc conductivity signal of electrons was measured by the standard capacitive (Sommer-Tanner) method using the Corbino disk. To do this, a low-frequency ac signal at 1117 Hz was applied to the inner Corbino electrode and an ac current induced in the middle Corbino electrode by the electron motion was measured using a lock-in amplifier.

1.3.2 Results

Figure 1.4 (left panel) shows the power reflection from the cavity containing 2DES at the surface density of $n_s = 8.0 \times 10^7$ cm^{-2} measured at $T = 0.2$ K and input MW power $P = -9$ dBm. In this experiment, the detector signal was recorded by scanning the frequency of input MW signal ω at fixed value of magnetic field B_0, therefore the cyclotron frequency of electrons ω_c, and repeating experiments for different values of B_0. Due to the much larger quality factor Q of our cavity comparing with the previous

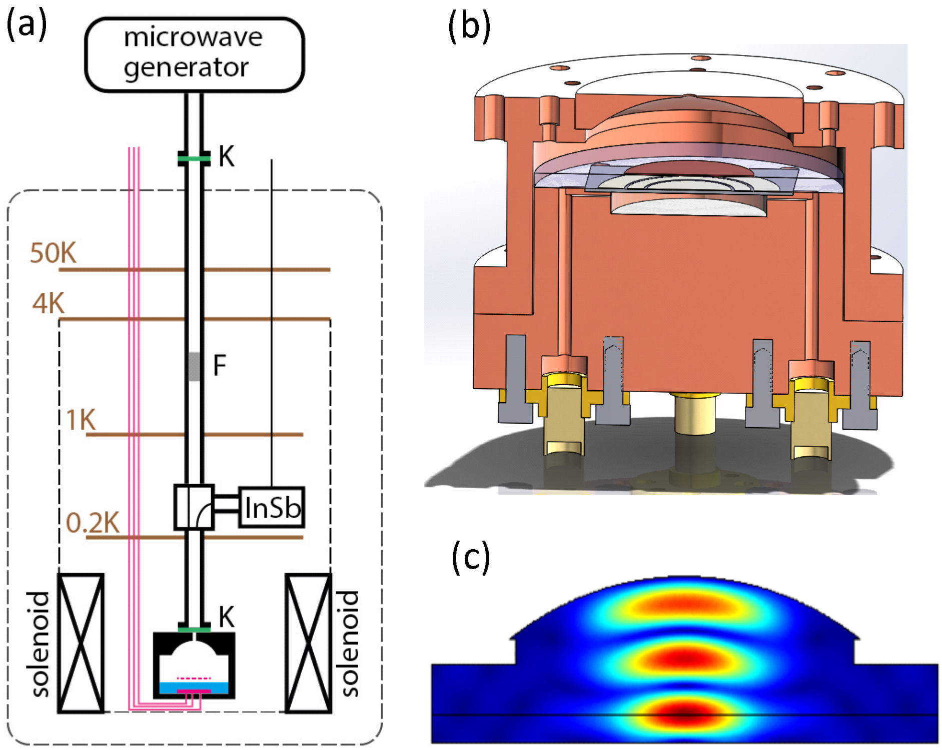

Figure 1.3: (a) Schematic diagram of the experimental setup. (b) 3D drawing of the experimental cell. (c) Distribution of the MW electric field of the resonant TEM_{002} mode inside the Fabry-Perot resonator. Black solid line shows position of the liquid helium level in the resonator which coincides with the position of the first antinode of MW electric field in the resonator.

experiment [64], in the present experiment we can clearly resolve two modes in the reflection spectrum. One mode shows pronounced normal-mode splitting when the cyclotron frequency is close to the resonant frequency of the cavity $\omega_r/2\pi \approx 35.06$ GHz. The other mode shows a single dip when the excitation frequency ω is close to the resonant frequency ω_r and is nearly unaffected by the presence of electrons. It is clear that these two modes can be associated with the two circular-polarized components of the input linear-polarized MW signal. For a given direction of the perpendicular magnetic field B_0 only one of the two components (CR-active component) can excite the cyclotron resonance in 2DES, while another one (CR-passive component) should not affect the electron motion in the rotating wave approximation. Thus two modes in the reflection spectrum shown in Fig. 1.4 can be associated with two circular-polarized components of the MW field in the cavity.

Figure 1.4 (right panel) shows the dc conductivity response of 2DES measured at the same conditions as the measurements of the power reflection shown on the left panel. In this experiment, an electrical current induced by the electron motion on the middle electrode of the Corbino disk was measured while a low-frequency driving voltage having the amplitude of 20 mV was applied to the center electrode. Unlike the power reflection measurements, which probes the coupled motion of the MW field in the cavity, in this experiment we probe the coupled motion of the electron system. Such a coupled motion is strongly affected only by the CR-active component of the MW field. The cyclotron motion of electrons introduce heating of the 2DES on liquid helium due to its slow energy relaxation. Such a heating strongly affects the dc conductivity of electrons, which causes a change in the electron current detected by the Corbino disk. Correspondingly, a strong dc conductivity response of 2DES is observed at the same ω_c and ω as the power reflection spectrum of the CR-active mode, c.f., two panels in Fig. 1.4. A surprising feature is the appearance of a strong response of the 2DES observed at $\omega_c \approx \omega \approx \omega_r$, which is also observed in the reflection spectrum of the CR-passive mode, see top panel. We will discuss this additional resonance in Section 1.6.

1.4 Classical description of coupled electron-mode motion

First, we consider a completely classical description of the coupled electron-mode motion. Our treatment is similar to that described previously [64], which is also similar to the earlier treatment by Shikin [66],but takes correct account for two independent circular polarization modes of the EM field in the resonator. In order to account for the observed experimental results we use a model of a 2DES system in a simplified FB resonator, see Fig. 1.5. In our model, the resonator is formed by two infinitely large mirrors located at a distance D apart. One of the mirrors located at $z = 0$, where z-direction is perpendicular to the mirrors, is partially-reflecting with the amplitude reflection coefficients r_1 and r_2 for the MWs incident on the mirror from $z > 0$ and $z < 0$, respectively. The corresponding transmission coefficients are $t_1 = 1 + r_1$ and $t_2 = 1 + r_2$. The second mirror (occupying the half-space at $z < -D$) is a good conductor with a finite electrical conductivity σ that accounts for internal (Ohmic) losses

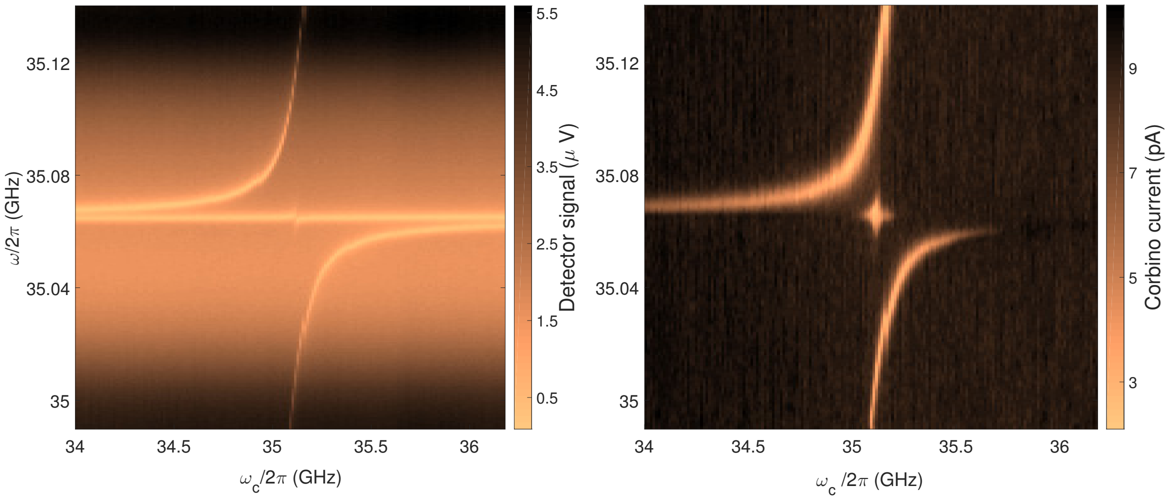

Figure 1.4: Power reflection from the cavity (top panel) and electron dc conductivity response (bottom panel) versus the cyclotron frequency of electrons ω_c and frequency of MW excitation ω measured at $T = 0.2$ K for surface density of electrons $n_s = 8.0 \times 10^7$ cm^{-2} and input MW power $P = -9$ dBm.

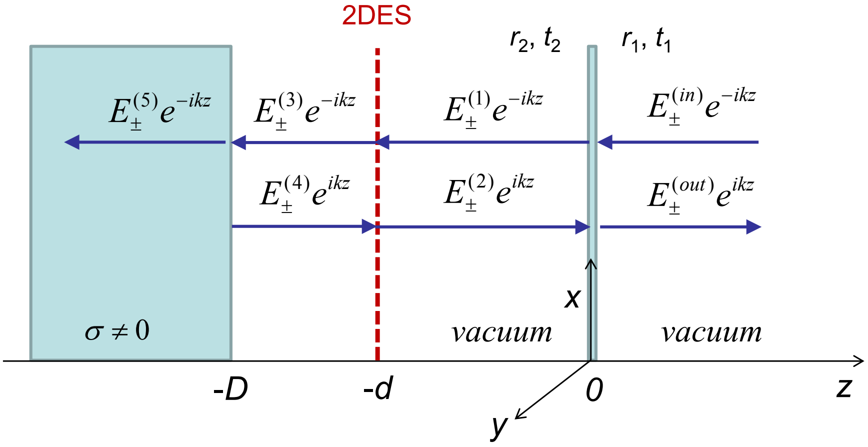

Figure 1.5: Simplified model of the Fabri-Perot resonator containing 2DES as described in the text. Thick arrows (blue) indicate the direction of propagation for different components of EM field inside and outside the resonator excited by the incoming field $\mathbf{E}_{\rm in} e^{-i(kz+\omega t)}$.

of MW field in the cavity. An infinitely large 2DES is located at $z = -d$, $d < D$, with the 2D plane oriented parallel to the plane of the mirrors, see Fig. 1.5. In simplicity, we neglect the presence of the dielectric liquid ^{3}He at $-D < z < -d$, whose dielectric constant is very close to that of vacuum ($\epsilon \approx 1.05$).

We will use notations for classical EM field similar to those introduced in Section 1.2.1. In order to account for the components of the EM field corresponding to two independent circular polarizations, we use the complex amplitudes $E_\pm = (E_x \pm iE_y)/\sqrt{2}$ and $j_\pm = 2^{-1/2}(j_x \pm ij_y)$ for the EM field and current density of electrons, respectively. The classical problem of EM field distribution inside and outside the resonator can be solved by considering the superposition of propagating waves and accounting for the boundary conditions at $z = -d$ and $-D$. Designating left- and right-propagating fields inside and outside resonator as indicated in Fig. 1.5 and employing the boundary conditions given by Eqs. (1.6) we obtain

$$E_\pm^{(1)} = t_1 E_\pm^{\text{in}} + r_2 E_\pm^{(2)}, \tag{1.32a}$$

$$E_\pm^{\text{out}} = r_1 E_\pm^{\text{in}} + t_2 E_\pm^{(2)}, \tag{1.32b}$$

$$E_\pm^{(1)} e^{ikd} + E_\pm^{(2)} e^{-ikd} = E_\pm^{(3)} e^{ikd} + E_\pm^{(4)} e^{-ikd}, \tag{1.32c}$$

$$-E_\pm^{(3)} e^{ikd} + E_\pm^{(4)} e^{-ikd} + E_\pm^{(1)} e^{ikd} - E_\pm^{(2)} e^{-ikd} = \eta_0 j_\pm, \tag{1.32d}$$

$$E_\pm^{(3)} e^{ikD} + E_\pm^{(4)} e^{-ikD} = E_\pm^{(5)} e^{i\kappa D}, \tag{1.32e}$$

$$-E_\pm^{(3)} e^{ikD} + E_\pm^{(4)} e^{-ikD} = -\frac{\eta_0}{\eta} E_\pm^{(5)} e^{i\kappa D}, \tag{1.32f}$$

where $\eta_0 = \sqrt{\mu_0/\varepsilon_0} = 377$ Ohm is the intrinsic impedance of vacuum, $k = \omega/c$ is the propagation constant in vacuum ($c = 1/\sqrt{\epsilon_0\mu_0}$ is the speed of light in vacuum), $\kappa = \sqrt{\mu_0}\omega/\eta$ is the propagation constant in conductor, and η is the intrinsic impedance of conductor:

$$\eta \approx \sqrt{\frac{\omega\mu_0}{2\sigma}}(1-i), \quad \frac{1}{\eta_0}\sqrt{\frac{\omega\mu_0}{2\sigma}} << 1. \tag{1.33}$$

The third and forth lines in Eq.(1.32) express continuity of electric field and discontinuity of magnetic field, respectively, at $z = -d$. The latter is due to non-zero electric surface current in 2DES. The fifth and sixth lines express continuity of electric and magnetic fields, respectively, at $z = -D$.

From Eq. (1.32) we can obtain relations between the E-field in the cavity at $z = -d$ for each of two circular-polarized modes, $E_\pm = E_\pm^{(1)} e^{ikd} + E_\pm^{(2)} e^{-ikd}$, and the corresponding components $j_\pm$ of the electron current density. Calculations are significantly simplified if we consider the frequency ω being close to $\omega_0 = c\pi m/D$, where $m = 1, 2, ..$ is the cavity mode number. Note that for an empty cavity each m-th mode is twice degenerate with respect to two independent polarization modes E^+ and E^-. In addition, we consider that 2DES is located at distance $\lambda_0/4 = c\pi/(2\omega_0)$ from the second mirror, that is at the antinode of the electric field. Finally, we assume that $r_1 \approx 1$ (that is $t_1 \approx 2$) and $r_2 \approx -1$ (that is $t_2 << 1$). Expanding in the first order of $(\omega - \omega_0)/\omega_0$,

$\sqrt{\omega\mu_0/(2\sigma)}/\eta_0$, and t_2, it is straightforward to obtain the required relation

$$\frac{D}{c}\Big(i(\omega-\omega_r)-(\gamma_{int}+\gamma_{ext})\Big)E^{\pm}-\eta_0 j_{\pm}=2i(-1)^m E^{\text{in}}_{\pm}, \tag{1.34}$$

where $\omega_r=\omega_0-\delta\omega_{int}-\delta\omega_{ext}$ is the resonant frequency of cavity,

$$\delta\omega_{int}=\frac{\omega_0}{\pi m}\sqrt{\frac{\omega\varepsilon_0}{2\sigma}}, \quad \delta\omega_{ext}=-\text{Im}\left(\frac{\omega_0}{2\pi m}t_2\right), \tag{1.35}$$

and

$$\gamma_{int}=\frac{\omega_0}{\pi m}\sqrt{\frac{\omega\varepsilon_0}{2\sigma}}, \quad \gamma_{ext}=\text{Re}\left(\frac{\omega_0}{2\pi m}t_2\right), \tag{1.36}$$

are internal (Ohmic) and external (radiative) loss rates of the resonator, respectively.

Eq. (1.34) gives us the first coupled relation between the EM field of the resonator mode and the current density of electrons. The second one is simply given by $j_{\pm}=\sigma_{\pm}E_{\pm}$, where the ac conductivity is given by Eq. (1.27). Thus, we obtain a system of coupled equations for electron-mode motion

$$\begin{pmatrix} \frac{D}{c}\Big[i(\omega-\omega_r)-(\gamma_{int}+\gamma_{ext})\Big] & -\eta_0 \\ n_s e^2/m_e & i(\omega\pm\omega_c)-\nu \end{pmatrix}\begin{pmatrix} E^{\pm} \\ j_{\pm}\end{pmatrix} = \begin{pmatrix} 2i(-1)^m E^{\text{in}}_{\pm} \\ 0 \end{pmatrix} \tag{1.37}$$

In the absence of external drive, $E^{\text{in}}_{\pm}=0$, the nontrivial solutions for $E^{\pm}$ and $j_{\pm}$ exist only for ω such that the determinant of the matrix in the left-hand-side of Eq. (1.37) vanishes. This provides frequencies $\omega_{1,2}$ for normal (eigen) modes of the coupled electron-field motion. It is instructive to find these frequencies for the case of zero losses, that is $\nu=0$ and $\gamma_{int}+\gamma_{ext}=0$. Then, we obtain

$$(\omega-\omega_r)(\omega\pm\omega_c)-\frac{n_s e^2}{m_e\varepsilon_0 D}=0. \tag{1.38}$$

For $\omega_c\approx\omega_r$, two solutions $\omega_{1,2}=\omega_r\pm g$, where

$$g=\sqrt{\frac{n_s e^2}{m_e\varepsilon_0 D}}, \tag{1.39}$$

are realized for the E^- mode. For this mode, the normal-mode splitting in the spectrum of coupled electron-field motion is given by $2g$. As discussed in Section 1.2.1, this mode corresponds to RHCP electric field which rotates in the same direction as electrons in the static magnetic field $\boldsymbol{B}_0$ oriented in positive z-direction. In other words, this corresponds to the CR resonance of electrons coupled to the CR-active (E_-) mode. The CR-passive (E^+) mode does not have any splitting as expected.

For the sake of comparison with the experimental results we derive an expression for the normalized power reflection, which we define as the ratio between the time-averaged output and input MW powers, $P_{\mathrm{R}} = \mathbf{E}_{out}\mathbf{E}^*_{out}/(\mathbf{E}_{in}\mathbf{E}^*_{in})$. From Eqs. (1.32) we obtain

$$E_{\pm}^{\mathrm{out}} = \left(1 - \frac{2(\delta\omega_{ext} + i\gamma_{ext})}{(\omega - \omega_r) + i\gamma + i\eta_0\sigma_{\pm}c/D}\right) E_{\pm}^{\mathrm{in}}, \tag{1.40}$$

where $\gamma = \gamma_{int} + \gamma_{ext}$ is the total loss rate of the cavity. Assuming linearly polarized (along x-axis) input MW field with $E_+^{\mathrm{in}} = E_-^{\mathrm{in}} = E_0/\sqrt{2}$, we obtain

$$\begin{aligned} P_{\mathrm{R}} =& \frac{\left|E_{out}^{+}\right|^2 + \left|E_{out}^{-}\right|^2}{E_0^2} \\ =& \frac{1}{2}\left|1 + \frac{2(\gamma_{ext} - i\delta\omega_{ext})}{i(\omega - \omega_r) - \gamma - \frac{\sigma_+}{\varepsilon_0 D}}\right|^2 + \frac{1}{2}\left|1 + \frac{2(\gamma_{ext} - i\delta\omega_{ext})}{i(\omega - \omega_r) - \gamma - \frac{\sigma_-}{\varepsilon_0 D}}\right|^2 . \end{aligned} \tag{1.41}$$

Similarly, the time-averaged power of Joule heating of 2DES due to MW electric field is given by

$$\begin{aligned} P_{\mathrm{J}} =& \langle \mathrm{Re}(\mathbf{j})\mathrm{Re}(\mathbf{E})\rangle_t \\ =& \frac{1}{2}\left(\mathrm{Re}(\sigma_+)|E^+|^2 + \mathrm{Re}(\sigma_-)|E^-|^2\right). \end{aligned} \tag{1.42}$$

The numerical solutions for P_{R} and P_{J} obtained by solving Eq. (1.37) for $n_s = 6 \times 10^7$ cm^{-2}, $\nu = 8 \times 10^7$ s^{-1} and $Q = 20,000$ are shown in Fig. 1.6. As seeing from comparison with Fig. 1.4, our completely classical model reproduces the main features of the experimental results. In particular, it reproduces the normal-mode splitting observed in both cavity field and electron system responses.

As seen from comparison with Fig. 1.4, our model does not reproduce an additional resonance appearing in both the reflection spectrum of the CR-passive LHCP mode and the dc conductivity response of electrons. This resonance will be addressed in Section 1.6.

1.5 Full quantum mechanical description of coupled electron-mode motion

In this section, we present the full quantum mechanical treatment of the coupled electron-mode motion and compare our results with the corresponding classical treatment, as well as our experimental results. After formulating the quantum mechanical Hamiltonian for the coupled system, we use quantum Langevin approach to formulate the coupled equations of motion, as well as input-output formalism to relate input and output cavity fields.

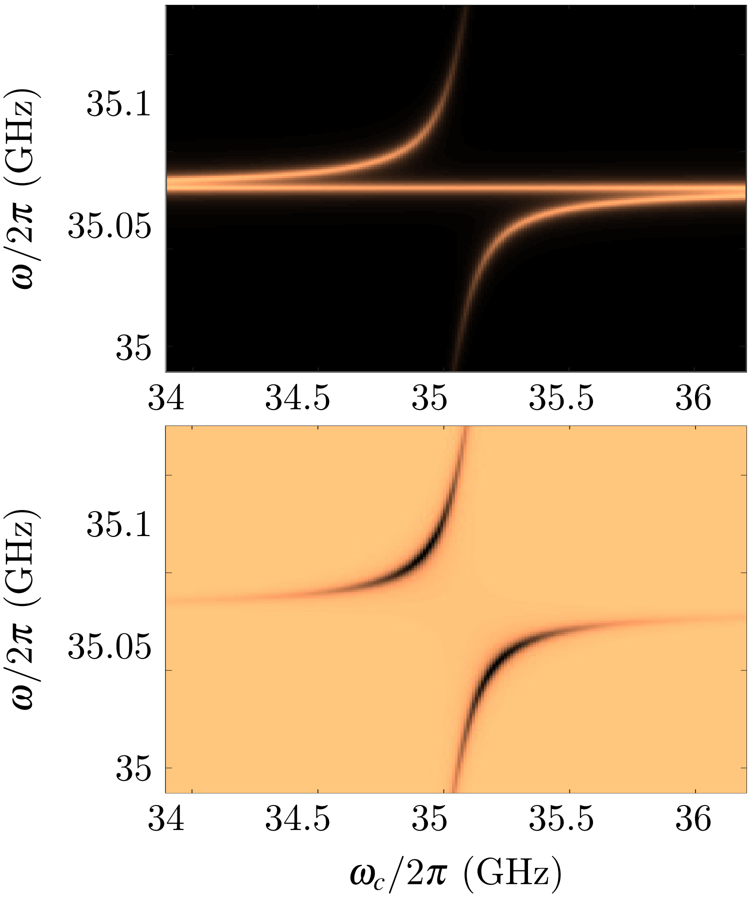

Figure 1.6: Power reflection from the cavity (top panel) and power of Joule heating of 2DES by MW field (bottom panel) versus the cyclotron frequency of electrons ω_c and frequency of MW excitation ω calculated from Eqs. (1.37), (1.41) and (1.42) for $n_s = 6 \times 10^7$ cm^{-2}, $\nu = 8 \times 10^7$ s^{-1} and $Q = 20,000$.

1.5.1 Hamiltonian of coupled oscillator system

We start with the description of EM field inside the model optical resonator shown in Fig. 1.4. As described in Section 1.2.1, the EM field inside an empty single-mode resonator can be described by an operator of vector potential

$$\hat{\boldsymbol{A}}(z,t) = \sqrt{\frac{\hbar\omega_0}{2\epsilon_0 V}} \sum_\alpha \left(\boldsymbol{e}_\alpha f(z)\hat{a}_\alpha(t) + \boldsymbol{e}^*_\alpha f^*(z)\hat{a}^\dagger_\alpha(t) \right), \tag{1.43}$$

where sum is over two polarization degrees of freedom described by the complex polarization vectors $\boldsymbol{e}_\alpha$. For example, as discusses in Section 1.2.1 $\boldsymbol{e}_\pm = (2^{-1/2})(\boldsymbol{e}_x \mp i\boldsymbol{e}_y)$ represent the LHCP and RHCP fields. We will use notations $\hat{a}_\mathrm{R}$ and $\hat{a}_\mathrm{L}$ for the corresponding photon operators. The normalized function $f(z) = i\sqrt{2}\sin(k_0 z)$, where $k_0 = \pi m/D$, $m = 1, 2, ..$, describes the spatial distribution of the electric field of the m-th mode (see Section 1.2.1). Under the Coulomb gauge condition, $\nabla\boldsymbol{A} = 0$ and $\boldsymbol{\nabla}\phi = 0$, the Hamiltonian of the system composed of a single EM mode and N-electron system can be written as

$$\begin{aligned} \hat{H} &= \hbar\omega_r \sum_\alpha \hat{a}^\dagger_\alpha \hat{a}_\alpha + \frac{1}{2m_e} \sum_e \left(\hat{\boldsymbol{\pi}} + e\hat{\boldsymbol{A}} \right)^2 \\ &\approx \hbar\omega_r \left(\hat{a}^\dagger_\mathrm{L}\hat{a}_\mathrm{L} + \hat{a}^\dagger_\mathrm{R}\hat{a}_\mathrm{R} \right) + \hbar\omega_c \sum_e \hat{b}^\dagger\hat{b} + \hbar g_0 \sum_e \left(\hat{b}\hat{a}^\dagger_\mathrm{R} + \hat{b}^\dagger\hat{a}_\mathrm{R} \right), \end{aligned} \tag{1.44}$$

where we adopted notations used in previous section for the frequency of resonant cavity mode $\omega_r \approx k_0/c$. We used the rotating wave approximation (RWA), and neglect the $\mathbf{A}^2$ term in the Hamiltonian. The single-electron coupling constant is given by $g_0 = \sqrt{e^2\omega_c/(m_e\epsilon_0\omega_r V)}$. The interaction term in the above equation can be viewed as an exchange of a quantum of excitation between the electron cyclotron and the cavity RHCP field. In RWA, the counter-rotating field of LHCP mode does not contribute to the interaction. We will reexamine possible contribution of this mode later. Finally, as in the previous section we assumed that electrons are located in the antinode of the electric field of the EM mode, thus $|f(z_e)|^2 = 2$.

1.5.2 Coupled equations of motion

Next, we write the Heisenberg equations of motion for time-dependent operators $\hat{a}_\mathrm{L}$ and $\hat{b}$ as

$$\dot{\hat{a}}_\mathrm{R} = (-i\omega_r - \gamma)\hat{a}_\mathrm{R} - ig_0 N\hat{b} + \hat{F}_a, \tag{1.45a}$$

$$\dot{\hat{b}} = -ig_0\hat{a}_\mathrm{R} + (-i\omega_c - \nu)\hat{b} + \hat{F}_b. \tag{1.45b}$$

Here, we use the quantum Langevin equation and introduce the Langevin noise operators $\hat{F}_a$ and $\hat{F}_b$, which vanish in the corresponding mean value equations, as well as the phenomenological relaxation rates γ and ν, in order to account for interaction of the system with environment [67]. The above equations describe two coupled harmonic oscillators with frequencies ω_r and ω_c. It is easy to check that the corresponding equations for mean values of operators $\hat{a}_{\mathrm{L}}$ and $\hat{b}$ obtained from (1.45) are equivalent to our classical equations (1.37) for complex amplitudes E^- and j_-. Indeed, it is easy to see that the operators corresponding to these quantities are given by the Fourier components of operators $\hat{j}_-$ and $\hat{E}^- = i\sqrt{2}E_{\mathrm{vac}}\hat{a}_{\mathrm{R}}$, where $E_{\mathrm{vac}} = \sqrt{\hbar\omega/(2\epsilon_0 V)}$ (see Section 1.2.1). Using equations of motion (1.45), we obtain

$$\begin{aligned} &[i(\omega-\omega_r)-\gamma]\,\langle \hat{E}^-(\omega)\rangle - \frac{2E_{\mathrm{vac}}^2 S}{\hbar\omega_r}\langle \hat{j}_-(\omega)\rangle = 0, \\ &\frac{e^2\omega_c N}{m_e\omega_r S}\langle \hat{E}^-(\omega)\rangle + [i(\omega-\omega_c)-\nu]\,\langle \hat{j}_-(\omega)\rangle = 0. \end{aligned} \tag{1.46}$$

The above system of coupled equations for the mean-values of quantum mechanical operators is similar to the classical coupled equations (1.37), see Section 1.4. Note that from Eqs. (1.46) the normal mode splitting is given by

$$g = \sqrt{\frac{2e^2E_{\mathrm{vac}}^2\omega_c N}{m_e\hbar\omega_r^2}}. \tag{1.47}$$

The relation of this result to the classical expression Eq. (1.39) will be discussed in Section 1.7.

In order to include an external pumping to our model, it is convenient to use Collect and Gardiner's approach, which allows to obtain relation between the input and output fields [68]. We consider a one sided cavity for which the main source of loss (with the rate γ) is coupling to external field. In this case, the boundary condition at the coupling port reads

$$\sqrt{2\gamma}\hat{a}_{\mathrm{R(L)}}(t) = \hat{a}^{(\mathrm{in})}_{\mathrm{R(L)}}(t) + \hat{a}^{(\mathrm{out})}_{\mathrm{R(L)}}(t), \tag{1.48}$$

which is consistent with boundary conditions (1.32a). Note that operators for external (in and out) fields are normalized such as $\hat{a}^\dagger\hat{a}$ gives the in(out)coming number of photons per second. The equations of motion for operators $\hat{a}_{\mathrm{R(L)}}$ and $\hat{b}$ lead to the linear algebraic equations for the corresponding Fourier transforms $\boldsymbol{u} = (\hat{a}_{\mathrm{R}}(\omega), \hat{a}_{\mathrm{L}}(\omega), \hat{b}(\omega))$, which can be written in the matrix form as $M\boldsymbol{u} = -\sqrt{2\gamma}\boldsymbol{u}^{(\mathrm{in})}$, where

$$M = \begin{pmatrix} i(\omega-\omega_r)-\gamma & 0 & -ig_0N \\ 0 & i(\omega-\omega_r)-\gamma & 0 \\ -ig_0 & 0 & i(\omega-\omega_c)-\nu \end{pmatrix}. \tag{1.49}$$

The solution for $\boldsymbol{u}^{(\mathrm{in})} = (\hat{a}^{(\mathrm{in})}_{\mathrm{R}}(\omega), \hat{a}^{(\mathrm{in})}_{\mathrm{L}}(\omega), 0)$, which can be obtained by simply inverting the matrix M, reads

$$\hat{a}_{\mathrm{R}}(\omega) = \frac{\sqrt{2\gamma}(\nu - i(\omega - \omega_c))}{\left(i(\omega - \omega_r) - \gamma\right)\left(i(\omega - \omega_c) - \nu\right) + g_0^2 N}\hat{a}_{\mathrm{R}}^{(\mathrm{in})}(\omega), \tag{1.50a}$$

$$\hat{a}_{\mathrm{L}}(\omega) = \frac{\sqrt{2\gamma}}{\gamma - i(\omega - \omega_r)}\hat{a}_{\mathrm{L}}^{(\mathrm{in})}(\omega), \tag{1.50b}$$

$$\hat{b}(\omega) = -\frac{ig_0\sqrt{2\gamma}}{\left(i(\omega - \omega_r) - \gamma\right)\left(i(\omega - \omega_c) - \nu\right) + g_0^2 N}\hat{a}_{\mathrm{R}}^{(\mathrm{in})}(\omega). \tag{1.50c}$$

Using the above equations together with the boundary condition (1.48), we obtain the linear input-output relations for two polarization modes

$$\frac{\hat{a}_{\mathrm{R}}^{(\mathrm{out})}}{\hat{a}_{\mathrm{R}}^{(\mathrm{in})}} = -1 - \frac{2\gamma(i(\omega - \omega_c) - \nu)}{\left(i(\omega - \omega_r) - \gamma\right)\left(i(\omega - \omega_c) - \nu\right) + g_0^2 N}, \tag{1.51a}$$

$$\frac{\hat{a}_{\mathrm{L}}^{(\mathrm{out})}}{\hat{a}_{\mathrm{L}}^{(\mathrm{in})}} = \frac{(\omega - \omega_r) - i\gamma}{(\omega - \omega_r) + i\gamma}. \tag{1.51b}$$

The normalized power reflection is given by $P_{\mathrm{R}} = \langle \hat{a}^{(\mathrm{out})\dagger}\hat{a}^{(\mathrm{out})}\rangle / \langle \hat{a}^{(\mathrm{in})\dagger}\hat{a}^{(\mathrm{in})}\rangle$, which results in the same relations as for classical quantities, see Eq. (1.40). The time-averaged power absorbed by the electron system from MW field is given by

$$P_{\mathrm{J}} = \langle \hat{\mathbf{j}} \cdot \hat{\mathbf{E}} \rangle = -\frac{i\hbar g_0 \omega_c n_s}{D}\langle \hat{b}^{\dagger}\hat{a}_{\mathrm{R}} - \hat{b}^{\dagger}\hat{a}_{\mathrm{R}}^{\dagger}\rangle. \tag{1.52}$$

The above equations completely reproduce results obtained from the classical treatment and shown in Fig. 1.6.

1.6 Additional resonance

We have shown that both classical and full quantum models reproduce the result of the normal mode splitting due to coupling between the cyclotron motion of electrons and RHCP cavity mode, see Fig. 1.6. However, the experimental data shown in Fig. 1.5 exhibit an additional resonance peak when the MW frequency ω is close to both the cavity frequency ω_r and cyclotron frequency ω_c. This result indicates that there is an effective coupling between the electron motion and CR-passive LHCP mode of the cavity.

This visible deviation from the ideal model can be explained by several mechanisms. The leading contribution comes from the spatial inhomogeneity of the MW field on the surface of liquid helium inside our experimental cell. The cylindrical copper cell in our setup, see Fig. 1.3(b), has a diameter of the same order of magnitude as the MW wavelength. As an illustration, the numerical simulation of the field distribution inside the cell using boundary conditions imposed by the cell confinement is plotted in Fig. 1.7(left panel). Here, we used a linearly polarized field as the input field. Clearly, the field inside the cavity does not preserve the linear polarization. Similarly, in Fig. 1.7(right panel) we show the polarization profile of the MW field for a pure

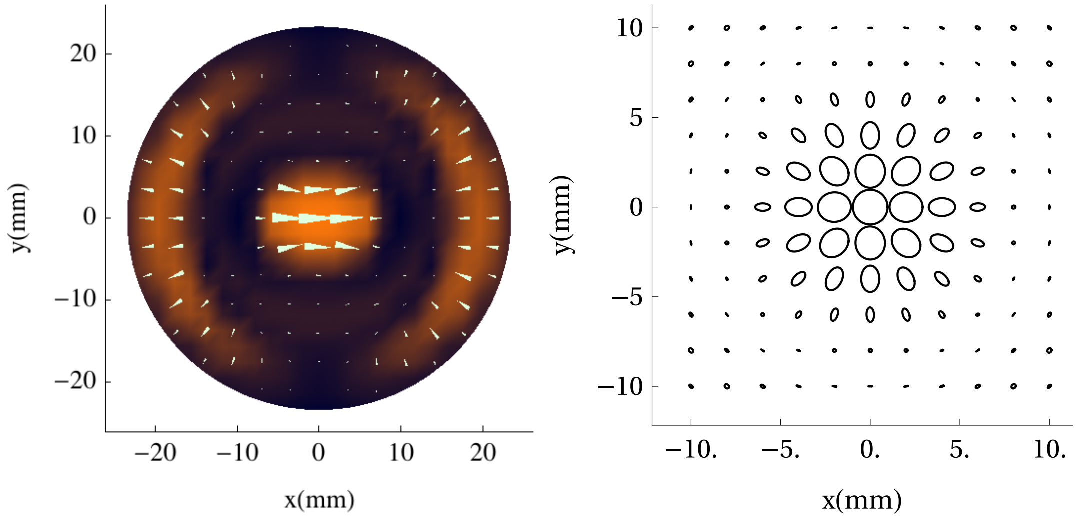

Figure 1.7: (left panel) Distribution of MW electric field on the surface of liquid helium inside the experimental cell under excitation with linearly (x-direction) polarized field. (right panel) Polarization of MW electric field on the surface of liquid helium under excitation with CP field.

circularly-polarized (CP) field as the input field. It clearly shows that the field is not circularly polarized everywhere inside the cell. The physical explanation of this is simple. According to the boundary conditions Eqs. 1.6 the MW electric field must be always perpendicular to the conducting walls of the cylindrical cell, which is impossible to satisfy for the pure CP mode. Therefore, interaction of the CP mode with the conducting walls produces an admixture with the opposite polarization.

That means the cyclotron motion away from the center can also have an effective coupling to the CR-passive mode. One can account for this effect by a small modification to the interaction term (1.44) to reflect the spatial dependence of the coupling between $\hat{b}$ and $\hat{a}_{(R/L)}$. The interaction part of the Hamiltonian reads,

$$\hat{H}_I = \sum_i \hbar \left(g_R^{(i)} \hat{b}^{(i)} \hat{a}_R^\dagger + g_L^{(i)} \hat{b}^{(i)} \hat{a}_L^\dagger \right) + H.c., \tag{1.53}$$

where $g_{R(L)}^{(i)}$ is a function of the position of particle i. In polar coordinate the interaction Hamiltonian reads

$$\hat{H}_I = \int_0^{2\pi} \mathrm{d}\phi\, r \int_0^{R_0} \mathrm{d}r\, \hat{\mathbf{A}}(r,\phi) \cdot \hat{\mathbf{j}}(r,\phi), \tag{1.54}$$

where ϕ is the azimuthal radian, r is the distance for the center, R_0 is the inner radius of the cavity.

In our cylindrical cavity, 2DES formed a pool of charge with diameter about 5 mm at the center of the cell. In our simulations, we assumed that charge was uniformly distributed in a circle of radius 5 mm around the center of the FB cavity. The power reflection and the power of Joule heating were numerically calculated from the mean value equations by the similar method used in Eq. (1.50). The results of our simulations are plotted in Fig. 1.8. Comparison with Fig. 1.4 shows that our simulations reproduce

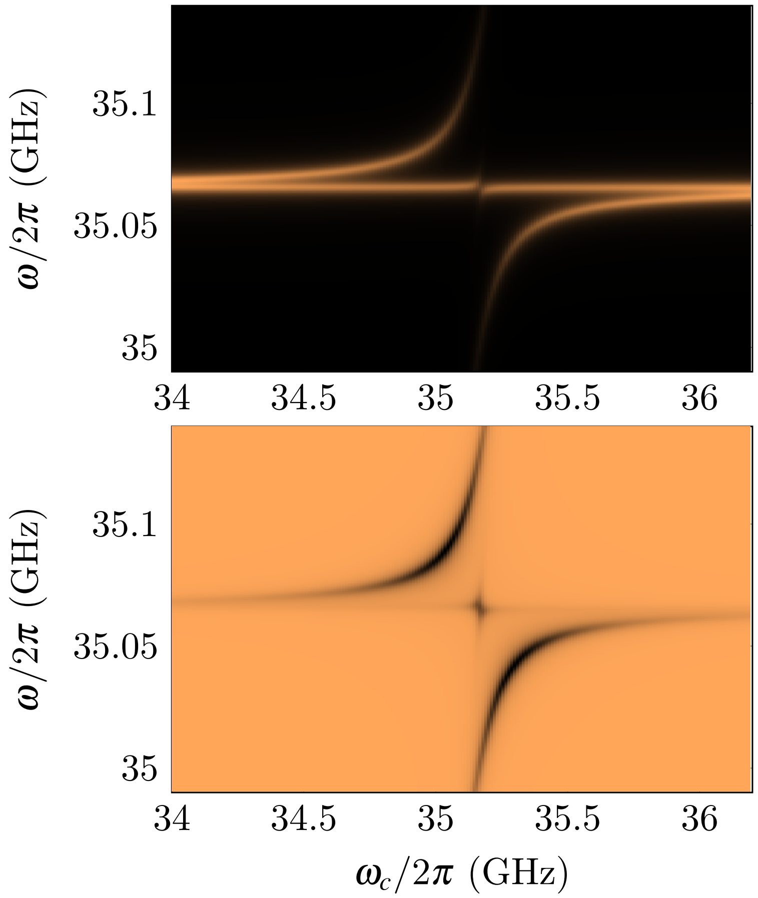

Figure 1.8: Power reflection from the cavity (top panel) and power of Joule heating of 2DES by MW field (bottom panel) versus the cyclotron frequency of electrons ω_c and frequency of MW excitation ω, calculated using the model with spatially inhomogeneous electromagnetic field and interaction term described by Eq. (1.54).

all the main feature of the additional resonance appearing in the CR-passive LHCP mode.

1.7 Discussion

In this Chapter, we described an experiment to realize the regime of strong coupling between a many-electron system and EM mode in an optical resonator, as manifested by the normal-mode splitting in spectrum of the coupled electron-mode motion. We also showed that both the classical and full quantum description of the coupled system give equivalent results, as well as completely accounts for all the experimental observations.

To illustrate the equivalence of two theoretical approaches further, let us examine the expression for the coupling constant g which quantifies the observed normal-mode splitting. Near the crossing point, $\omega_r \approx \omega_c$, the full quantum expression (1.47) gives

$$g \approx \sqrt{\frac{2e^2 E_{\rm vac}^2 N}{m_e \hbar \omega_c}} = \frac{\sqrt{2} e l_B E_{\rm vac}}{\hbar} \sqrt{N}. \tag{1.55}$$

On the one hand, this expression has a quantum mechanical meaning of a $\sqrt{N}$-enhanced coupling of a single-electron dipole el_B to the r.m.s. electric field of vacuum $E_{\rm vac}$, see Section 3.1. On the other hand, by using the definition of $E_{\rm vac} = \sqrt{\hbar\omega/(2\epsilon_0 V)}$, we completely reproduce the classical result for g given by Eq. (1.39). Note that the Plank's constant $\hbar$ drops out from the expression for g.

The complete equivalence of the full quantum and classical descriptions of the coupled linear quantum system discussed in this section is not surprising. Indeed, the linearity of the obtained equations of motion for quantum-mechanical operators allows one to construct closed mean-value equations for observables which completely correspond to the classical equations of motion. The complete agreement of the classical approach with the experiment is also not surprising since the input EM field is in a classical coherent state and there are no considerable non-linear effects in our experiment. Still, the regime of strong coupling demonstrated in our experiments can provide possibilities to create and manipulate non-classical states of 2DES by introducing nonlinearities in the system, e.g. coupling the cyclotron motion to a degree of freedom with effective two-level energy spectrum. Some theoretical models for such nonlinear systems will be discussed in Chapter 2, while in Chapter 3 we describe our further experiments with 2D electrons on helium to explore possibilities for observing quantum effects of light-matter interaction in this system.

It is worthwhile to mention that in our calculation, we didn't need to consider the Coulomb interaction between the electrons and the interaction between electrons and the helium surface excitations. For example, two-dimensional plasmons exist due to the interaction among the SEs, which was experimentally observed by Grimes *et al* [69]. This phenomenon can shift the frequency of the cyclotron resonance. The changes in CR linewidth and peak position against the pressing field $E_\perp$ provides information about the effective mass of SEs and about their coupling to the helium surface motion. This was demonstrated in Édel'man's experiments in [70] and [71]. In our experiment these shifts are small and thus can be ignored. However, these interactions might be interesting for future investigation.

Chapter 2

Adiabatic Preparation of squeezed states

2.1 Overview

We showed in the experiment detailed in Chapter 1 the strong coupling between two quantum harmonic oscillators, i.e., the strong coupling between the cyclotron motion of surface electrons on liquid helium and the microwave photons in the cavity. The experimental realization of strong coupling to photons in a quantum system is one of the prerequisites for implementing some protocol of coherent control of matter using light. In this chapter, we deviate from the experiments and focus on developing theoretical protocols that have potential use in experimental systems including the surface electron system on liquid helium. I will present a theoretical study about the use of a single two-level system coupled to an oscillator mode or coupled to a collective spin in order to generate squeezed states by slowly changing the driving terms. The results of this study are published in [72][1].

This chapter is structured as follows. Section 2.2 briefly explains why we study the adiabatic preparation of squeezed states using Jaynes-Cummings-type systems. Section 2.3 introduces the theoretical model and related concepts. In Section 2.4, we introduce the Hamiltonian and identify the analytical solution for the eigenstate that is followed adiabatically by the system. The system is prepared in the ground state of the Jaynes-Cummings Hamiltonian, and subject to a gradually increased resonant driving of the oscillator mode until a maximum critical strength. In Section 2.5, we study the case of a two-level system coupled to an effective large collective spin, for which the initial ground state also transforms adiabatically through a sequence of eigenstates, and for which one may explore system eigenstates for all driving strengths. Finally, Section 2.6 contains the conclusions and an outlook for this chapter.

2.2 Motivation

How might one prepare and manipulate the quantum states of matter using precisely controlled light-matter interactions, especially into non-classical states which can be

---

[1] This chapter describes joint work with Prof. Klaus Mølmer, Aarhus University.

used for high precision measurements and quantum information processing? This question can be answered by studying various simple theoretical models. One of the simplest non-trivial interacting quantum mechanical models is the one that contains a two-level system(TLS) and a quantized harmonic oscillator (HO) mode which couples strongly to that TLS. Yet, this minimalistic model can describe a wide range of experimental physical systems. Among them are atoms in cavities (cavity QED) [12, 13], cold trapped ions [14, 15], superconducting qubits in microwave resonators (circuit QED) [17], electrons on liquid helium [26, 27], and many others [73]. In this chapter, we are going to study experimental protocols that can be implemented in these systems to generate non-classical states called squeezed states.

Squeezed states of an oscillator mode are non-classical states, for which the fluctuations in one of its quadratures are smaller than that of a coherent state [74–77]. Squeezed states of light hold potential for high precision optical measurements, and squeezed microwave fields were recently shown to enhance the sensitivity in electron spin resonance experiments [78]. The robust generation of such states is of interest in many experimental systems with applications for sensing and quantum information processing.

In the Section 2.4, we use the Jaynes-Cummings Model (JCM) [79], which describes the interaction between the TSL and the HO with the rotating wave approximation (RWA). Even with the simplification brought on by the RWA in the JCM, one can see that the discrete nature of the bosonic mode leads to interesting features. These features include, the ‘collapse and revival’ of Rabi oscillations, demonstrated by atoms in microwave and optical cavities [12, 45, 80, 81], or coupling of the internal degree of freedom to the center-of-mass motion of ions [14, 15, 82]. The non-linearity induced by the two-level system causes an effective Kerr non-linearity. This leads to squeezing [83, 84], superpositions of coherent states of the oscillator [85], and, similar to classical nonlinear systems, bistability and phase transitions are also present in the JC model [86, 87].

We have investigated the generation of squeezed states by adiabatic evolution of a JC system subject to a slowly varying coherent drive on the oscillator component, in Sec. 2.4. In addition, we supplement the analysis of the oscillator with the study of a single two-level system coupled to a large spin. Which might describe, for example, a central spin coupled to the collective symmetric states of other spin $1/2$ particles in a spin-star configuration [88].

Collective spin squeezed states [89–91] have non-classical correlations (entanglement) between their spin $1/2$ constituents [92, 93], and they have been proposed for use in precision clocks and magnetometers, and as entanglement sources for quantum information protocols [6]. Spin squeezing of atomic ensembles may be obtained by suitably engineered interactions. Using Rydberg blockade interactions, the use of laser excitation pulses have been proposed to implement adiabatic protocols to drive a large system of atoms into spin squeezed and entangled states [94, 95].

In Section 2.5, we study a case analogous to the JCM, namely that of a classically driven spin interacting with a single two-level system, and we identify the states explored by this system under adiabatic variation of the interaction parameters. Unlike for the oscillator, the states of the large spin are always normalizable, but they evolve through spin squeezed and very non-classical quantum states.

2.3 Concepts and methods

In this section, we are going to review the technical backgrounds of a few subjects needed by the main part of the study. Firstly, we introduce the basics of quantum harmonic oscillator and its squeezed states in Subsection 2.3.1. This is followed by a brief review of the phase space representation of quantum states, which we use to visualize our results in this chapter. Then we proceed to use the Jaynes-Cummings model to describe the interaction between a two-level-system and the harmonic oscillator. In Subsection 2.3.4 we introduce the properties of the large collective spins, the spin squeezed states and their connections to harmonic oscillator.

2.3.1 Properties of quantum harmonics oscillators

Firstly we'll review some important properties of the HOs, and uncertainty relations in different states of HOs. Secondly, we define the phase space representations, so that it can be used to visualize the quantum states in a intuitive way. These are the concepts needed in Section 2.4.

The Hamiltonian of a harmonic oscillator can be written as

$$H_{HO} = \frac{P^2}{2m} + \frac{1}{2}m\omega^2 X^2 = \hbar\omega(a^\dagger a + \frac{1}{2}), \tag{2.1}$$

where X is the position operator, and $P \equiv -\mathrm{i}\hbar\partial/\partial X$ is the momentum operator. These operators follow the canonical commutation relation $[X, -\mathrm{i}\hbar\partial/\partial X] = i\hbar$.

The dimensionless annihilation operator a and its adjoint $a^\dagger$ for the HO are defined as

$$a \equiv \sqrt{\frac{m\omega}{2\hbar}}\left(X + \frac{i}{m\omega}P\right), \quad a^\dagger \equiv \sqrt{\frac{m\omega}{2\hbar}}\left(X - \frac{i}{m\omega}P\right), \tag{2.2}$$

so that they follow the simple commutation relation $\left[a, a^\dagger\right] = 1$.

The exact values of m and $\hbar$ are irrelevant to the discussions, in the rest of this chapter. The will be set to $\hbar = 1$, $m = 1$. I will also use observable x, p which correspond to position and momentum operator respectively,

$$x = (a + a^\dagger), \quad p = (a - a^\dagger)/\mathrm{i}. \tag{2.3}$$

With the definition of the HO, we are going to study the uncertainty of the observables in the different states of HOs including the Fock state, the coherent state and the squeezed state.

The uncertainty principle

The uncertainty of an observable is define by its standard deviation

$$\Delta A = \sqrt{\langle A^2\rangle - \langle A\rangle^2}, \tag{2.4}$$

where A is an Hermitian operator and $\langle A\rangle$ its expectation value.

One can show that [96]

$$\Delta A^2 \Delta B^2 \geq |\langle \delta A \delta B \rangle|^2 = \frac{1}{4}|\langle [A,B] \rangle|^2 + \frac{1}{4}|\langle \{\delta A, \delta B\} \rangle|^2, \tag{2.5}$$

where $\delta A \equiv A - \langle A \rangle$. This leads to the familiar uncertainty principle

$$\Delta A \Delta B \geq \frac{1}{2}|\langle [A,B] \rangle|. \tag{2.6}$$

Now we can see this uncertainty relation in the HO case. For the eigenstates of (2.1), i.e., the Fock state $a^\dagger a \left|n\right\rangle = n \left|n\right\rangle$, the uncertainty of x and p is simply

$$\Delta x_n^2 = \Delta p_n^2 = 2n + 1 \tag{2.7}$$

The ground state of HO, also called the vacuum state, $|n = 0\rangle$, reachs the equal sign in Eq. (2.6).

Coherent states

Coherent states of harmonic oscillators are the eigenstates of the non-hermitian annihilation operator in [97–99], defined as

$$a \left|\alpha\right\rangle = \alpha \left|\alpha\right\rangle. \tag{2.8}$$

Unlike number states with $n \geq 0$, coherent states can be generated by applying a spatially homogeneous periodic driving force to the harmonics oscillator, thus is the most ‘classical’ pure state.

Let $D(\alpha)$ be a unitary displacement operator

$$D(\alpha) \equiv \exp\big(\alpha a^\dagger - \alpha^* a\big) = e^{-|\alpha|^2/2} e^{\alpha a^\dagger} e^{-\alpha^* a}, \tag{2.9}$$

The a coherent state can be generated by applying the unitary displacement operator $D(\alpha)$ on the ground state $|0\rangle$, i.e.

$$\left|\alpha\right\rangle = D(\alpha) \left|0\right\rangle = e^{-|\alpha|^2/2} \sum \frac{\alpha^n}{\sqrt{n!}} \left|n\right\rangle, \tag{2.10}$$

where $a \left|0\right\rangle = 0$.

One can use a variation of the Baker–Campbell–Hausdorff formula to evaluate the transformation property of an operator. It reads

$$e^{\zeta B} A e^{-\zeta B} = A + \zeta [B, A] + \frac{\zeta^2}{2!}[B,[B,A]] + \cdots, \tag{2.11}$$

where B is an operator and ζ a number [100].

$$D^\dagger(\alpha) a D(\alpha) = a + \alpha, \quad D^\dagger(\alpha) a^\dagger D(\alpha) = a^\dagger + \alpha^* \tag{2.12}$$

The variance of the two quadrature in a coherent state $|\alpha\rangle$ should be the same as the ones in the vacuum state $|0\rangle$

$$\Delta x^2_{\mathrm{coh}} = \Delta p^2_{\mathrm{coh}} = 1. \tag{2.13}$$

Eq. (2.13) is the theoretical limit of variance for a classically driven harmonic oscillator or light, to further lower this value, one has to use non-classical quantum states, which are the squeezed states.

Squeezed state of a quantum harmonic oscillator

A squeezed state in general refers to the state in which one observable's fluctuation is reduced even compared to that of the coherent state [101, 102]

$$\Delta A < \frac{1}{2}|\langle[A,B]\rangle|. \tag{2.14}$$

Here the fluctuation of A is reduced at a cost of the increasing fluctuation in the other observable B.

Squeezed light is important for modern quantum applications, because it reduces the fluctuation of light to be below the classical limit. It allows us to push the precision of measurements further than what is allowed by using coherent light. One can read more about the development of squeezed light in quantum optics in the review papesr[103, 104].

One way of generating a squeezed state is by applying a unitary transformation of higher power of a and $a^\dagger$. For example

$$S(\zeta) = \exp\left[\tfrac{1}{2}(\zeta^* a^2 - \zeta a^{\dagger 2})\right] = \exp\left(\tfrac{\mathrm{i}}{2} r (X_\phi Y_{\phi+\pi/2} + Y_{\phi+\pi/2} Y_\phi)\right), \tag{2.15}$$

where $\zeta = re^{\mathrm{i}2\phi}$ for $r, \phi \in \mathbb{R}$.

$S(\zeta)$ has the useful transformation property:

$$S^\dagger(\zeta) a S(\zeta) = \cosh\zeta a + \sinh\zeta a^\dagger = a\cosh r - a^\dagger e^{2-\mathrm{i}\phi}\sinh r \tag{2.16}$$

which shows that 1) one can reduce the uncertainty of one quadrature by applying squeezing operator to a coherent state. 2) the eigenstate of linear combination of a and $a^\dagger$ can be obtained using $D(\alpha)$ and $S(\zeta)$.

It is useful to define

$$b \equiv ua + va^\dagger = \cosh\zeta a + \sinh\zeta a^\dagger, \tag{2.17}$$

which can have the canonical commutation relation $\left[b, b^\dagger\right] = 1$ if the constraint $|u|^2 - |v|^2 = 1$ is imposed. The uncertainty the two quadratures for the eigenstates of b is

$$\mathrm{Var}(x) = |u - v|^2, \quad \mathrm{Var}(p) = |u + v|^2, \tag{2.18}$$

when both μ and ν are real. These eigenstates of b are also called the generalized coherent state [75, 105, 106].

The squeezing of an arbitrary state is quantified by the squeezing parameter

$$\xi^2 = 2 \min_{\theta \in (0, 2\pi)} \mathrm{Var}(X_\theta) = \min_\theta \mathrm{Var}(a e^{-\mathrm{i}\theta} + a^\dagger e^{\mathrm{i}\theta}), \tag{2.19}$$

and for squeezed state $S(\zeta)\,|\alpha\rangle$ the squeezing parameter is

$$\xi = \cosh\zeta - \sinh\zeta = \exp(-\zeta), \tag{2.20}$$

for $\zeta > 0$.

2.3.2 Quasi-probability representation of quantum states and visualization

A quantum state cannot have a real probability distribution in the phase space in the same way as in a classical system, because the probability of finding a particle in a certain position and momentum in the same time is not well-defined. However, when relaxing the axiom of probability one may define quasi-probability distributions in the phase space to represent a quantum state in the phase space, such that . In this chapter, we choose to use Wigner function and Husimi Q-function to visualize the state which represents expectation values of symmetrically ordered and anti-normal ordered characteristic functions respectively [107, 108].

An arbitrary mixed or pure quantum state is defined by density matrix

$$\rho = \sum_i p_i \,|\psi_i\rangle\langle\psi_i|\,, \tag{2.21}$$

where the probabilities p_i are non-negative and add up to one.

The quasi-probability representation of ρ can be defined by Fourier transforms of the representations' corresponding characteristic functions [67]. For one-dimensional systems, the characteristic functions for the Wigner-function and the Husimi Q-function are

$$\chi(\eta) \equiv \left\langle e^{\eta a^\dagger - \eta^* a} \right\rangle = \mathrm{Tr}\Big(\rho e^{\eta a^\dagger - \eta^* a}\Big), \tag{2.22a}$$

$$\chi_A(\eta) \equiv \left\langle e^{-\eta^* a} e^{\eta a^\dagger} \right\rangle = \mathrm{Tr}\Big(\rho e^{-\eta^* a} e^{\eta a^\dagger}\Big), \tag{2.22b}$$

which are the expectation values of the displacement operator in Eq.(2.9). The operator in $\chi_A(\eta)$ is called anti-normal ordered, since the all the creation operators $a^\dagger$ are placed on the right side compared to the one in $\chi(\eta)$.

Here we denote $\alpha \equiv (x + \mathrm{i}p)/2$ as the coordinates in the phase space. The Wigner function $W(\alpha)$ and Husimi Q-function $Q(\alpha)$ naturally relate to their characteristic functions by the Fourier transforms:

$$W(\alpha) = \frac{1}{\pi^2} \int \exp(\eta^* \alpha - \eta \alpha^*) \chi(\eta) \mathrm{d}^2\eta \tag{2.23a}$$

$$Q(\alpha) = \frac{1}{\pi^2} \int \exp(\eta^* \alpha - \eta \alpha^*) \chi_A(\eta) \mathrm{d}^2\eta. \tag{2.23b}$$

Both $W(\alpha)$ and $Q(\alpha)$ have clear physical interpretations. One can recover the probabilities $P(x) = \langle x|\rho|x\rangle$ or $P(p) = \langle p|\rho|p\rangle$ by integrating over the variables p and x respectively

$$P(x) = \int_{-\infty}^{\infty} \mathrm{d}p W(x,p), \quad P(p) = \int_{-\infty}^{\infty} \mathrm{d}x W(x,p), \tag{2.24}$$

where we denote $W(x,p) \equiv W(\alpha)/4$ by convention.

In FIG. 2.1 we plot the Wigner functions of the vacuum state, a coherent state, a squeezed state, and a superposition of two coherent states (a cat state). In particular, in panel (d) we can see the oscillation between positive and negative values in $W(0,p)$, hinting that the interference pattern one would observe in the function $P(p)$.

The Q-function $Q(\alpha)$ can also be interpret as the overlap between ρ and a coherent state $|\alpha\rangle$. The equivalent definition for $Q(\alpha)$ reads

$$Q(\alpha) = \frac{1}{\pi} \langle\alpha|\rho|\alpha\rangle . \tag{2.25}$$

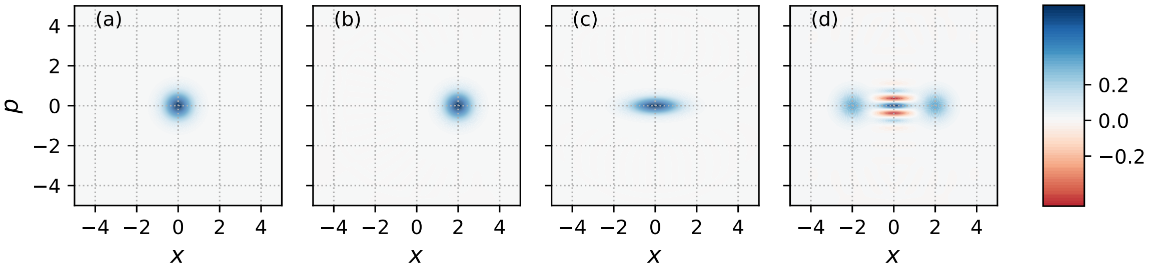

Figure 2.1: Wigner function representation of various pure states$|\psi_i\rangle$. (a) vacuum state $|\psi_a\rangle = |0\rangle$; (b) a coherent state $|\psi_b\rangle = D(\alpha = 2)|0\rangle$;(c) a squeezed state$|\psi_c\rangle = S(\zeta = -1/2)|0\rangle$;(d) a superposition of two coherent states $|\psi_d\rangle = \frac{1}{\sqrt{2}}(D(-2) + D(2))|0\rangle$.

In FIG. 2.2 we plot the Q-functions of the vacuum state, a coherent state, a squeezed state, and a superposition of two coherent states (a cat state). As opposed to $W(\alpha)$, $Q(\alpha)$ is non-negative. The Q-function provides a more direct measure of how the quantum state ρ is related to the set of coherent states $|\alpha\rangle$.

2.3.3 JCM and the coupling between a TSL and a HO

After reviewing the properties of the harmonics oscillator and its phase-space representations, in this subsection, we are going to introduce the interaction between the TSL and the HO and the JCM. This kind of interaction is common in many experiments. To give two examples, in Jaynes and Cummings' original paper [79], the atom interacts with a photon field inside an optical cavity via the electric dipole interaction. When the atom resonates at the same frequency as the cavity, excitations can be coherently exchanged between them. If the speed of this exchange exceeds dissipation, we say that it is in the strong coupling regime.

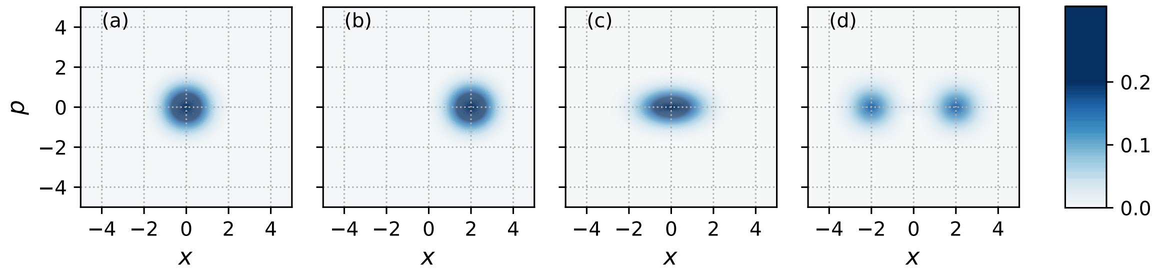

Figure 2.2: The Q-function representation of various pure states$|\psi_i\rangle$. (a) a vacuum state: $|\psi_a\rangle = |0\rangle$; (b) a coherent state: $|\psi_b\rangle = D(\alpha = 2)|0\rangle$;(c) a squeezed state$|\psi_c\rangle = S(\zeta = -1/2)|0\rangle$;(d) a superposition of two coherent states $|\psi_d\rangle = \frac{1}{\sqrt{2}}(D(-2) + D(2))|0\rangle$.

For trapped ions or electrons on Helium, instead of photons in optical cavity, the HO degrees of freedom can be used to describe the center-of-mass motion or the Landau Levels respectively. In this case, the TLS and the HO have different excitation energies. Because of energy conservation, the energy transfer between these two systems is facilitated by an external electromagnetic field that oscillates at the difference of the resonant frequencies of the TSL and the HO.

The JC Hamiltonian for an atom in an optical cavity in the Schrödinger picture reads

$$H_{JC} = \omega_a a^\dagger a + \frac{1}{2}\omega_0 \sigma_z + g_1(\sigma_+ a + \sigma_- a^\dagger), \quad (\hbar = 1) \tag{2.26}$$

where a and $a^\dagger$ are the annihilation and creation operators for a single radiation mode in the cavity resonator with frequency ω_a, and the $\sigma_{\pm,z}$ are the spin operators for the spin $\pm/z$ components for the two-level atom with frequency ω_0. The Pauli matrices are written explicitly as $\sigma_z = -|g\rangle\langle g| + |e\rangle\langle e|$, $\sigma_+ = |e\rangle\langle g|$, and $\sigma_- = |g\rangle\langle e|$, where we define $|g\rangle$ and $|e\rangle$ as the ground and excited states of the atomic TLS. The eigenstates of $a^\dagger a$ are labeled by $|n\rangle$, where n is the photon number. We denote $|n, m\rangle = |n\rangle \otimes |m\rangle$ as the product states of the TLS and HO, where $|m\rangle = |g\rangle$ or $|e\rangle$.

Note that for the Hamiltonian (2.26) the total excitation number operator $N \equiv a^\dagger a + \frac{1}{2} + \frac{1}{2}\sigma_z$ commutes with H_{JC}, making the total excitation number N a conserved quantity. As a result, H_{JC} can be written in a block diagonal form, in which each block is an invariant subspace spanned by $\{|n, e\rangle, |n+1, g\rangle\}$ except for the first block which is spanned only by $\{|0, g\rangle\}$.

In order to discuss the eigenstates and eigenvalues of H_{JC}, it is convenient to use a rotating frame, i.e., an interaction picture, in which H_{JC} is split into two parts

$$H_{JC,S} = H_{0,S} + H_{1,S}, \tag{2.27a}$$

$$H_{0,S} = \omega_a(a^\dagger a + \frac{1}{2}\sigma_z), \tag{2.27b}$$

$$H_{1,S} = \delta\frac{1}{2}\sigma_z + g_1(a\sigma_+ + a^\dagger\sigma_-), \tag{2.27c}$$

where $\delta \equiv \omega_0 - \omega_a$ is the detuning between the cavity and the atom.

For this we use the rule that an operator A is transformed under a unitary operation as

$$A_I = U^-1 A_S U, \quad U = \exp(-\mathrm{i} H_{0,S} t), \tag{2.28}$$

which for Eq. (2.26), and with $U = \exp\bigl[-\mathrm{i}\omega_a t(a^\dagger a + \frac{1}{2}\sigma_z)\bigr]$, it yields

$$H_{I,1} = \delta_a a^\dagger a + g_1(a\sigma_+ + a^\dagger \sigma_-). \tag{2.29}$$

We can diagonalize Eq. (2.29) using the fact that it has the conserved quantity N. In the rotating frame the block Hamiltonian $H^{(N)}$ reads

$$H_I^{(N)} = \begin{pmatrix} -\delta_a/2 & g_1\sqrt{n+1} \\ g_1\sqrt{n+1} & \delta_a/2 \end{pmatrix}. \tag{2.30}$$

which has the eigenstates

$$\begin{aligned} |0\rangle &= |g, 0\rangle\,, \\ |N, \pm\rangle &= \sin(\theta_n/2)\,|n+1, g\rangle \pm \cos(\theta_n/2)\,|n, e\rangle\,, \end{aligned} \tag{2.31}$$

where $\theta_n \equiv \arctan\bigl(2g_1\sqrt{n+1}/\delta\bigr)$.

The eigenvalues of $H_{1,I}$, i.e., the 'equasi-eigenergy' are

$$\begin{aligned} E_0 &= 0 \\ E_{N,\pm} &= \pm\frac{1}{2}\sqrt{\delta^2 + 4g_1^2 N}, \quad N = 1, 2, \dots\;. \end{aligned} \tag{2.32}$$

As shown in Eq. (2.31), the ground state of JCM is a product state while the excited states are entangles states between $|g, n+1\rangle$ and $|e, n\rangle$. In particular the energy splitting between the $|0, g\rangle \to |1, \pm\rangle$ transition, $2g_1$, when $\delta_a = 0$, is called the "vacuum" Rabi splitting [109].

We have to bear in mind that the conservation of excitation number N is often the result of applying the rotating wave approximation (RWA). This is because without the RWA, the interaction between atoms and the linearly polarized photon mode is

$$H_{1,\mathrm{Rabi}}(t) = g_1(a + a^\dagger)(\sigma_+ + \sigma_-), \tag{2.33}$$

which does not commute with the operator N. We approximate $H_{1,Rabi}$ by ignoring the counter rotating term $a\sigma_- + a^\dagger\sigma_+$, which is valid when $g_1 \ll \omega_0$.

If the HO corresponds to the center of mass motion of a charged particle in a harmonic trap or to the Landau Levels of electrons on helium, the HO frequency ω_a is much less than that of the TLS one ω_0. This case the full Hamiltonian in the Schrödinger picture is given by (2.34), which can produce the same interaction term in the rotating frame as the one in (2.29).

In the case of a single trapped ion, which is coupled to a standing wave radiation field, as demonstrated in [15, 110]. This classical radiation field drives a lower sideband optical transition between $|n, e\rangle$ and $|n+1, g\rangle$, where $|n\rangle$ are the eigenstates of the center-of-mass motion in a harmonic trap. The Hamiltonian reads

$$H_{\text{ion}} = \omega_a a^\dagger a + \frac{1}{2}\omega_0\sigma_z + \frac{\Omega}{2}\sin[\eta(a+a^\dagger)]\big(\sigma_+ e^{-i\omega_r t} + H.c.\big), \tag{2.34}$$

where ω_r is the angular frequency of the external radiation field, η is defined as the Lamb-Dicke parameter, and Ω is the Rabi frequency for the atom-light interaction. When $\eta(a+a^\dagger)$ is small, we can approximate $\sin[\eta(a+a^\dagger)] \approx \eta(a+a^\dagger)$ and use a unitary operator

$$U(t) = \exp\big(-\mathrm{i}\omega_a a^\dagger a t\big)\exp[-\mathrm{i}(\omega_r t)\sigma_z/2] \tag{2.35}$$

to transform (2.34) into a time independent Hamiltonian in the interaction picture by neglecting the counter-rotating terms.

$$H_{1,I} = \frac{1}{2}\delta\sigma_z + \frac{1}{2}\Omega\eta(a\sigma_+ + a^\dagger\sigma_-), \tag{2.36}$$

where $\delta = (\omega_0 - \omega_a) - \omega_r$. This is of the same form as (2.29).

JCM with external drive

In the JCM, we can add a linear drive term to describe the external field driving the HO degree of freedom directly. In this situation, the combined excitation number N may no longer be conserved, and therefore the system has more complicated eigenstates and eigenvalues. For example, when the oscillator is coupled to a classical field the Hamiltonian is given by

$$H_d = H_0 + H_{\text{JC}}(t) + H_f(t), \quad H_f(t) = g_2(a+a^\dagger)\cos(\omega_f t). \tag{2.37}$$

This driven JCM is often discussed in the context of cavity or circuit QED, in which the harmonic oscillator term represents the photons in a resonator, [111–113]. In this model the presence of the TSL gives rise to a nonlinearity for the cQED system, which enables feature like bistability and dynamic quantum phase transition. In particular, the eigenstate and eigenergies for when the frequency of the external drive is on-resonance, i.e., $\omega_a = \omega_f$, was solved by [114]. In section 2.4 we will study this model in detail, in the context of using its property to generate squeezed states mentioned above.

2.3.4 Collective spin systems

Besides the squeezing phenomena in bosonic systems (harmonics oscillators), squeezing of spin (or angular momentum) systems is also an interesting and useful topic for quantum applications [89–91, 115]. In the most general sense, the spin systems have finite dimensions which only host $2s+1$ states, as opposed to the harmonic oscillator systems. For experiments, a collective spin can be constructed by an ensemble of TLSs or a combination of two HOs. I will consider the adiabatic generation of non-classical states including spin-squeezed states in Section2.5. The relevant concepts will be reviewed in this subsection, including the intuitive explanation for the Dicke state, the coherent spin state and the squeezed spin state.

Here let us consider an ensemble of N two-level-system or spin-1/2 particles. A total angular momentum operator for the spin ensemble is given by

$$\boldsymbol{J} = \frac{1}{2}\sum_i \boldsymbol{\sigma}_i, \tag{2.38}$$

where $\boldsymbol{\sigma}_i$ is the vector containing three Pauli matrices for the i-th particle.

The spin operators follow the commutation relations for Lie algebra of the special unitary group $SU(2)$

$$[J_i, J_k, =]i\epsilon_{ijk}J_k, \tag{2.39}$$

where the ϵ_{ijk} is the Levi-Civita symbol. To specify, $\epsilon_{xyz} = 1$, $\epsilon_{xzy} = -1$.

We also define the spin raising and lowing operators $J_\pm \equiv J_x \pm \mathrm{i} J_y$, which have the commutation relation reads

$$[J_z, J_\pm] = \pm J\pm, \quad [J_+, J_-] = 2J_z. \tag{2.40}$$

The Hilbert space formed by all the individual spins combined can be divided further into invariant subspaces form by the degenerate eigenstates of J^2, which have eigenvalues $j(j{+}1)$. Since J^2 commutes with $J_{x,y,z}$, we may choose to use the eigenstates of J_z, with eigenvalue m to label states within the degenerate subspace of J^2. These states $|j, m\rangle$ are known as Dicke states [116], and one can use the Dicke states $|j, m\rangle$ as a new basis to describe the collective spins.

The Dicke states are analogous to the Fock states of photons. A Dicke state with $m \neq \pm$j by definition is in a superpostion state composed by all the possible combination of individual spin configurations which produce the same quantum number j and m. This superposition of product states cannot be factorized and there is entanglement between the individual component. Therefore these states are non-classical and can be used as a reliable witness of the existence of entanglement [93, 117].

Besides fundamental research, these non-classical states of collective spins can be used to enhance the precision of measurements in a Mach-Zehnder interferometer and Ramsey spectroscopy, for example as described in the paper by Wineland and coworkers [91]. In short, there are two limits of relative sensitivity in phase or excitation population that one can get by using N two-level system compared to use only one TLS. The minimal scaling of noise for N uncorrelated (classical) TLSs is $1/\sqrt{N}$, which is known as the shot-noise limit. This limit can be obtain optimally by using coherent spin states(CSS) [118]. By using N correlated TLSs, however, in the best case scenario, one can reach the Heisenberg limit $1/N$ [91, 119, 120]. A maximally spin-squeezed state, like a Dicke state with $j = N + 1/2$ and $m = 0$, can be used to generate measurement with precision up to this Heisenberg limit. The quantitative description of this property is written in the following subsections.

Uncertainty, measurement, and squeezing parameter(work in progress)

This subsection is going to define the degree of squeezing and its impact for improving measurements quantitatively.

Following the general case given in Eq. (2.6), the Heisenberg uncertainty relation involving $\boldsymbol{J}$ is

$$\Delta J_x \Delta J_y \geq \frac{1}{2}|\langle J_z \rangle|, \tag{2.41}$$

which is true for other combinations of $J_{x,y,z}$. The uncertainty is related to the quantum states' sensitivity to rotation.

Recall that the coherent state of a HO can be used to describe a classical coherent state of light. The coherent spin states (CSS) describes a classical state of a spin ensemble, in which there is no quantum correlation (entanglement) between the spins [118]. The CSS is a product state of N individual spins all pointing at the same directions specified by spherical coordinate (θ, ϕ).

$$|\theta, \phi\rangle = \bigotimes_{l=1}^{N} (\cos\frac{\theta}{2} |0\rangle_l + e^{i\phi} \sin\frac{\theta}{2} |1\rangle_l), \tag{2.42}$$

in which $|0\rangle$ and $|1\rangle$ are the eigenstates of σ_z with eigenvalues -1 and 1. Note that some literature might use the opposite convention.

By the given definitions, CSS can also be described by rotating the eigenvectors of the Dicke state $|j, m\rangle$. Let $R(\theta, \phi)$ be the rotation operator

$$R(\theta, \phi) \equiv \exp(\zeta J_+ - \zeta^* J_-) = \exp\{\tfrac{1}{2}\theta[\exp(-\mathrm{i}\phi) J_+ - \exp(\mathrm{i}\phi) J_-]\}, \tag{2.43}$$

where $\zeta = -(\theta/2)\exp(-\phi)$.

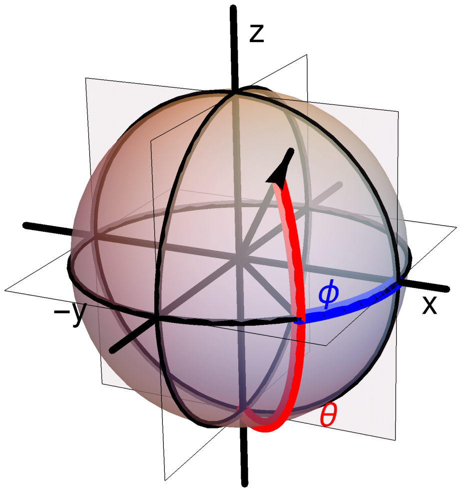

Figure 2.3: Bloch sphere representation of a coherent spin state $R(\theta, \phi)\,|j, -j\rangle$.

Using Eq. (2.11) we can derive the transformation properties of J under a rotation along the z axis [121].

$$\exp(J_z\theta)\, J_\pm \exp(-J_z\theta) = J_\pm e^{\pm\theta} \tag{2.44a}$$

$$\exp(J_z\theta)\, J_x \exp(-J_z\theta) = J_x \cosh\theta + iJ_y \sinh\theta, \tag{2.44b}$$

and get

$$|\theta,\phi\rangle \equiv R(\theta,\phi)\,|j,-j\rangle = (1+|\eta|^2)^{-j} \sum_{m=-j}^{j} \binom{2j}{j+m}^{1/2} \eta^{j+m}\,|j,m\rangle\,, \tag{2.45}$$

where the Dicke state $|j,m\rangle$ are eigenstates of J_z of eigenvalue m, and $\eta = -\tan(\theta/2)\exp(-i\phi)$.

For interferometry purposes, one can prepare the system in an CSS $|\theta = \pi/2, \phi\rangle$, and measure the angle ϕ as an output of the interferometer. This represents the best case scenario for N uncorrelated TLSs in terms of minimizing the uncertainty $\Delta\phi$, which can reach the shot noise limit $1/\sqrt{N}$. However, if one uses an entangled ensemble of N TLSs, in theory, the uncertainty can be lowered to the Heisenberg limit $1/N$. To quantify this improvement one can use the spin squeezing parameter ξ_R define by[91]

$$\xi_R = \sqrt{2J}\,\Delta\,J_y/|\langle J_z\rangle|. \tag{2.46}$$

For a squeezed spin state, there is relation $\Delta\phi = \xi_R/\sqrt{N}$, when $\xi_R < 1$ the phase sensitivity to rotation is improved over CSS.

Similar improvement is also manifested by the spin population statistics $\left|\langle\psi|j,m\rangle_y\right|^2$. A coherent spin state will follow a binomial distribution, which implies the spin is uncorrelated; while the a squeezed spin state can follow a sub-binomial distribution.

Note that, there are other commonly used but different spin-squeezing parameters defined by other authors, for example, [90].

On the other hand, measuring the the uncertainty in these spin state observable can serve as a sufficient witness of entanglement within the ensemble[117],[93].

Connection to harmonic oscillators

Besides physical spin ensemble, on can use the combination of two HOs to construct a large spin. This mapping allow us to describe Mach-Zehnder type of interferometry using angular momentum eigenstates [89, 91, 122]. These two different physical systems are connected because they follow the same $SU(2)$ or $SU(1,1)$ symmetry. To construct large spin using harmonic oscillators, one may introduce Schwinger's oscillator model of angular momentum [123]. We define abstract operators:

$$J_+ \equiv a_1^\dagger a_2, \quad J_{\equiv} a_2^\dagger a_1, \tag{2.47}$$

and

$$J_z \equiv (a_1^\dagger a_1 - a_2^\dagger a_2)/2. \tag{2.48}$$

Defining the total j to be

$$j \equiv (a_1^\dagger a_1 + a_2^\dagger a_2)/2, \tag{2.49}$$

leads to

$$J^2 = J_z^2 + \frac{1}{2}(J_+J_- + J_-J_+) = j(j+1). \tag{2.50}$$

This way we associate j with the total excitation number of the two HOs, and associate J_z with the difference between the excitation number of the two HOs.

2.3.5 Adiabatic time evolution

If the time-dependent Hamiltonian $H(t)$ of a quantum system varies slowly, at a time scale T such that h/T is small compared to the gaps between eigenenergies. The system will be following the eigenstates of the instantaneous Hamiltonian, as stated in the well-known adiabatic theorem[124].

To show the properties of time-dependent Hamiltonian, let $|n;y\rangle$ be the instantaneous eigenstates of $H(t)$.

$$H(t)\,|n;t\rangle = E_n(t)\,|n;t\rangle \tag{2.51}$$

Let $|\alpha;t\rangle \equiv \sum_n c_n \exp(\mathrm{i}\theta_n)\,|n;t\rangle$ be a general state evolving under $H(t)$, where $\theta_n \equiv -(\int_0^t \mathrm{d}t'\, E_n(t'))/\hbar$ is the dynamic phase.

If $|n;t\rangle$ is not degenerate, rearranging the Shrödinger equation $\mathrm{i}\hbar\partial_t\,|\alpha;t\rangle = H(t)\,|\alpha;t\rangle$ gives the differential equation for the "mixing" of eigenstates due to the time evolution.

$$\dot{c}_m = -c_m\,\langle m|\left[\partial_t\,|m\rangle\right] - \sum_{n\neq m} c_n \exp\left[\mathrm{i}(\theta_n - \theta_m)\right]\frac{\langle m|\,\dot{H}\,|n\rangle}{E_n - E_m}. \tag{2.52}$$

Adiabatic approximation

In the limit of slow evolution the chaange in the Hamiltonian $\dot{H}$ is small enough that

$$\frac{\langle m|\dot{H}|n\rangle}{E_{nm}} \ll \langle m|\partial_t m\rangle\,, \tag{2.53}$$

so the second term in (2.52) can be ignored. Consequently, $c_m(t)$ acquires an extra phase factor associates with $\langle m|\partial_t m\rangle$ while the population $|c_m(t)|^2$ is unchanged. [125]

$$c_n(t) = \exp(\mathrm{i}\gamma_n(t))c_n(0), \tag{2.54}$$

where $\gamma_n(t)$ is a real number defined by

$$\gamma_n(t) \equiv i\int_0^t \mathrm{d}t'\,\langle n|\partial_{t'} n\rangle \tag{2.55}$$

When degeneracy is present, the system evolves adiabatically within the degenerate subspace. This generates a non-Abelian analog of Berry's geometric phase[126].

2.4 Jaynes-Cummings Hamiltonian with the oscillator subject to a resonant, linear drive

We consider a two-level system (TLS) with a ground state $|g\rangle$ and an excited state $|e\rangle$, which is described by the raising and lowering operators, $\sigma_+ = |e\rangle\langle g|$ and $\sigma_- = |g\rangle\langle e|$. It also interacts resonantly with strength g_1 with a quantized oscillator, described by the operators a and $a^\dagger$, which in turn is subject to a resonant classical driving force of strength g_2. The schematic level diagram shown in Figure 2.4 depicts the product

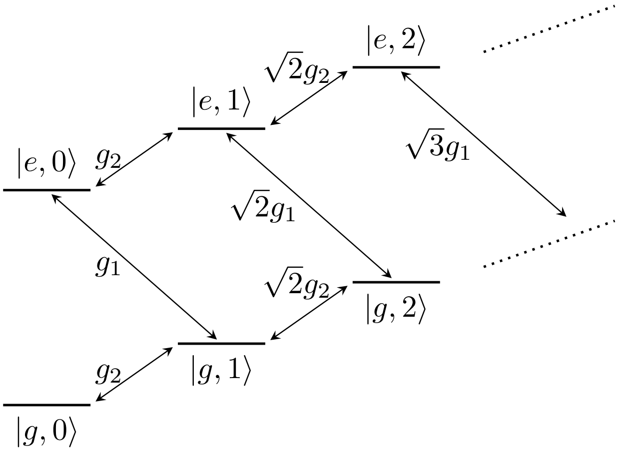

Figure 2.4: Energy level diagram.

eigenstates $|\chi,n\rangle = |\chi\rangle \otimes |n\rangle$ of the uncoupled systems, where $\chi = g, e$ denotes the state of the TLS and n is the excitation number of the oscillator mode.

As introduced in subsection 2.3.3, in the rotating frame in the interaction picture (with respect to the bare atom and oscillator Hamiltonians) and with the rotating wave approximation, the Hamiltonian takes the form [67]

$$H_{\mathrm{I}} = g_1 \left(\sigma^- a^\dagger + \sigma^+ a\right) + g_2 \left(a^\dagger + a\right). \tag{2.56}$$

A system of this kind can be implemented in a variety of quantum systems with two-level and oscillator degrees of freedom. In the case of a single trapped ion, g_1 can be obtained by driving a lower sideband optical transition, while g_2 can be implemented by an electric RF interaction with the charged particle motion. Atoms in cavities are excited by absorption of a cavity photon with strength g_1, while resonant illumination of the cavity coherently excites the cavity mode with strength g_2 [14, 15]. Throughout the whole section, unless stated otherwise, we only consider the eigenstates in the rotating frame. The full Hamiltonian is described in subsection 2.3.3.

In the absence of pumping of the oscillator ($g_2 = 0$), the system is governed by the usual JC Hamiltonian and has the well known dressed eigenstates, $\frac{1}{\sqrt{2}}(|g,n\rangle \pm |e,n-1\rangle)$, with symmetric pairs of energies $\pm g_1\sqrt{n}$ around the zero energy of the ground state $|g,0\rangle$. The presence of the g_2 term in the Hamiltonian (2.56) does not change the symmetry of the spectrum: for any eigenstate $|\Psi\rangle$ of H_{I} with eigenvalue E, it is easy to verify that $(-1)^{a^\dagger a}|\psi\rangle$ is an eigenstate with eigenvalue $-E$.

All eigenvalues of the Hamiltonian (2.56) for $g_2 < g_1/2$,

$$E_0 = 0, \quad E_n^\pm = \pm\sqrt{n} g_1 \left(1 - \left(\frac{2g_2}{g_1}\right)^2\right)^{\frac{3}{4}} \tag{2.57}$$

have been identified by Alsing and Carmichael together with expressions for the corresponding eigenstates [114].

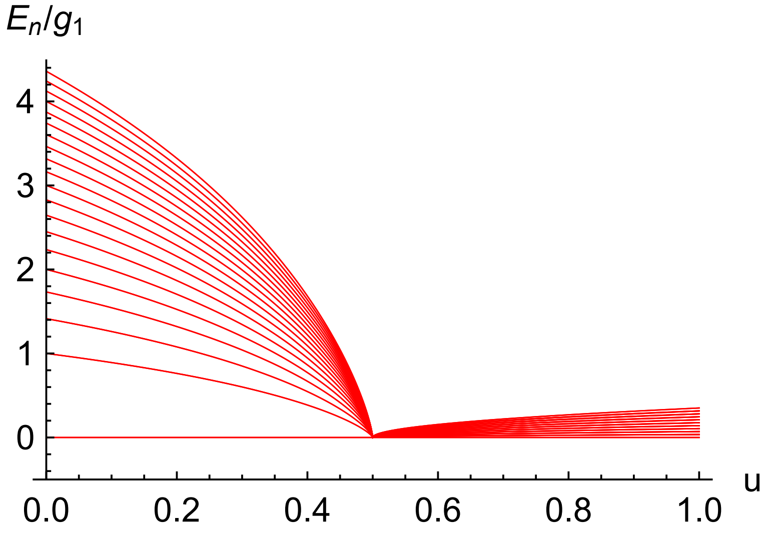

Figure 2.5: A few smallest non-negative scaled eigenvalues: E_n/g_1, of the Hamiltonian (2.56), in the truncated Fock basis of the oscillator ($N_{\mathrm{cut}} = 2000$). The spectrum is symmetric with eigenvalues $\pm E$ around zero. The horizontal axis is a transition parameter $u \equiv 2g_2/(g_1 + 2g_2)$.

2.4.1 The eigenstates

Diagonalizing the Hamiltonian over the full parameter range, we show the 21 lowest lying non-negative eigenvalues in Fig. 2.5 as function of the parameter $u = 2g_2/(g_1 + 2g_2)$. The numerical results confirm the existence of the zero eigenvalue over the whole parameter range and the collapse of all eigenvalues to zero when $g_2 \to g_1/2$ ($u \to 1/2$). In the limit where $u = 1$, the system is only subject to the linear Hamiltonian $H_{\mathrm{I}} = g_2(a + a^\dagger) = g_2 \cdot x$, and the resulting, un-normalizable position eigenstates have a continuum of eigenvalues. Due to the truncation in Fock space at $N_{cut} = 2000$ in the numerical diagonalization, with a resulting largest $x_{\mathrm{rms}} \simeq \sqrt{N_{\mathrm{cut}}}$, however, the eigenvalues show almost equidistant spacing $\propto 1/\sqrt{N_{\mathrm{cut}}}$ in the right hand side of the figure.

We now turn to the adiabatic evolution of the zero energy state as the driving strength g_2 is gradually increased. We expect to follow the zero energy eigenstate adiabatically as long as the change of Hamiltonian is slow compared to the energy gap to the other states, i.e., until we approach $g_2 = g_1/2$. Although the full set of eigenstates is identified in [114], it is instructive to deal separately with the zero energy eigenstate, and we apply the product state ansatz $|\Psi\rangle = |\chi\rangle \otimes |\phi\rangle$ with the two-level systems parametrized as $|\chi\rangle = (\cos\theta/2, \sin\theta/2)^T$. This yields an equation for each spin component of the eigenvalue equation, that must both be fulfilled by the oscillator state $|\phi\rangle$,

$$\begin{aligned}\left[g_1 \sin\frac{\theta}{2} a^\dagger + g_2 \cos\frac{\theta}{2}\big(a + a^\dagger\big)\right] |\phi\rangle = 0 \\ \left[g_1 \cos\frac{\theta}{2} a + g_2 \sin\frac{\theta}{2}\big(a + a^\dagger\big)\right] |\phi\rangle = 0.\end{aligned} \tag{2.58}$$

This system has unique solutions for $|\phi\rangle$ only if they are linearly dependent, which allows to find the relation

$$\sin\theta = -2g_2/g_1, \tag{2.59}$$

with real solutions for $-\pi/2 < \theta < \pi/2$ as long as $|g_2/g_1| < 1/2$. It is worth noting that the equations (2.58) for the oscillator state can be written in the familiar form

$$\left(\mu a + \nu a^\dagger\right)|\phi\rangle = 0, \tag{2.60}$$

where the real parameters

$$\begin{aligned}\nu &= -\sin^2(\theta/2)\sqrt{\sec(\theta)},\\ \mu &= \cos^2(\theta/2)\sqrt{\sec(\theta)},\end{aligned} \tag{2.61}$$

obey the normalization condition $\mu^2 - \nu^2 = 1$. The solutions to eq. (2.60) yield minimum uncertainty squeezed states [76, 77] with variances in the $x = a + a^\dagger$ and $p = i(a^\dagger - a)$ oscillator quadratures given by

$$\begin{aligned}\mathrm{Var}(x) &= \left\langle (a + a^\dagger)^2\right\rangle = (\mu - \nu)^2 = \sec\theta,\\ \mathrm{Var}(p) &= \left\langle (i(a^\dagger - a))^2\right\rangle = (\mu + \nu)^2 = \cos\theta.\end{aligned} \tag{2.62}$$

By applying a classical field or a coherent drive to a cavity or a mechanical oscillator, coupled to a two-level system, the oscillator is driven adiabatically into a squeezed state, and we believe that this may be a robust, practical protocol to achieve appreciable squeezing. It is remarkable that while the adiabatically varying Hamiltonian passes between the Jaynes-Cummings Hamiltonian and the x quadrature operator, and one might hence have expected the zero energy eigenstate to gradually transform into the $x = 0$ position eigenstate, we instead observe strong squeezing of the conjugate observable p, as the system approaches the critical driving strength, $g_2 = g_1/2$.

2.4.2 The time evolved quantum state

We have solved the time dependent Schrödinger equation under slow variation of the coupling strength g_2 and as one may expect, we find that beyond a finite degree of squeezing the system cannot follow the $E = 0$ eigenstate adiabatically and the factorization in separate TLS and oscillator components fails. The fact that the Hamiltonian does not even have normalizable eigenstates as we explore values of $g_2 > g_1/2$ does not, however, prevent numerical solution of the Schrödinger equation, and we have explored the dynamics within a truncated basis of harmonic oscillator states.

We assume the timedependent interaction strengths,

$$g_1(t) = (1 - \frac{t}{T})g, \quad g_2(t) = \frac{1}{2}\frac{t}{T}g, \tag{2.63}$$

such that $u = 2g_2/(g_1 + 2g_2)$ changes from 0 to 1 linearly in time. The results are obtained for a time scale $T = 100g^{-1}$ and a truncation of the oscillator Fock space at $N_{\mathrm{cut}} = 2000$. For early times the elliptic shaped Wigner function shows the graduate squeezing of the vertical p component, cf., the upper panels of Fig. 2.6 As we surpass

$g_2 = g_1/2$ the elliptic shape is distorted, and the non-adiabatic evolution gives rise to a ‘cat-like’ superposition of components with well defined amplitude which are both displaced towards negative p values and with negative quasi-probability ’fringes’ along the $x = 0$ line, cf. the lower panels of Fig. 2.6.

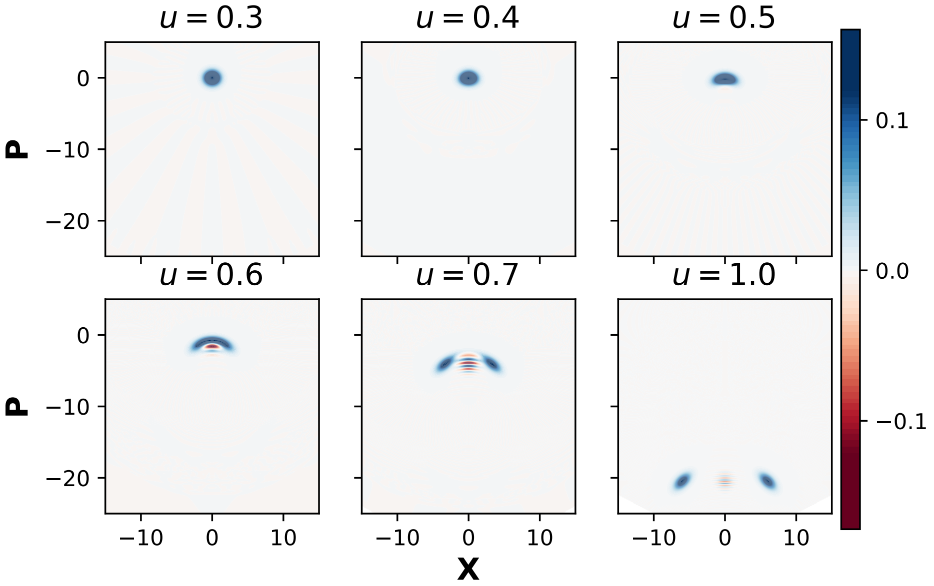

Figure 2.6: Wigner function of the time evolved system. Initially the system is able to follow the momentum squeezed eigenstates of the Hamiltonian adiabatically, but later non-adiabatic effects distort the phase space distribution and a ’Schrödinger cat-like’ state appears when the Hamiltonian no longer supports discrete eigenstates

.

2.5 Two-level system coupled to an integer collective spin subject to a resonant, linear drive

Let us consider the case of a two-level particle coupled to a collective spin J

$$H_I = g_1\big(\sigma^- J_+ + \sigma^+ J_-\big) + g_2(J_+ + J_-), \tag{2.64}$$

where we define $J_- \equiv J_x - iJ_y$, $J_+ \equiv J_x + iJ_y$.

Such a system may be implemented by the electron and nuclear spin in alkali atoms, and the large spin may also represent symmetric, collective states of a collection of two-level systems or the Schwinger representation of a pair of oscillators. For any eigenstate $|\Psi\rangle$ of H_I with eigenvalue E, $e^{-i\pi J_z}|\Psi\rangle$ is an eigenstate of H_I with eigenvalue $-E$, so the spectrum is symmetric around zero as in the oscillator case. For large J, the states close to the extremal J_z eigenstate $|J, M = -J\rangle$, indeed, constitute an oscillator-like ladder and the weakly driven system shows similarities with the driven JC model. When driven more strongly, we expect to see deviations from the JC dynamics, and due to

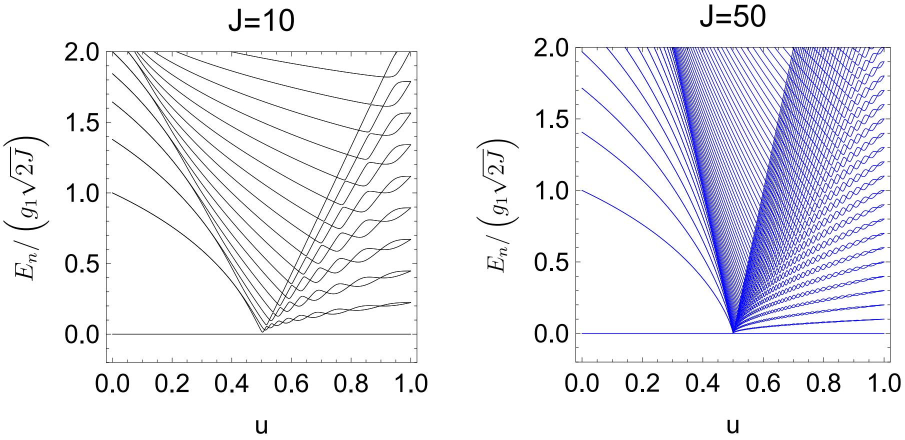

Figure 2.7: Lowest, non-negative energy eigenvalues for the two-level system coupled to a collective spin with $J = 10$ (left) and $J = 50$ (right). The scaling factor $(g_1\sqrt{2J})^{-1}$ ensures the similarity with Fig. (2.5) for the lowest eigenvalues for values of $u < 0.5$, where $u \equiv 2g_2/(g_1 + 2g_2)$.

the finite Hilbert space we obtain discrete, normalizable eigenstates of the Hamiltonian (2.64) for all coupling parameters.

These properties are confirmed by numerical diagonalization of the Hamiltonian as illustrated for $J = 10$ and $J = 50$ in Fig. 2.7. When the eigenvalues are scaled by $\sqrt{2J}$, the lowest lying states for $g_2 < g_1/2$ show similar behavior as in Fig. 2.5, while, for $g_2 > g_1/2$, the density of eigenstates depends on the finite number of angular momentum states $2J+1$ rather than the numerical truncation of the oscillator system.

Systems with integer spin J described by Eq. (2.64) have an odd number of distinctive eigenvalues, and due to the symmetry between positive and negative eigenvalues, there always exists eigenstates with eigenvalue 0. When we drive the system parameters across the transitional point we explore the transition between the zero energy eigenstates in the parameter ranges $g_2 < g_1/2$ and $g_2 > g_1/2$.

2.5.1 The eigenstates

We will study the adiabatic evolution of the system when g_2 is gradually turned on, starting from the zero energy eigenstate $|g\rangle \otimes |J, -J\rangle$. The state will initially show features similar to the ones obtained in the previous section, but here we shall be able to understand the full dynamics through all parameter values from the behavior of the adiabatic eigenstates.

The similar structure of Eqs.(2.56) and (2.64) with the operator a replaced by J_- permits use of the same factorization ansatz $|\Psi\rangle = |\chi\rangle \otimes |\phi\rangle$ to obtain the zero energy eigenstates, satisfying $H_I |\Psi\rangle = 0$.

In the parameter range $0 < g_2/g_1 < 1/2$, we can use the same expression for the TLS:

$$|\chi\rangle = (\cos(\theta/2), \sin(\theta/2))^{\mathrm{T}}, \tag{2.65}$$

where $\theta = \arcsin(-2g_2/g_1)$, such that Eq. (2.64) yields a single equation for $|\phi\rangle$,

$$(\mu J_- + \nu J_+) |\phi\rangle = 0, \tag{2.66}$$

with $\nu/\mu = -\tan^2(\theta/2)$. The solution of Eq.(2.66) is a minimum uncertainty spin squeezed state, also known as a generalized intelligent state [121, 127], and it is known to be of the explicit form,

$$|\phi\rangle = C(\tau)e^{-\tau J_z} e^{i\frac{\pi}{2}J_x} |J,0\rangle_z = C(\tau)e^{-\tau J_z} |J,0\rangle_y , \tag{2.67}$$

where $\tau = \log\sqrt{\left|\frac{\mu}{\nu}\right|} = \log\left(\left|\cot\frac{\theta}{2}\right|\right)$ and $C(\tau)$ is a normalization factor to ensure $\langle\phi|\phi\rangle = 1$. We use $|J,0\rangle_{z(y)}$ to denote the$J_{z(y)} = 0$ eigenstates of the large spin.

The spin component uncertainties in the state $|\phi\rangle$ are

$$\begin{aligned} \langle\Delta J_y\rangle &= \sqrt{\cos\theta}\sqrt{|\langle J_z\rangle|}/2 \\ \langle\Delta J_x\rangle &= \sqrt{\sec\theta}\sqrt{|\langle J_z\rangle|}/2. \end{aligned} \tag{2.68}$$

where $\langle J_z\rangle = C_\tau^2 \langle J,0|_y J_z e^{-2\tau J_z} |J,0\rangle_y$ in our case.

For $g_2/g_1 > 1/2$, we may apply the complex argument solutions to $\theta = \arcsin(-2g_2/g_1)$, but for clarity we shall introduce an alternative parametrization with real arguments,

$$|\chi\rangle = \frac{1}{\sqrt{2}}\left(e^{i\varphi/2} \quad , -e^{-i\varphi/2}\right)^{\mathrm{T}}, \tag{2.69}$$

where $\tan^2\varphi = 4g_2^2/g_1^2 - 1,\ 0 < \varphi < \pi/2$, resulting in the large spin equation

$$(e^{i(-\varphi-\pi/2)}J_- + e^{i(\varphi+\pi/2)}J_+) |\phi\rangle = 0. \tag{2.70}$$

The pre-factors on J_- and J_+ have the same absolute value, and for $g_2 = g_1/2$, $\varphi = 0$, and $|\phi\rangle$ is the $J_y = 0$ eigenstate, while for larger g_2 and a finite φ, Eq.(15) describes an infinitely spin squeezed state with $M = 0$ about an axis in the direction φ with respect to the y-axis in the equatorial plane. As $g_2/g_1 \to \infty$, φ approaches $\pi/2$ and $|\phi\rangle$ rotates towards the (expected) $J_x = 0$ eigenstate of the large spin. We note that these states have the explicit expression

$$|\phi\rangle = e^{i\varphi J_z} e^{i\frac{\pi}{2}J_x} |J,0\rangle_z = e^{i\varphi J_z} |J,0\rangle_y . \tag{2.71}$$

and that they may be attractive for precision measurements [93, 117].

2.5.2 Degeneracy of the $E = 0$ eigenstates

So far, we have disregarded an important fact in the description of the system: the energy eigenvalues for the Hamiltonian are two-fold degenerate for all values of the coupling strengths. This has the consequence that any weak coupling is sufficient to drive rotations of the state in the two-dimensional $E = 0$ subspace and must be taken into account to properly describe the time evolution of the system, even if g_1 and g_2

change infinitely slowly.

The degeneracy of the Hamiltonian eigenstates follows from the fact that the Hamiltonian (2.64) commutes with the operator $R_x = \exp(-i\pi(J_x + \sigma_x/2))$, which applies a 180 degree rotation around the x axis to both the two-level spin vector and the large angular momentum. This implies that for any eigenstate $|\Psi\rangle$ of H_I, $R_x|\Psi\rangle$ is also an eigenstate of H_I with the same energy.

For integer values of J, $R_x^2 = e^{i(2\pi(1/2+J))} = -\mathbb{1}$, and $i(-1)^J R_x$ thus has the eigenvalues ± 1. It follows that assuming the zero energy product states $|\Psi\rangle = |\chi\rangle \otimes |\phi\rangle$ defined in the previous subsection, we can construct an orthonormal pair of joint eigenstates for H_I and $i(-1)^J R_x$ (eigenvalues ∓ 1),

$$|\Psi_\pm\rangle = \frac{|\Psi\rangle \pm i(-1)^J R_x |\Psi\rangle}{\sqrt{2}\sqrt{1 \pm \gamma}}, \tag{2.72}$$

where γ is the real part of the state vector overlap $\gamma = \mathrm{Re}(\langle\Psi| (iR_x(-1)^J |\Psi\rangle))$. We shall denote these eigenstates $|\Psi_\pm^{(1)}\rangle$ and $|\Psi_\pm^{(2)}\rangle$ in the domains $0 < g_2/g_1 < 1/2$ and $g_2/g_1 > 1/2$, respectively.

As the initial state $|\Psi\rangle$ for $g_2 = 0$ is orthogonal to $R_x|\Psi\rangle$ and hence $\gamma = 0$, we can expand it as

$$|\Psi\rangle = \frac{1}{\sqrt{2}}(|\Psi_+^{(1)}\rangle + |\Psi_-^{(1)}\rangle), \quad \text{for } g_2 = 0. \tag{2.73}$$

A general theory for adiabatic evolution with degenerate subspaces was presented in [126], but in our problem symmetry arguments suffice to obtain the approximate time dependent states (ignoring transitions to adiabatic eigenstates with non-vanishing energy). Linearity of quantum mechanics, and the fact that the time dependent H_I commutes with R_x and hence does not couple the $|\Psi_\pm\rangle$ eigenstates, ensures that the system will adiabatically evolve as the equal weight superposition of the symmetrized energy eigenstates, $|\Psi\rangle = \frac{1}{\sqrt{2}}(|\Psi_+^{(1)}\rangle + |\Psi_-^{(1)}\rangle)$, as g_2 is slowly increased towards the value $g_2 = g_1/2$.

At $g_2 = g_1/2$ a basis transformation to the eigenstates $|\Psi_\pm^{(2)}\rangle$ takes place. With our convention (2.65,2.67) and (2.69,2.71) for the eigenstate $|\Psi\rangle$, we find that when approaching $g_2 = g_1/2$ from opposite sides, the limiting eigenstates obey the identities

$$\begin{aligned} |\Psi_+^{(1)}\rangle &= |\Psi_+^{(2)}\rangle \\ |\Psi_-^{(1)}\rangle &= -i\,|\Psi_-^{(2)}\rangle\,, \end{aligned} \tag{2.74}$$

where the first expression follows easily, while the second one requires a more careful analysis of the first order dependence of the states on the angle variable on either side of $g_2 = g_1/2$.

Assuming that transitions to states with different energies are suppressed, we obtain the adiabatic approximation to the time dependent solution of the problem:

$$|\Psi\rangle = \begin{cases} \frac{1}{\sqrt{2}}\left(|\Psi_+^{(1)}\rangle + |\Psi_-^{(1)}\rangle\right), & g_2 < g_1/2; \\ \frac{1}{\sqrt{2}}\left(|\Psi_+^{(2)}\rangle - i\,|\Psi_-^{(2)}\rangle\right), & g_2 > g_1/2. \end{cases} \tag{2.75}$$

2.5.3 The time evolved quantum state

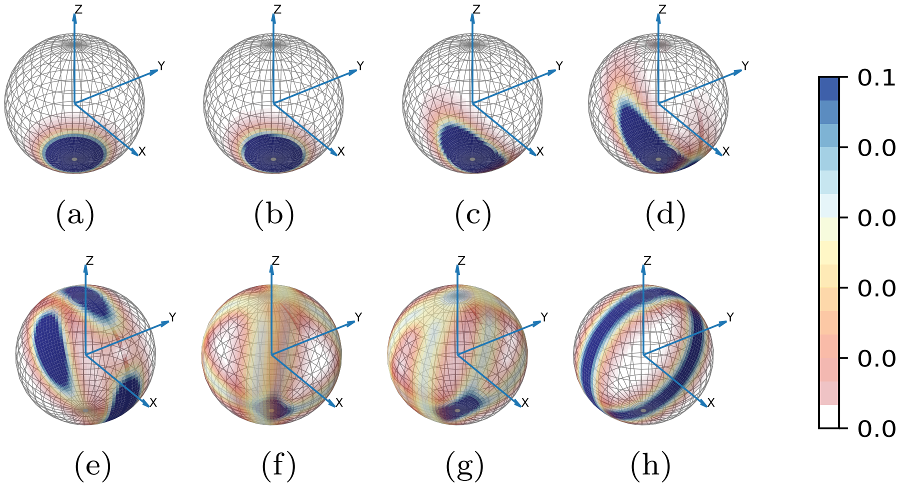
(a) (b) (c) (d)
(e) (f) (g) (h)

Figure 2.8: The result of time evolution of the TLS and a large spin with J=20, subject to the Hamiltonian (2.64), with time varying coefficients $g_1(t)$ and $g_2(t)$ as in the previous section. The result is represented by the Husimi Q-function of the reduced density matrix of the large spin ρ_ϕ, shown for different values of $u \equiv 2g_2/(g_1 + 2g_2)$. While increasing g_2 and decreasing g_1, the collective spin subsystem starting form $|J, -J\rangle$ ($u = 0$), evolves along spin squeezed states and spin eigenstates determined by the analytical arguments and expressions in the main text. (a) u=0.1; (b) u=0.4; (c) u=0.49; (d) u=0.499; (e) u=0.501; (f) u=0.6; (g) u=0.7 (h) u=1.0.

We have numerically tested the validity of the restriction of the dynamics to the $E = 0$ subspace and the formation of superposition states in this subspace. Using the temporal ansatz (8), with a duration $T > 10000g^{-1}$ we find good agreement throughout the entire time evolution between the numerical solution of the time dependent Schrödinger equation and our analytical eigenstate expressions. Fig. 2.8 shows results obtained with $T = 50000g^{-1}$, and we observe how the state occupied for $g_2 < g_1/2$ first develops into a highly spin squeezed state in the xz-plane and then a $J_y = 0$ eigenstate as shown by the Husimi Q-function in the upper panels in Fig. 2.8. For $g_2 > g_1/2$ the numerical solution reveals an intricate patterns of two vertical rings that rotate in opposite direction, cf., the lower panels in Fig. 2.8. These rings are the $M = 0$ eigenstate components Eq.(2.71) with opposite angular argument φ, populated simultaneously in Eq.(2.75) and finally coalescing into the $J_x = 0$ eigenstate. The simultaneous occupation of two differently oriented spin squeezed states is similar to the observation in Fig. 2.6 of the progression from a momentum squeezed state of the time evolved harmonic oscillator into two position squeezed wave packet components. In the limit of $g_2 \gg g_1$, when the two angular momentum states coincide in the $J_x = 0$ eigenstate, the TLS occupies a superposition of $|\chi_1\rangle$ and $|\chi_2\rangle$, forming the TLS ground state $|g\rangle$.

To further illustrate how the system evolves from a product state to an entangled superposition state and back to a product state, we shown the time evolution of the reduced density matrix of the TLS subsystem, $\rho_\chi(t)$, in the left panel of Fig. 2.9,

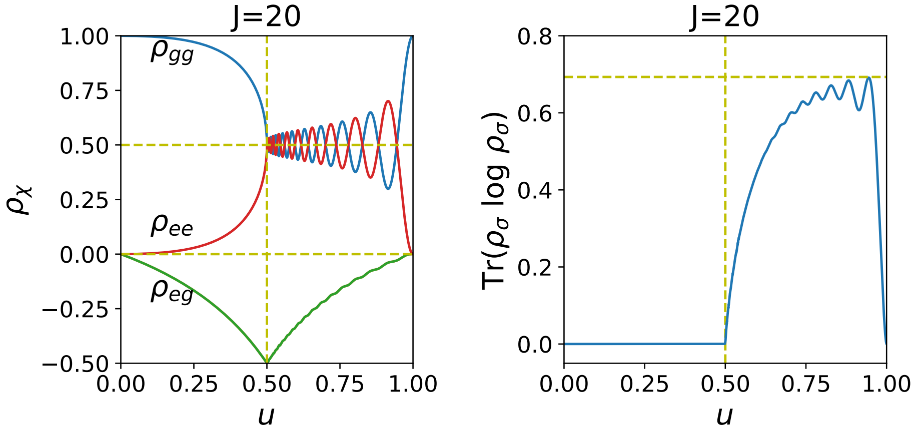

Figure 2.9: The result of slow time evolution by the Hamiltonian (2.64) illustrated by the reduced density matrix elements of the two-level subsystem $\rho_\chi(t)$ and its von Neumann entropy. The horizontal axis is the transition parameter $u \equiv 2g_2/(g_1 + 2g_2)$.

corresponding to the Husimi Q-Function shown in Fig. 2.8. The rapid oscillation between density matrix element ρ_{gg} and ρ_{ee}, is caused by interference terms in the scalar product $\langle\phi|e^{-i\pi J_x}|\phi\rangle$ of the two $M = 0$ states with respect to the rotated axes and is only reproduced correctly by the analytical $E = 0$ superposition states Eq.(20) if the proces duration is longer than $10000g^{-1}$. The right panel in Fig. 2.9 shows the von Neumann entropy of the state of the TLS, confirming the emergence and disappearance of entanglement of the joint quantum state of the system.

2.6 Discussion

To summarize, we have analyzed the dynamics of a two-level system coupled resonantly to an oscillator and to a large spin. We have shown that factorized zero energy states exist under the resonant driving of the oscillator or large spin, and that the adiabatically evolved state becomes squeezed and entangled as the driving amplitude is gradually increased. These results supplement related ideas for generation of squeezed and non-classical states in the literature [94, 95] and due to the generic Hamiltonians assumed in this work they may inspire experimental protocols for squeezing of field and motional oscillators and collective spins in a variety of quantum systems.

Our method of solution may go well beyond the Hamiltonians studied in this article and apply to the coupling of a TLS and any ancillary system with a Hermitian adjoint pair of operators $K^\dagger$ and K,

$$H_I \equiv g_1 \left(\sigma^- K^\dagger + \sigma^+ K\right) + g_2 \left(K^\dagger + K\right). \tag{2.76}$$

The similarity with Eqs. (2.56,2.64) invites use of the product state ansatz: $|\Psi\rangle = |\chi\rangle\rangle \otimes |\phi\rangle$ for an $E = 0$ eigenstate, where $|\chi\rangle = (\cos\theta/2, \sin\theta/2)^T$, leads to two equations

$$\begin{aligned}\left[\sin\frac{\theta}{2}K^\dagger + \frac{g_2}{g_1}\cos\frac{\theta}{2}\big(K+K^\dagger\big)\right]|\phi\rangle &= 0\\ \left[\cos\frac{\theta}{2}K + \frac{g_2}{g_1}\sin\frac{\theta}{2}\big(K+K^\dagger\big)\right]|\phi\rangle &= 0,\end{aligned} \tag{2.77}$$

and with the constraint $\sin\theta = -2g_2/g_1$, we find that $|\phi\rangle$ must solve the equation,

$$\big(\mu K + \nu K^\dagger\big)|\phi\rangle = 0, \tag{2.78}$$

where $\nu/\mu = -\tan^2(\theta/2)$.

2.6.1 Outlook

In trapped ions lower sideband excitation can be used to implement the JC model and upper sideband excitation leads to the so-called anti-JC model with interaction $\propto (\sigma^- a + \sigma^+ a^\dagger)$ [128]. Simultaneous driving of both sidebands then implements ladder operators among squeezed Fock states (Bogoliubov transformed linear combinations of a and $a^\dagger$) [129] with Hamiltonians that are also explicitly of the form of (2.76). To obtain similar results as in the present work, we recall that one must verify the existence of the $E = 0$ product state which will depend on the properties of the ancillary system (e.g., it does not occur for Eq.(9) with a half integer spin) and of the operator K.

The adiabatic time-evolution is a useful and robust method to prepared engineered quantum states, because it allows us to ignore the details of $H(t)$, and thus tolerates imperfections in a real experiment. For future works, the adiabatic method can be easily extended to a faster process by shortcut to adiabaticity or optimal-control. For example, the unwanted transition created by a finite speed $H(t)$ can be canceled by applying a counter adiabatic term, which is known as transitionless quantum driving[130].

Further applications may go well beyond quantum optics as, e.g., Gutiérrez-Jáauregui and Carmichael [131] have emphasized the interesting formal equivalence between the driven Jaynes-Cummings Hamiltonian and the Dirac Hamiltonian of a charged particle subject to an external electromagnetic field and where a similar transition between discrete and continuous spectra appear.

Chapter 3

Coupling between Rydberg states and Landau Levels of surface electrons

The coupling between the Rydberg states of electrons trapped on the surface of liquid helium and the equidistant Landau Levels of the electron cyclotron motion induced by a perpendicular magnetic field is usually small. However, this coupling can be significantly enhanced by applying a non-zero component of magnetic field parallel to the surface. In this chapter we provide necessary theoretical background and describe an experimental realization of such a coupling. It is shown that it leads to the renormalization of the energy spectrum of the electron orbital motion and a plethora of interesting phenomena known in the Atomic and Molecular Optics (AMO), such as the dressed states and avoided crossings of energy levels in the Rydberg spectrum, the light shifts and sideband transitions in coupled system, etc. The strong non-linearities of the cyclotron motion of electrons introduced by such coupling can be used for cQED-type experiments in such electron systems coupled to the optical resonators described in Chapter 1.

3.1 Motivation

As was demonstrated in Chapter 1, two-dimensional electrons on liquid helium coupled to a single-mode optical resonator and subject to a static perpendicular magnetic field can be a suitable systems for cQED-type of experiments providing there are appreciable non-linearities in the system. Also, in Chapter 2 we described some hypothetical model systems where coupling between a strongly nonlinear TLS and an oscillator mode can be used to create and study non-classical states of matter and light. The Rydberg states of electrons on helium with their non-equidistant energy spectrum can potentially provide a source of strong non-linearity in our system. Although the coupling between the Rydberg states and the Landau levels of the quantized cyclotron motion can be mediated by the scattering of electrons from ripplons, it is very weak. However, the significant coupling can be introduced by applying a static in-plane magnetic field in addition to the perpendicular field. The effect of tilted magnetic field on the electron energy spectrum was first investigated by Fang and Stiles for 2DEG in silicon inversion layers [132], and subsequently probed by electrical transport measurements in several experiments in semiconductors [133]. Recently it was demonstrated that a tilted magnetic field applied to the surface electrons (SE) on liquid helium leads to the renormalization of the electron's Rydberg spectrum due to the coupling to the cyclotron oscillator mode, which can be seen as an analog of the Lamb shift [134]. This can provide a new interesting avenue for our future experiments with electrons on helium coupled to microwave cavity resonators.

Here we theoretically and experimentally study the effect of the in-plane magnetic field on the Rydberg states of electrons on liquid helium. We provide a thorough analysis of the coupled states, which are described by a Jaynes-Cummings-type Hamiltonian, using both the second-order perturbation theory and numerical diagonalization calculations. Several theoretical predictions which came from our analysis are then compared with the experimental data which were obtained using the spectroscopic detection of the Rydberg states of electrons on liquid ^{3}He in tilted magnetic fields. Our studies confirm that the tunable coupling induced by the in-plane magnetic field introduces strong non-linearity in the cyclotron oscillator spectrum, which potentially can be used in our future cQED-type of experiments with the electrons-on-helium system.

3.2 Electrons on helium in tilted magnetic fields

This section provides a thorough theoretical analysis of the eigenstates of electrons on helium subject to a tilted magnetic field. The predictions of our treatment will be compared with the experimental results in Section 3.4. For the sake of simplicity, throughout this chapter we will omit the hat notations for quantum mechanical operators.

3.2.1 Stark shift of energy levels in a perpendicular electric field

‘

The energy eigenvalues of the Rydberg states of quantized motion perpendicular to the liquid surface were described for electrons on helium in the Introduction. Here we describe the effect of an electric field $E_\perp$ applied perpendicular to the surface. Such a field is usually present in the experiments due to a positive bias applied to the back-gate electrode placed beneath the liquid surface, e.g. see Chapter 1. In addition, the linear dc Stark shift due to such a field provides a convenient way to tune energy difference between Rydberg states for their spectroscopic studies, as will be described in Section 3.3.

In a uniform electric field $E_\perp$, the electron's Hamiltonian for z-motion reads

$$H_{\mathrm{z}} = \frac{p_z^2}{2m_e} + V(z) + eE_\perp z, \quad e > 0, \tag{3.1}$$

where $V(z)$ includes the effect of the positive image charge in the liquid and the repulsive barrier at the helium surface, see the Introduction. For sufficiently small values of $E_\perp$, the energy shift for n-th Rydberg state without the electric field is given by $\Delta E_n^{(1)} = eE_\perp z_{nn}$, where z_{nn} is the mean value of the coordinate operator z for this state. It is clear that the dc Stark shift is linear due to the inversion symmetry breaking in z-direction imposed by the repulsive barrier at the liquid surface. Already for moderate fields $E_\perp \sim 10$ V/cm the perturbation theory does not provide accurate estimates for the shifts, therefore one has to numerically solve the 1D eigenvalue problem with the Hamiltonian (3.1). The energy eigenvalues and probability densities for the corresponding eigenstates calculated for $E_\perp = 15$ V/cm for an electron above liquid ^{3}He are shown in Fig. 3.1(b) and can be compared with corresponding quantities for $E_\perp = 0$, see Fig. 3.1(a). From this comparison it is clear that even the moderately small electric fields lead to the large shifts of energy levels and strong reduction of the electron localization length in z-direction.

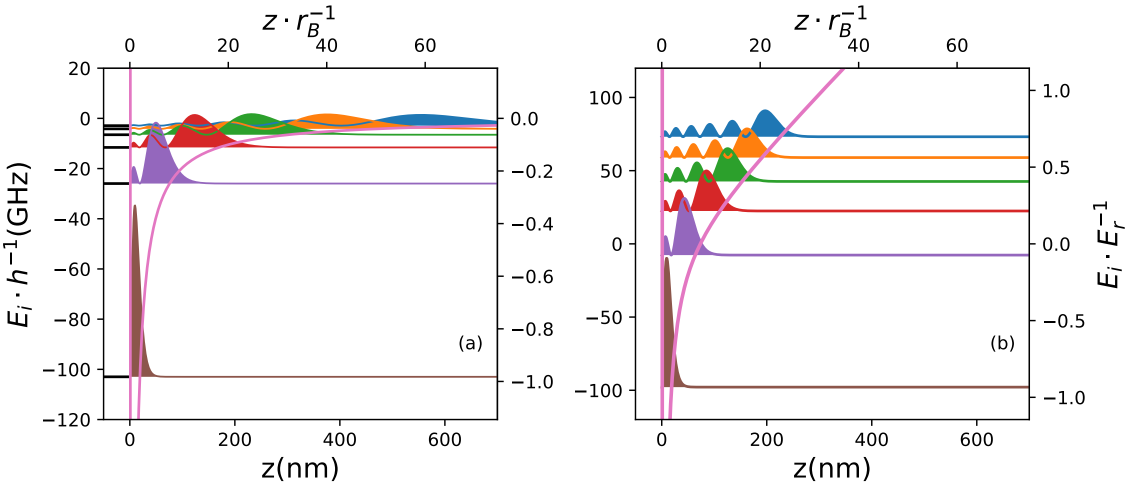

Figure 3.1: Energy eigenvalues (in GHz) and probability densities (in a.u.) for a surface electron on liquid ^{3}He for two values of the perpendicular electric field: $E_\perp = 0$ (a) and $E_\perp = 15$ V/c (b).

The linear dc Stark shift described above provides a very convenient way to tune the transition energies for the Rydberg states in resonance with applied MW radiation [135]. This is a technique that will be used for spectroscopic studies of electrons on helium described in Section 3.3.

3.2.2 Hamiltonian of SE in a tilted magnetic field

When SE are subject to a static magnetic field $\boldsymbol{B} = B_z \boldsymbol{e}_z$ applied perpendicular to the liquid surface, the in-plane orbital motion is quantized into a set of LLs with equidistant energy spectrum $\hbar\omega_c(l+1/2)$, $l = 0, 1, ..$ (see Section 1.2.2). Typically, the in-plane and out-plane motions of an electron are uncoupled, and the full Hamiltonian describing the electron's orbital motion reads

$$H = H_z + \frac{(\boldsymbol{p} + e\boldsymbol{A})^2}{2m_e} = \sum_n E_n \left|n\right\rangle\!\left\langle n\right| + \hbar\omega_c\left(b^\dagger b + \frac{1}{2}\right), \tag{3.2}$$

where $\boldsymbol{p}$ is the operator of in-plane momentum and $\boldsymbol{A}$ is the vector potential which can be chosen, for example, in the Landau gauge $\boldsymbol{A} = (0, B_z x, 0)$. The corresponding eigenstates are the product states $|n, l\rangle$, where $b^\dagger b\,|l\rangle = l\,|l\rangle$. Throughout this chapter we will disregard the spin state of electron because the spin-orbit interaction for SE on liquid helium is negligibly small [40], so the spin degree of freedom is always uncoupled from the orbital motion.

When an additional component of static magnetic field is applied parallel to the liquid surface, in other words when the magnetic field $\boldsymbol{B}$ is tilted with respect to z axis, the eigenstates are no longer the product states $|n, l\rangle$. For certainty, let's consider non-zero components of the applied static magnetic field only in y and z directions and use the Landau gauge for the corresponding vector potential $\boldsymbol{A} = (B_y z, B_z x, 0)$. The total Hamiltonian now reads

$$\begin{aligned}
H &= H_z + \frac{1}{2m_e}(\boldsymbol{p} + e\boldsymbol{A})^2 \\
&= H_z + \frac{1}{2m_e}\left[(p_x + eB_y z)^2 + (p_y + eB_z x)^2\right] \\
&= H_z + \frac{1}{2m_e}\left[p_x^2 + 2eB_y p_x z + e^2 B_y^2 z^2 + p_y^2 + 2eB_z p_y x + e^2 B_z^2 x^2\right],
\end{aligned} \tag{3.3}$$

where the term $eB_y p_x z/m_e$ provides the coupling between the in-plane momentum p_x and coordinate z. The physical picture of this coupling is clear. In the presence of non-zero magnetic field B_y in y direction, an electron experience the Lorentz force in z direction due to the in-plane momentum p_x. This force provides coupling to the orbital motion in z direction.

To simplify the full Hamiltonian (3.3) we notice that with the above choice of the gauge, the canonical momentum operator p_y commutes with H, thus the corresponding eigenvalue p_y is the good quantum number. Note that only the kinematic momentum $\pi_y = p_y + eA_y$, which was introduced in Chapter 1, is gauge invariant and thus corresponds to the physical observable. The gauge transformation $\boldsymbol{A} \to \boldsymbol{A} + \boldsymbol{\nabla} f(\boldsymbol{r})$ does not change physical observables, in particular the Hamiltonian, but can change the Hamiltonian eigenstates. Choosing the eigenstates of (3.3) as the products of $|p_y\rangle$, where $p_y\,|p_y\rangle = p_y\,|p_y\rangle$, and the rest, we can separate (3.3) into the terms

$$\begin{aligned}
H &= H_z + H_{xy} + H_I \\
&= H_z + \left[\frac{p_x^2}{2m_e} + \frac{m_e \omega_c^2 (x - x_0)^2}{2m_e}\right] + \frac{eB_y p_x z}{m_e} \\
&= H_z + \hbar\omega_y\left(b^\dagger b + \frac{1}{2}\right) + \frac{\hbar\omega_y}{\sqrt{2} l_B}(b^\dagger + b) z,
\end{aligned} \tag{3.4}$$

where $\omega_y = eB_y/m_e$, $x_0 = p_y/(m_e\omega_c)$ $(-\infty < p_y < \infty)$, and the new (renormailzed) Hamiltonian H_z for the orbital motion in z direction reads

$$H_z = \frac{p_z^2}{2m_e} + V(z) + eE_\perp z + \frac{m\omega_y^2 z^2}{2} = \sum_i \epsilon_i\,|\phi_i\rangle\langle\phi_i|\,. \tag{3.5}$$

Note that each eigenstate of (3.4) is infinitely degenerate with respect to the x coordinate of the cyclotron orbit x_0 or, equivalently, with respect to the eigenvalue of momentum p_y is the y-direction.

The Hamiltonian (3.4) is reminiscent of the Jaynes-Cummings Model commonly used in cQED [136]

$$H_{\mathrm{JC}} = \frac{\hbar\omega_{12}}{2}\sigma_z + \hbar\omega_c\left(b^\dagger b + \frac{1}{2}\right) + \hbar g(b^\dagger + b)(\sigma^+ + \sigma^-), \tag{3.6}$$

which describes coupling (with the coupling constant g) between a two-level atom and bosonic field of an optical cavity mode. This analogy can be seen by expanding the operator z in (3.4) using the completeness relation for the eigenstates $|\phi_i\rangle$ as $z = \sum_{ij} z_{ij} |\phi_i\rangle \langle\phi_j|$, where $z_{ij} = \langle\phi_i| x |\phi_j\rangle$. Our system can be thought of as an atom with the Rydberg states (renormalized by the diamagnetic term $m_e\omega_c z^2/2$) coupled to the bosonic field of the electron cyclotron motion [134], with the coupling strengths tuned by the value of in-plane field B_y. Although it is tempting to apply the same intuition, we note that the inversion symmetry breaking for z direction in the electron-on-helium system makes the physical picture somewhat different. That is, the non-zero diagonal matrix elements z_{ii} make contributions to the eigenvalues and eigenstates of the coupled system described by (3.4), while it is usually not the case for atoms in a cavity.

The eigenvalues and eigenstates of (3.4) can be obtained numerically, for example by the diagonalization of the matrix representation of (3.4) constructed on a sufficiently large Hilbert sub-space. However, when B_y is not too large, it will be instructive to use the perturbation theory with the basis $|n, l\rangle$ as the eigenstates of the unperturbed Hamiltonian. Then, we can intuitively consider $|n\rangle$ and $|l\rangle$ as two separate degrees of freedom coupled by the small perturbation proportional to B_y. Below, we will present results of both approaches and discuss validity of the perturbation approach.

3.2.3 Dimensionless quantities

As usual, in order to do numerical calculations it is convenient to introduce dimensionless quantities corresponding to real physical ones. Here, we briefly describe the dimensionless quantities used in our calculations and their relation to experimentally measured quantities. In the following, we will use the tilde ($\tilde{\square}$) symbol to denote normalized dimensionless quantities.

First, we define the normalized z coordinate according to $\tilde{z} = z r_{\mathrm{B}}^{-1}$, where $r_{\mathrm{R}} = \hbar^2/(\Lambda m_e)$ is the effective Bohr radius for SE, see the Introduction. Similarly, we define the normalizes energy using the Rydberg energy $E_{\mathrm{r}} = m_e\Lambda^2/(2\hbar^2)$. The normalized potential energy in the z direction reads

$$\tilde{V}(\tilde{z}) = V(z)/E_{\mathrm{r}} = -\frac{2}{\tilde{z}} + \tilde{E}_\perp \tilde{z}, \tag{3.7}$$

where $\tilde{E} = eE_\perp r_B/E_{\mathrm{r}}$ is the dimensionless electric field.

The perpendicular magnetic field B_z can be represented by the normalized cyclotron angular frequency defined by $\tilde{\omega}_c = \hbar\omega_c/E_{\mathrm{r}} = \hbar e B_z/(m_e E_{\mathrm{r}})$. Similarly, for the in-plane magnetic field B_y we define $\tilde{\omega}_y = \hbar\omega_y/E_{\mathrm{r}} = \hbar e B_y/(m_e E_{\mathrm{r}})$.

Using these notations, we can rearrange the full Hamiltonian of the system (3.4) into the dimensionless format

$$\begin{aligned}\tilde{H} &= (H_z + H_{xy} + H_I)/E_{\mathrm{R}} \\ &= \tilde{H}_z + \tilde{\omega}_y\left(b^\dagger b + \frac{1}{2}\right) + \sqrt{\frac{\tilde{\omega}_c}{2}}\tilde{\omega}_y \tilde{z}\left(b^\dagger + b\right),\end{aligned} \tag{3.8}$$

where

$$\tilde{H}_z = -\frac{\partial^2}{\partial \tilde{z}^2} - \frac{2}{\tilde{z}} + \tilde{E}_\perp \tilde{z} + \frac{\tilde{\omega}_y^2}{4}\tilde{z}^2. \tag{3.9}$$

Note that this format is valid for electrons above either liquids ^{3}He or liquid ^{4}He. This is simply determined by the numerical values of the effective Bohr radius r_{B} and the Rydberg energy E_{r}, see Table 3 .

3.2.4 Energy eigenstates of SE in a tilted magnetic field

With the above choice of the gauge, we can separate the contribution of a non-zero in-plane magnetic field B_y in the full Hamiltonian (3.4) into two parts. The first part, which is quadratic in z, appears in the Hamiltonian (3.5) for electron's z motion, thus leads to the renormalization of the corresponding energy eigenvalues ϵ_i. It is clear that this contribution comes from the term quadratic in the vector potential $\boldsymbol{A}$, thus can be called the diamagnetic term in analogy with the CQED model. This term competes with the potential energy of interaction between electron and liquid $V(z)$ and electron and static electric field $eE_\perp z$. For highly excited states, for which the mean value $(z^2)_{ii}$ is large, the diamagnetic term dominates. Therefore, the Hamiltonian (3.5) is close to that of a quantum harmonic oscillator and the energy eigenvalues ϵ_i are approximately proportional to B_y. Oppositely, for the ground and low-lying excited states, the diamagnetic term can be treated as a perturbation for moderate values of B_y. Correspondingly, the energy eigenvalues experience a small shift proportional to B_y^2. For the sake of comparison, Fig. (3.2) shows the energy eigenvalues for five lowest eigenstates of (3.5) calculated for a surface electron on liquid ^{3}He in the perpendicular electric field $E_\perp = 15$ V/cm using the first-order perturbation theory (dotted lines) and numerical solution of the 1D eigenvalue (Schrodinger) equation (solid lines).

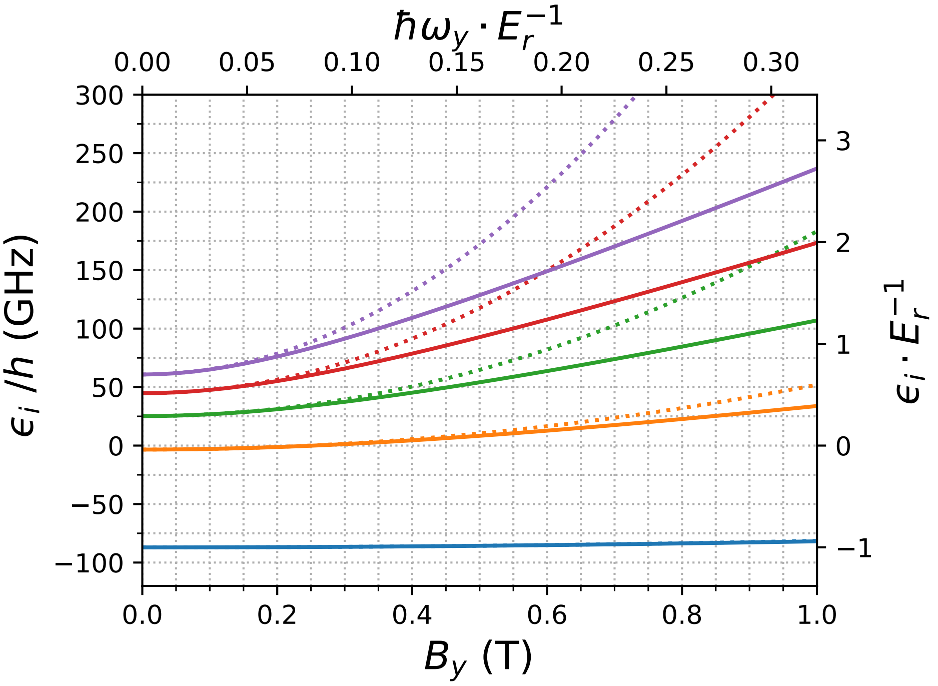

Figure 3.2: Five lowest energy eigenvalues (in GHz) of the Hamiltonian 3.5 for SE on liquid ^{3}He in the perpendicular electric field $E_\perp = 15$ V/cm versus the in-plane magnetic field B_y calculated using the first-order perturbation theory (dashed lines) and numerical solution of the eigenvalue equation (solid lines).

The second contribution of B_y, which is a subject of our major interest, appears as the interaction part H_I in the full Hamiltonian 3.4 and describes the coupling between the electron's z motion and its cyclotron motion in xy plane due to the perpendicular magnetic field B_z. The simple product states $|\phi_i, l\rangle$, which are the eigenstates of the Hamiltonian without the coupling term, are no longer the eigenstates of 3.4. In other words, the coupling term H_I leads to mixing of different product states. It will be convenient for us to use the basis $|n, l\rangle$ of the eigenstates of Hamiltonian (3.2) rather than the basis $|\phi_i, l\rangle$. In Fig. 3.3 we show the energy eigenvalues of the full Hamiltonian 3.4 versus B_z calculated for several values of $B_y = 0$, 0.1, and 0.2 T using the numerical diagonalization of the Hamiltonian's matrix representation in a sub-set of $|n, l\rangle$ with $1 \leq n \leq 6$ and $0 \leq l \leq 50$. For $B_y = 0$, there is a manifold of energy levels $E_{n,l} = E_n + \hbar\omega_c(l + 1/2)$ for each n-th Rydberg state, each shifting linearly with B_z with the slope proportional to l. The largest effect of the non-zero B_y can be seen at the crossings of energy levels of different manifolds. The coupling leads to the avoided crossing of energy levels, which implies the strong mixing between the corresponding product states. Following our CQED analogy, we can talk about the 'dressed states' whose energies at the crossing point are separated by a gap proportional to B_y. This dressed states are a mixture of product states $|n, l\rangle$, thus in general are entangled states of the electron's z motion and in-plane cyclotron motion.

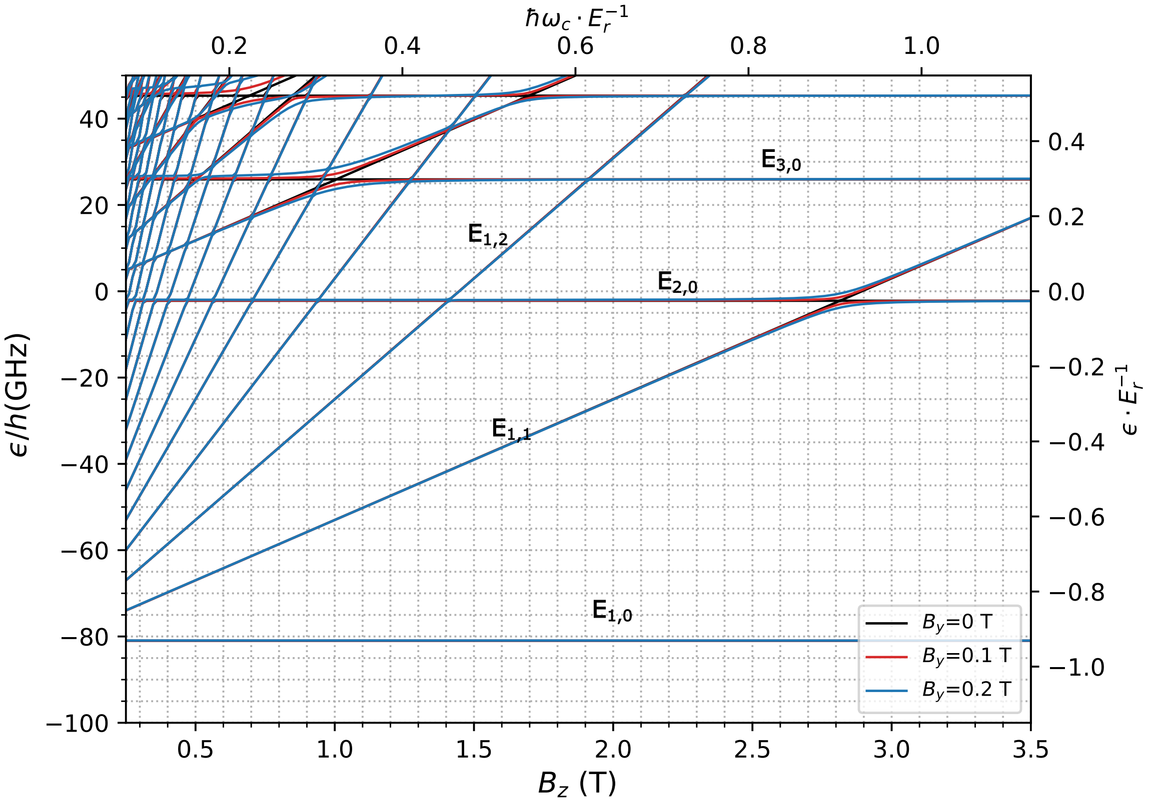

Figure 3.3: Energy eigenvalues (in GHz) of the full Hamiltonian (3.4) for SE on liquid ^{3}He in the perpendicular electric field $E_\perp = 15$ V/cm versus the perpendicular magnetic field B_z. Different colors correspond to the different values of $B_y = 0$ (black lines), 0.1 (red lines), 0.2 T (blue lines).

Using analogy with the CQED model we can say that the above situation, which appears near the level crossings, describes the resonant case of coupling between an atom (the Rydberg states of SE) and a cavity mode (the cyclotron motion of SE). However, even far from the level crossings (the non-resonant case) there is appreciable shift of the energy levels induced by the coupling, which is the anologue of the 'light shift' (or ac Stark shift) in CQED [137]. As will be seen later, this light shifts are on the order of 1 GHz, therefore can be hardly distinguished in Fig. 3.3. However, they can be clearly seen in our experiments as will be described later.

Below, we address the non-resonant and resonant cases of coupling in more details and calculate corresponding shifts, which will be compared with the experimental data in Section 3.4 .

Non-resonant regime of coupling: the light shift

First, it is instructive to consider the non-resonant case far enough from the level crossing where the coupling H_I can be treated as a perturbation. Also, we will be considering sufficiently small values of B_z such that the diamagnetic term $m_e\omega_y^2 z^2/2$ can be treated as a perturbation as well, see Fig. 3.2. As before, it will be convenient to use the basis $|n,l\rangle$ as the eigenstates of the unperturbed Hamiltonian, therefore the Hamiltonian $H_1 = m_e\omega_y^2 z^2/2 + H_I$ as a perturbation. Then, the shift of the unperturbed energy eigenvalues $E_{n.l}^{(0)}$ is the sum of the first-order correction $\Delta E_{n,l}^{(1)}$ due to the diamagnetic term and the second-order correction $\Delta E_{n.l}^{(2)}$ due to the coupling term:

$$\Delta E_{n,l}^{(1)} = \frac{m_e\omega_y^2 (z^2)_{nn}}{2}, \tag{3.10a}$$

$$\Delta E_{n,l}^{(2)} = \frac{\hbar^2\omega_y^2}{2l_B^2} \sum_{(n',l')\neq(n,l)} \frac{|z_{nn'}|^2 \left| \langle l'|b^\dagger + b|l\rangle \right|^2}{E_n^{(0)} - E_{n'}^{(0)} + \hbar\omega_c(l-l')}, \tag{3.10b}$$

where we denote $(z^2)_{nn} = \langle n|z^2|n\rangle$ and $z_{nn'} = \langle n|z|n'\rangle$.

It is interesting that there is strong cancellation between the first and second-order terms, which is reminiscent of the calculations of the Lamb shift in the Hydrogen atom [138] or calculations of the ripplonic Lamb shift in electrons on liquid helium [139]. To see this cancellation, it is convenient to expand $(z^2)_{nn}$ appearing in (3.10) using the completeness relation for basis $|n\rangle$:

$$\langle n|z^2|n\rangle = \sum_{n'} \langle n|z|n'\rangle \, \langle n'|z|n\rangle = \sum_{n'} |z_{nn'}|^2. \tag{3.11}$$

We will also use $\langle l'|b^\dagger + b|l\rangle = \sqrt{l+1}\delta_{l',l+1} + \sqrt{l}\delta_{l',l-1}$. Using the above relations, Eqs. (3.10) become

$$\Delta E_{n,l}^{(1)} = \frac{m_e\omega_y^2}{2}\left[|z_{n1}|^2 + |z_{n2}|^2 + |z_{n3}|^2 + \ldots\right], \tag{3.12a}$$

$$\Delta E_{n,l}^{(2)} = \frac{m_e\omega_y^2}{2}\left[-|z_{nn}|^2 + \sum_{n'\neq n} |z_{nn'}|^2 \left(\frac{l}{E_{nn'}^{(0)}/\hbar\omega_c + 1} + \frac{l+1}{E_{nn'}^{(0)}/\hbar\omega_c - 1}\right)\right]. \tag{3.12b}$$

where we introduced $E_{nn'}^{(0)} = E_n^{(0)} - E_{n'}^{(0)}$, the energy difference between two unperturbed Rydberg states, to shorten notations. It is clear that the leading term in the first-order correction proportional to $|z_{nn}|^2$ is canceled by the corresponding term in the second-order correction. The remaining shift of energy eigenvalues to the second order reads

$$\Delta E_{n,l} = \Delta E_{n,l}^{(1)} + \Delta E_{n,l}^{(2)} = \frac{m_e\omega_y^2}{2}\sum_{n'\neq n} |z_{nn'}|^2 \left(1 + \frac{l}{E_{nn'}^{(0)}/\hbar\omega_c + 1} + \frac{l+1}{E_{nn'}^{(0)}/\hbar\omega_c - 1}\right). \tag{3.13}$$

As a particular example, let us consider the shift in the transition frequency $(E_{2,0} - E_{1,0})/\hbar$, which corresponds to situation when SE occupy the lowest LL with $l = 0$. Setting $l = 0$ in Eq. (3.13), we obtain

$$\Delta E_{1,0} = \frac{m_e\omega_y^2}{2}\left[|z_{12}|^2\left(1+\frac{1}{E_{12}^{(0)}/\hbar\omega_c - 1}\right) + |z_{13}|^2\left(1+\frac{1}{E_{13}^{(0)}/\hbar\omega_c - 1}\right) + \dots\right], \tag{3.14a}$$

$$\Delta E_{2,0} = \frac{m_e\omega_y^2}{2}\left[|z_{12}|^2\left(1+\frac{1}{E_{21}^{(0)}/\hbar\omega_c - 1}\right) + |z_{23}|^2\left(1+\frac{1}{E_{23}^{(0)}/\hbar\omega_c - 1}\right) + \dots\right], \tag{3.14b}$$

and the corresponding shift in the transition energy $\Delta_0 = \Delta E_{2,0} - \Delta E_{1,0}$ is

$$\Delta_0 = \frac{m_e\omega_y^2}{2}\left[|z_{21}|^2\left(\frac{2\hbar\omega_c E_{21}^{(0)}}{E_{21}^{(0)} - \hbar\omega_c}\right) + |z_{23}|^2\left(\frac{E_{32}^{(0)}}{E_{32}^{(0)} + \hbar\omega_c}\right) + |z_{31}|^2\left(\frac{E_{31}^{(0)}}{E_{31}^{(0)} + \hbar\omega_c}\right) + \dots\right]. \tag{3.15}$$

For typical fields $B_z \lesssim 1$ T used in the experiments we have $E_{21}^{(0)} >> \hbar\omega_c$, therefore the above shift is always positive. The shift $\Delta_0/\hbar$ is an anologue of the Lamb shift in the CQED model [137]. It represents the shift of the transition frequency between the Rydberg states of SE due to their interaction with the 'vacuum' state ($l = 0$) of the cyclotron motion. This shift can be experimentally observed and will be discussed in more details in Section 3.4.1.

For the sake of comparison, let us also consider the shift in the transition frequency $(E_{2,1} - E_{1,1})/\hbar$ for SE occupying the first excited LL with $l = 1$. Setting $l = 1$ in Eq. (3.13), we obtain

$$\Delta E_{1,1} \approx \frac{m_e\omega_y^2}{2}\left[|z_{12}|^2\left(1+\frac{1+3(E_{12}^{(0)}/\hbar\omega_c)}{(E_{12}^{(0)}/\hbar\omega_c)^2 - 1}\right) + |z_{13}|^2\left(1+\frac{1+3(E_{13}^{(0)}/\hbar\omega_c)}{(E_{13}^{(0)}/\hbar\omega_c)^2 - 1}\right) + \dots\right], \tag{3.16a}$$

$$\Delta E_{2,1} \approx \frac{m_e\omega_y^2}{2}\left[|z_{12}|^2\left(1+\frac{1+3(E_{21}^{(0)}/\hbar\omega_c)}{(E_{21}^{(0)}/\hbar\omega_c)^2 - 1}\right) + |z_{23}|^2\left(1+\frac{1+3(E_{23}^{(0)}/\hbar\omega_c)}{(E_{23}^{(0)}/\hbar\omega_c)^2 - 1}\right) + \dots\right], \tag{3.16b}$$

and the corresponding shift in the transition energy $\Delta_1 = \Delta E_{2,1} - \Delta E_{1,1}$ is

$$\Delta_1 = \frac{m_e\omega_y^2}{2}\left[|z_{21}|^2\left(\frac{6E_{21}^{(0)}}{(E_{21}^{(0)})^2 - (\hbar\omega_c)^2}\right) + |z_{23}|^2\left(\frac{E_{32}^{(0)}(E_{32}^{(0)} - 3\hbar\omega_c)}{(E_{32}^{(0)})^2 - (\hbar\omega_c)^2}\right) + \dots\right]. \tag{3.17}$$

While for the range of the field B_z considered here the first term in the above equation is positive, the following terms can be either positive or negative. Therefore, the light shift $\Delta_1/\hbar$ in the transition frequency corresponding to the coupling of the Rydberg states to the cyclotron oscillator field with one quantum of excitation ($l = 1$) can be either positive or negative, depending on the range of the field B_z and $E_\perp$. In our

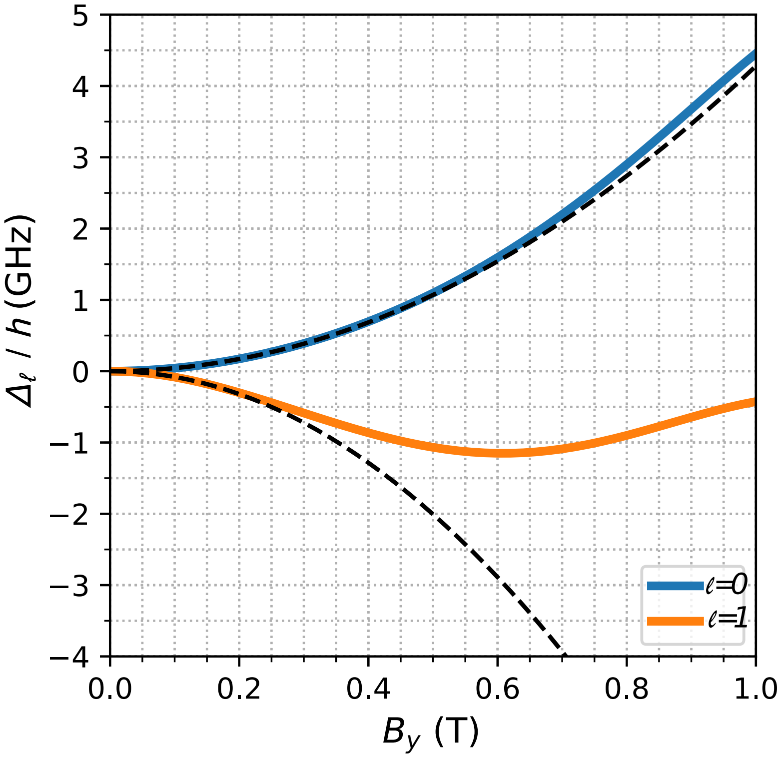

Figure 3.4: The frequency shift of the $|1,0\rangle \rightarrow |2,0\rangle$ transition (blue line) and $|1,1\rangle \rightarrow |2,1\rangle$ transitions (orange line) obtained by the numerical diagonalization of the full Hamiltonian Eq. (3.4) for SE on liquid ^{3}He in the perpendicular magnetic field $B_z = 0.65$ T and perpendicular electric field $E_\perp = 15$ V/cm. For the sake of comparison, dashed lines show corresponding shifts obtained from the second order perturbation theory.

experiments described in Section 3.4, electrons mostly occupy the lowest ($l = 0$) LL, so the observed shift in the transition frequency is positive, see Section 3.4.1 The light shift in the transition frequency due to occupation of the first excited ($l = 1$) LL was observed in Ref. [134] and indeed has negative sign for the considered ranges of fields.

The perturbation approach is valid only for sufficiently low coupling magnetic fields B_y. For large values of B_y one needs to proceed with the diagonalization of the full Hamiltonian (3.4) to deduce the values of the light shifts. The shifts Δ_0 and Δ_1 calculated using the perturbation theory, Eqs. (3.15) and (3.17), are plotted in Fig. 3.4. For the sake of comparison, the shifts calculated using the numerical diagonalization procedure described earlier are plotted on the same figure. It is clear that the perturbation theory does not give adequate description for $B_y \gtrsim 0.2$ T. Comparison with our experimental results will be presented in Section 3.4.1.

Resonant regime: the level anti-crossing

Now, we consider the resonant regime of coupling between the Rydberg states and Landau levels of SE, which is of particular interest to us. This regime is realized at the crossings of energy levels of uncoupled motion, see Fig. 3.3, where the coupling leads to the strong mixing of corresponding eigenstates. Therefore, the perturbation approach is not valid. However, we can obtain essential results by considering only a subspace of degenerate eigenstates of uncoupled motion and perform diagonalization of the full Hamiltonian (3.4) in this subspace. This procedure is similar to the one for JCM [136]. In the resonant regime of coupling, we can consider zero-order perturbation limit with respect to the diamagnetic term, $m_e\omega_y^2 z^2/2$, thus neglect difference between eigenstates $|\phi_i, l\rangle$ of the Hamiltonian (3.5) and the eigenstates $|n, l\rangle$ for zero B_y.

First, it will be convenient to introduce the coupling constants $g_{nn'}$ defined by the expression for the coupling matrix element

$$\langle n, l|H_I|n', l'\rangle = \delta_{l+1,l'}\, g_{nn'}\sqrt{l+1} + \delta_{l-1,l'}\, g_{nn'}\sqrt{l}. \tag{3.18}$$

Using the coupling Hamiltonian from Eq. (3.4) we obtain

$$g_{nn'} = \frac{\hbar\omega_y}{\sqrt{2}\ell_B} z_{nn'} = \sqrt{\frac{\hbar m_e \omega_y^2 \omega_c}{2}}\, z_{nn'}. \tag{3.19}$$

At the crossing of energy levels $E_{n,l+1}$ and $E_{n',l}$, the matrix elements of the full Hamiltonian (3.4) in the subspace of degenerate uncoupled eigenstates $|n, l+1\rangle$ and $|n', l\rangle$ are given by

$$\begin{array}{r|cc} & |n, l+1\rangle & |n', l\rangle \\ \hline \langle n, l+1| & E_{n,l+1} & \sqrt{l+1}\, g_{nn'} \\ \langle n', l| & \sqrt{l}\, g_{n'n} & E_{n',l} \end{array} \tag{3.20}$$

It is convenient to perform an unitary transformation on uncoupled eigenstates according to

$$\begin{pmatrix} |+, l\rangle \\ |-, l\rangle \end{pmatrix} = U \begin{pmatrix} |n, l+1\rangle \\ |n', l\rangle \end{pmatrix} \tag{3.21}$$

which diagonalizes the subspaces. This unitary transformation can be viewed as an $SU(2)$ rotation, which leads to a new basis

$$\begin{aligned} |+, l\rangle &= \cos(\theta_l/2)\,|n', l\rangle + \sin(\theta_l/2)\,|n, l+1\rangle\,, \\ |-, l\rangle &= -\sin(\theta_l/2)\,|n', l\rangle + \cos(\theta_l/2)\,|n, l+1\rangle\,, \end{aligned} \tag{3.22}$$

where the 'mixing angle' θ_l is given by $\theta_l = \arctan\left[g_{nn'}\sqrt{l+1}/(E_{n,l+1} - E_{n',l})\right]$. In the new basis, the matrix elements of the full Hamiltonian (3.4) read

$$\begin{aligned} \langle \pm, l|H_I|\pm, l\rangle =& \frac{1}{2}\left[(E_{n',l} + E_{n,l+1}) \pm \sqrt{(E_{n,l+1} - E_{n',l})^2 + 4(l+1)|g_{nn'}|^2}\right], \\ \langle \pm, l|H_I|\mp, l\rangle =& 0. \end{aligned} \tag{3.23}$$

The diagonal matrix elements $E_{\pm,l} = \langle \pm, l|H_I|\pm, l\rangle$ approximate the energy eigenvalues of the Hamiltonian (3.4). The coupling produces the energy level anti-crossing with the splitting given by $2\sqrt{l+1}|g_{nn'}|$, which scales with l as $\sqrt{l+1}$. Note that this result is similar to JCM, where the (Rabi) splitting between the energy eigenvalues of the two-level atom coupled to the cavity scales with the number of photons in the cavity n_{ph} as $\sqrt{n_{\mathrm{ph}}+1}$.

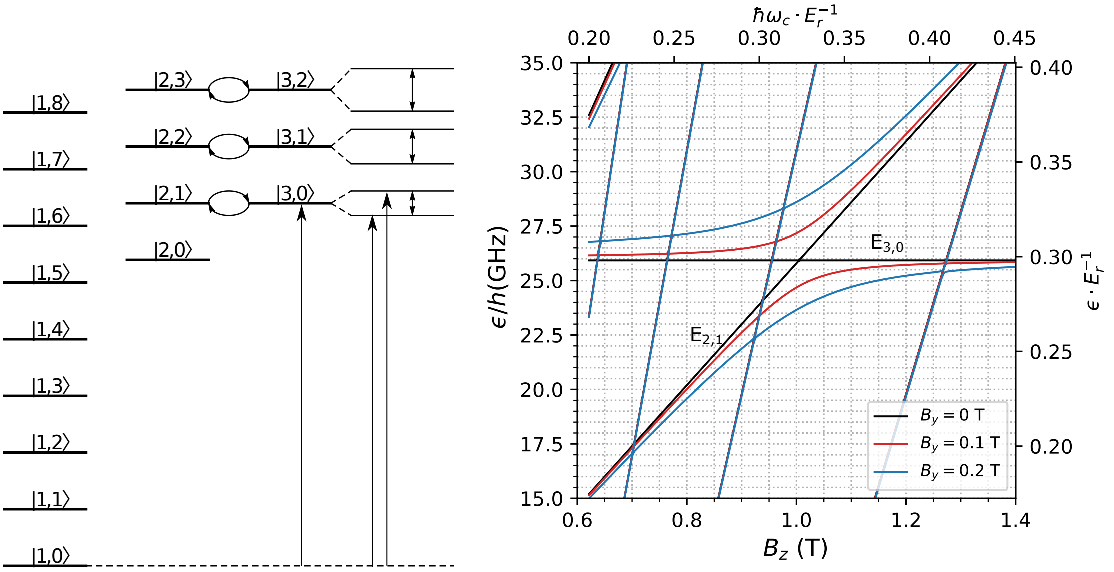

Figure 3.5: (left) Schematic energy level diagram for three lowest Rydberg states. The upward arrows indicate transitions from the lowest energy eigenstate $E_{1,0}$. (right) Energy eigenvalues obtained from the numerical diagonalization of the full Hamiltonian (3.4) for SE on liquid ^{3}He at the pressing field $E_\perp = 15$ V/cm.

As a particular example, let us consider the energy level anti-crossing for $n = 2$ and $n' = 3$. The schematic energy level diagram, which shows the LL manifolds for the ground, the first excited and the second excited Rydberg states, is shown in Fig. 3.5 (left). The magnetic field B_z is assumed to be adjusted such that is causes alignment of the LL manifold for $i = 2$ and $j = 3$. The coupling leads to the splitting of the aligned energy levels $E_{2,l+1}$ and $E_{3,l}$. The energy eigenvalues obtained from the numerical diagonalization of the full Hamiltonian (3.4) are plotted versus B_z in Figure 3.5 (right). As expected from (3.19), the energy splitting at $E_{2,1} = E_{3,0}$ increases linearly with B_y. In the experiment, the splitting can be observed by looking at the microwave-excited transitions between the split energy levels and the ground energy level $E_{1,0}$, as indicated by the upwards arrows in Fig. 3.5 (left). The comparison with experimental results will be discussed in Section 3.4.3.

From Fig. 3.3 (right), it is also evident that there are much weaker anti-crossings involving energy levels $E_{1,3}$ and $E_{1,4}$ at sufficiently large coupling field B_y. This effects comes from the higher-order mixing between different eigenstates, which can be captured only by the diagonalization of the Hamiltonian (3.4) on a sufficiently large subspace of the eigenstates.

3.2.5 Section summary

In summary, we have calculated the eigenstates and energy eigenvalues of SE subject to tilted magnetic fields. This allows us to make certain predictions regarding the spectroscopic properties of this system. In particular, we predict certain features, such as the off-resonant shifts and resonant avoided crossings in the energy spectrum of SE, which can be probed in our experiments by employing the Stark spectroscopy method. More detailed comparison with experimental results also require calculations of the corresponding transition rates, which will be presented in Section 3.4 .

3.3 Experimental method

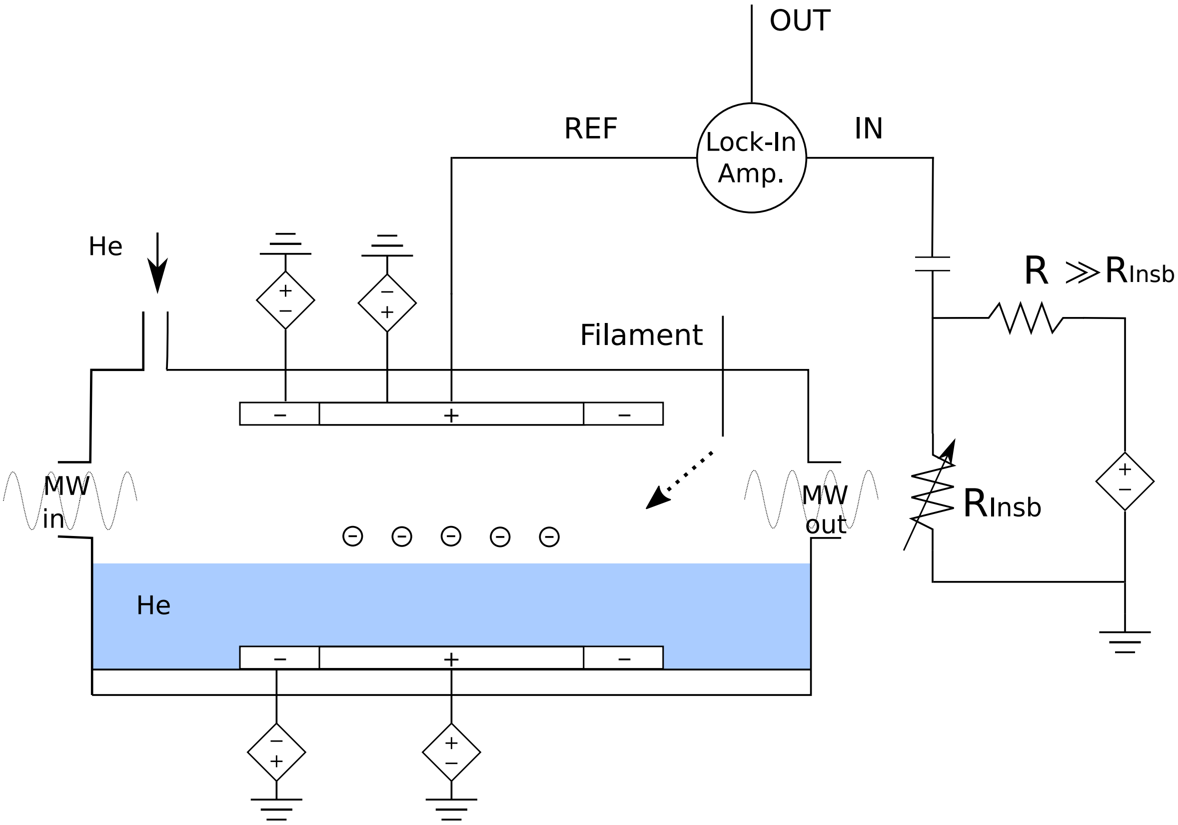

Figure 3.6: Schematic illustration of the experimental setup to perform the Stark spectroscopy of SE on liquid helium.

To check predictions of our calculations regarding the energy spectrum of SE in tilted magnetic field we performed experiments with electrons on liquid ^{3}He using the Stark spectroscopy method. The experimental setup is similar to that which can be found in literature [135, 140]. The main components of our setup are schematically shown in Fig. 3.6. The experiment is performed in a leak-tight cylindrical copper cell cooled down to temperatures below 1 K in a dilution refrigerator. The cell is placed inside a superconducting vector magnet (not shown) which can produce the static magnetic field in both y (horizontal) and z (vertical) directions. The cell can be filled with the ^{3}He gas through a thin capillary tube from a room temperature storage tank (not shown). The cell has two side windows located opposite to each other. This windows serve as input and output ports for microwave (MW) radiation which is used to excite transitions between energy eigenstates of SE. Both windows are sealed with the Kapton film using the Stycast epoxy to prevent leakage of helium from the cell into the vacuum space of the refrigerator.

Inside the cell, there are two round metal discs of diameter $D = 18$ mm which form a parallel-plate capacitor with the distance between the plates $d = 2$ mm. ^{3}He gas, which is introduced into the cell, is condensed in the cooled cell until the surface of liquid helium covers the bottom disk and the liquid's level is set approximately in the middle between the bottom and top disks. Free electrons are injected into the space above the liquid's surface from a tungsten filament (shown schematically) by thermionic emission, while applying a positive voltage V_{BOT} to the bottom disk. As a result, the injected electrons are attracted towards the liquid surface and form a round pool of charge on the surface just above the positively biased bottom disk. With a positive voltage applied to the bottom disk, SE can be held on the surface of liquid helium infinitely long. In addition, each metal disk is surrounded by a metal ring of outer diameter 22 mm, which serve as guard rings. By applying a negative voltage V_{GURD} to the guard rings, electrons can be stronger confined on the liquid surface to prevent their escape to the grounded walls of the experimental cell.

To excite quantum transitions between the Rydberg states of SE, the MW radiation in the 100 GHz range is transmitted into the cell from a room-temperature source (not shown) through a waveguide coupled to the input port of the cell. In the experiment, the frequency ω of the MWs is fixed, while the transition frequency of SE is tuned, by means of the DC Stark effect, to match the MW frequency by sweeping the perpendicular electric field $E_\perp \approx V_{\mathrm{BOT}}/d$. This comprises the essence of the Stark spectroscopy method.

In our experiments, we measure the absorption of the MW radiation due to resonant transitions induced in SE by detecting the change in the power of MW radiation transmitted through the cell. In order to measure the transmitted power, the output MW port of the cell is coupled to a cryogenic hot-electron (InSb) bolometer which changes its resistance R_{InSb} when it is heated by the incident MW radiation. To observe change in the bolometer resistance, we pass a DC current $I \approx 100$ μA generated by a DC battery and measure the voltage drop across the bolometer IR_{InSb}. To detect variation in the transmitted MW power due to the resonant transitions in SE, we apply a small modulating AC voltage $V_{\mathrm{ac}} = 40$ mV$_{\mathrm{RMS}}$ at the frequency $f_{\mathrm{m}} \approx 10$ kHz to the top metal disk of the parallel-plate capacitor. Due to the Stark shift, this modulates the detuning of the transition frequency of SE with respect to the MW frequency, therefore the MW power absorbed by SE and the MW power transmitted through the cell. The corresponding modulation of the voltage across the bolometer is then detected using the conventional lock-in amplifier operated at the modulation frequency f_{m}.

An example of the bolometer signal recorded by the lock-in amplifier for SE at $B_z = 0.7$ T, $B_y = 1$ T, and under presence of the microwave radiation at the frequency $\omega/2\pi = 90$ GHz is shown in Fig. 3.7 (left). For this frequency, the observed signal corresponds to the transition from the ground ($n = 1$) state to the first excited ($n = 2$) Rydberg state of SE. By keeping an amplitude of the modulating voltage V_{ac} to be much

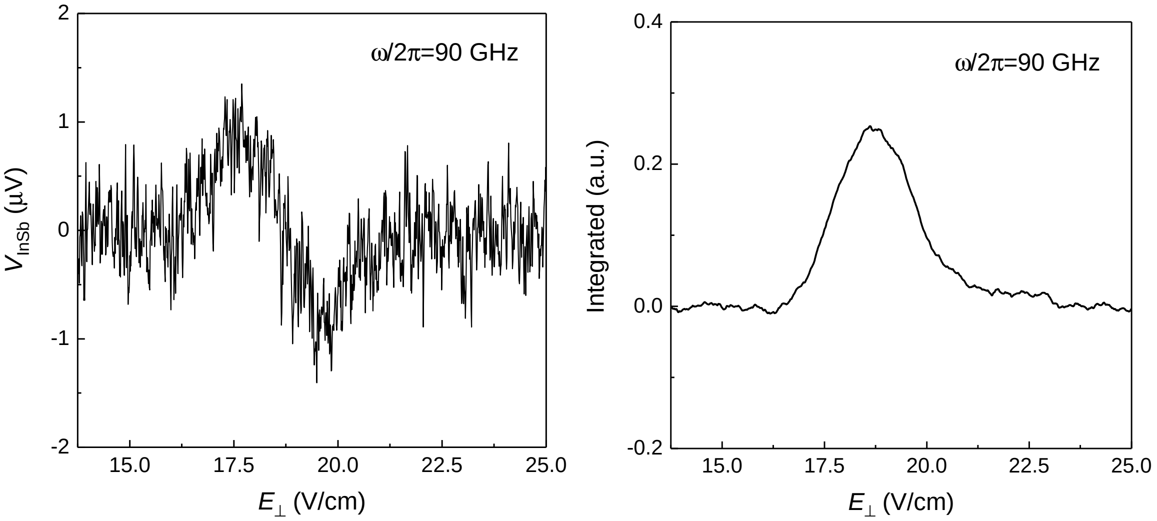

Figure 3.7: (left) Bolometer signal recorded by sweeping the perpendicular electric field $E_\perp$ exerted on electrons to tune the $n = 1 \to 2$ transition between the Rydberg states of SE at $B_z = 0.7$ T, $B_y = 1$ T, and in resonance with MWs at frequency $\omega/2\pi = 90$ GHz. (right) Integrated bolometer signal which gives the absorption line due to the $n = 1 \to 2$ transition.

smaller than the width of the transition line, we record the derivative of the transition line. Then, the transition line can be obtained from the recorded bolometer signal by the numerical integration, see Fig. 3.7 (right). The center of the line corresponds to the perpendicular electric field $E_\perp \approx 20$ V/cm, which agrees reasonably well with the expected transition frequency $\omega_{12}/2\pi = 90$ GHz of the Stark-shifted energy levels of electrons on liquid ^{3}He.

To measure energy spectrum of SE in tilted magnetic fields, we record transition lines measured by the above method either for a fixed value of B_z and different values of B_y, or for a fixed value of B_y and different values of B_z. The results will be presented on 2D color plots of the bolometer signals versus the corresponding B-field (horizontal axis) and $E_\perp$-field (vertical axis). All data presented here were taken at the temperature of the cell $0.3 \leq T \leq 0.33$ K measured by a ruthenium-oxide thermometer attached to the cell's top.

3.4 Experimental results and comparison with calculation

We restrict the scope of our experimental study to the changes in the spectroscopic properties of the $n = 1 \to 2$ and $n = 1 \to 3$ Rydberg transitions of SE in tilted magnetic fields[1]. To summarize our key experimental observations, we reproduced a few spectroscopic signatures predicted by our theoretical analysis given above:

- The off-resonant Lamb shift in the $|1, 0\rangle \to |2, 0\rangle$ transition, which is approxi-

---

[1] The experimental data presented in this section were obtained by Aleksiy A. Zadorozhko.

mately second order in B_y.

- The resonant coupling between $|3,0\rangle$ and $|2,1\rangle$, which is approximately first order in B_y.
- The sideband transitions, namely the blue sideband, $|1,0\rangle \to |2,1\rangle$ and the red sideband, $|1,1\rangle \to |2,0\rangle$, which have increasing transition moments as B_y increases.

3.4.1 The Lamb shift

First, we address the non-resonant light shift of the $n = 1 \to 2$ transition between the Rydberg states in tilted magnetic field, see Section 3.2.4. In the experiment, the shift can be seen by observing the evolution of the transition line at a fixed value of B_z and different values of B_y, which changes the coupling between the Rydberg states and LLs. An example of experimental data taken at $B_z = 0.584$ T and the excitation frequency $\omega/2\pi = 90$ GHz are shown in Fig. 3.8. Fig. 3.8 (left) shows the bolometer signal recorded by sweeping the perpendicular electric field $E_\perp$ for different values of $0 \leq B_y \leq 1$ T, while Fig. 3.8 (right) shows the corresponding transition line obtained by the numerical integration. The shift of the transition frequency with respect to its value at $B_y = 0$ is plotted in Fig. 3.9. Here, we used the conversion coefficient $\alpha_{12} = 0.74$ GHz·cm/V, which is the slope of the $(E_2^{(0)} - E_1^{(0)})/h$ versus $E_\perp$ dependence, which was obtained in the experiment by measuring the transition line for different values of $E_\perp$ at zero magnetic field.

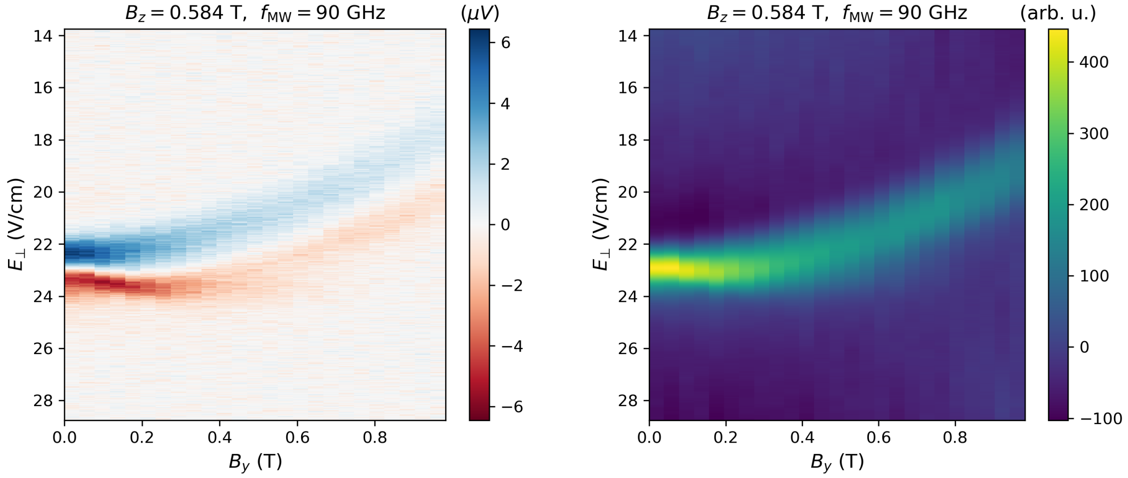

Figure 3.8: (left) Bolometer signal recorded for SE irradiated by 90 GHz microwave radiation while sweeping the perpendicular electric field $E_\perp$ for different values of $0 \leq B_y \leq 1$ T and a fixed value of the perpendicular magnetic field $B_z = 0.584$ T. (right) MW absorption signal obtained by numerical integration of the bolometer signal shown on the left.

Assuming that the electron system is in the thermal equilibrium with the liquid helium at temperature $T = 0.33$ K, for $B_z = 0.584$ T, which corresponds to the spacing between LLs equal to $\hbar\omega_c/k_B = 0.8$ K, the electrons mostly occupy the lowest ($l = 0$) Landau level. Thus, the shift observed in Fig. 3.9 corresponds to the Lamb shift Δ_0. As expected from our discussion in Section 3.2.4, this shift is positive, see Eq. (3.15). For the sake of comparison, the solid line shows the shift obtained by the numerical diagonalization of the full Hamiltonian 3.4.

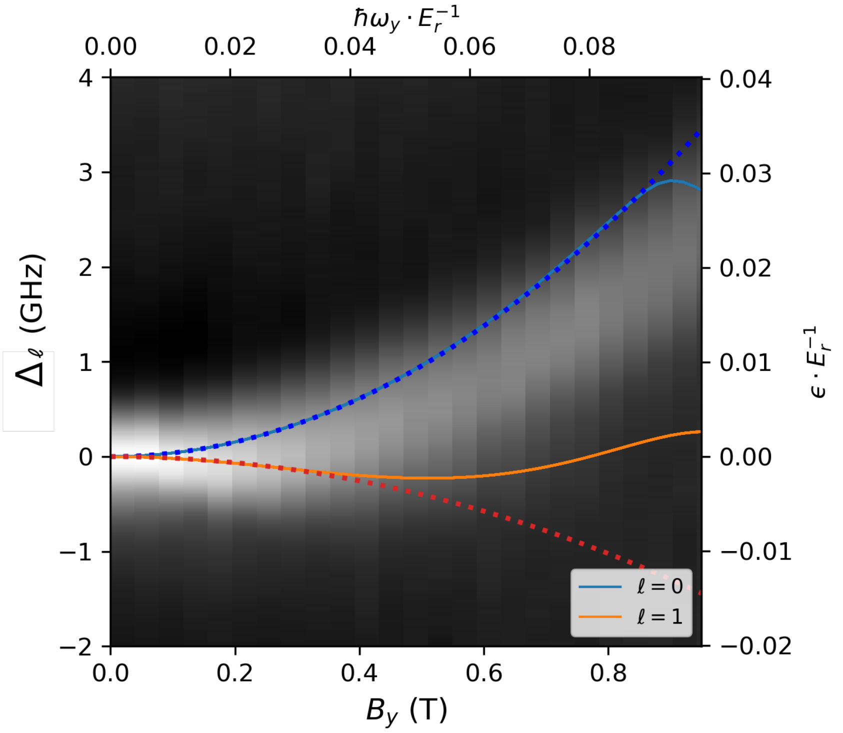

Figure 3.9: Shift in the $n = 1 \to 2$ transition frequency obtained from data shown in Fig. 3.8. Blue (orange) solid line is the theoretical result for $|1,0\rangle \to |2,0\rangle$ ($|1,1\rangle \to |2,1\rangle$) transition obtained from the numerical diagonalization of the full Hamiltonian (3.4). Dashed lines are results of the second-order perturbation theory, see Section 3.2.

At $T = 0.3$ K, there is a small (about 9%) thermal population of the first excited $l = 1$ Landau level. Therefore, in addition to the $n = 1 \to 2$ Rydberg transition for electrons occupying $l = 0$ state, there is a corresponding transition for electrons occupying $l = 1$ state. This transition is visible in our experimental data as a splitting that appears at $B_y \sim 0.3$ T, see Fig. 3.9. As discussed in Section 3.4.1, the light shift Δ_1 of this transition due to the coupling to LLs can have an opposite (negative) sign, as shown by the solid line obtained from our numerical calculations. In other words, the coupling of the Rydberg states to the LLs line non-zero B_y leads to the splitting of the transition line when there is appreciable population of the excited Landau states. Note that this splitting in the $n = 1 \to 2$ transition line in non-zero B_y was also observed in Ref. [134].

3.4.2 Sideband transitions

As discussed in Section 3.2.4, the coupling due to the in-plane magnetic field B_y leads to the mixing between different eigenstates $|n,l\rangle$ of the uncoupled Hamiltonian. This can be readily seen in the off-resonance regime by applying the first order perturbation theory to find corrections to the eigenstates $|\Psi\rangle$ of the full Hamiltonian (3.4):

$$\begin{aligned}|\Psi\rangle^{(1)} &= |n,l\rangle + \sum_{(n',l')\neq(n,l)} \frac{\langle n,l|\, H_1\, |n',l'\rangle}{E^{(0)}_{n,l} - E^{(0)}_{n',l'}} |n',l'\rangle \\ &= |n,l\rangle + \frac{m_e\omega_y^2}{2}\sum_{n'\neq n}\frac{(z^2)_{n'n}}{E^{(0)}_{nn'}}|n',l\rangle + \frac{\hbar\omega_y}{\sqrt{2}l_B}\sum_{n'}\frac{z_{n'n}\sqrt{l+\frac{1}{2}(1\pm 1)}}{E^{(0)}_{nn'}\mp\hbar\omega_c}|n',l\pm 1\rangle\end{aligned} \tag{3.24}$$

where $H_1 = m_e\omega_y z^2/2 + H_\mathrm{I}$. One of the effects of such mixing was discussed in the previous section. Another prominent effect of the mixing of states is appearance of the sideband transitions. Without coupling between the Rydberg states and LLs, one expects to conserve the quantum number l during the radiation-induced transitions $|n,l\rangle \to |n',l\rangle$ between the Rydberg states. Indeed, the transition rate in the electrical dipole (E1) approximation is given by the Fermi's golden rule

$$\Gamma_{n\to n'} = \frac{2\pi}{\hbar}|\langle n',l'|\,|V|\,|n,l\rangle|\delta\Big(E^{(0)}_{n',l'} - E^{(0)}_{n,l} - \hbar\omega\Big), \tag{3.25}$$

where $V = eE_0 z$ (E_0 is the amplitude of the MW electric field). The transition moment $\langle n,l|\, z\, |n',l'\rangle = z_{nn'}\delta_{l,l'}$, therefore the transition rate $\Gamma_{n\to n'}$, is zero when $l' \neq l$. It is clear, however, that when the initial and final states are mixtures of states with different l, there will be transitions $|n,l\rangle \to |n',l'\rangle$ with $l \neq l'$. Again, it is instructive to consider the perturbative limit of coupling. In the second order perturbation theory, the rate of transition between an initial state $|i\rangle = |n,l\rangle$ and a final state $|f\rangle = |n',l'\rangle$ reads

$$\Gamma_{i\to f} = \frac{2\pi}{\hbar}\left|\sum_{|m\rangle\neq|i\rangle}\left[\frac{\langle f|\, V\, |m\rangle\, \langle m|\, H_1\, |i\rangle}{E^{(0)}_{n'',l''} - E^{(0)}_{n,l}} + \frac{\langle f|\, H_1\, |m\rangle\, \langle n'',l''|\, V\, |i\rangle}{E^{(0)}_{n'',l''} - E^{(0)}_{n,l} - \hbar\omega}\right]\right|^2 \delta\Big(E^{(0)}_{n',l'} - E^{(0)}_{n,l} - \hbar\omega\Big), \tag{3.26}$$

where $|m\rangle = |n'', l''\rangle$ is an intermediate state. For the transitions which change the quantum number l by 1, that is $l' = l \pm 1$, we obtain

$$\begin{aligned}\Gamma_{l'=l\pm1} =& \frac{\pi(eE_0\hbar\omega_y)^2}{\hbar l_B^2} \\ & \left|\sum_{n''}\left[\frac{z_{n'n''}z_{n''n}\sqrt{1+\frac{1}{2}(l\pm1)}}{E^{(0)}_{n''n} \pm \hbar\omega_c} + \frac{z_{n'n''}z_{n''n}\sqrt{1+\frac{1}{2}(l\pm1)}}{E^{(0)}_{n''n} - \hbar\omega}\right]\right|^2 \\ & \delta\Big(E^{(0)}_{n'n} \pm \hbar\omega_c - \hbar\omega\Big).\end{aligned} \tag{3.27}$$

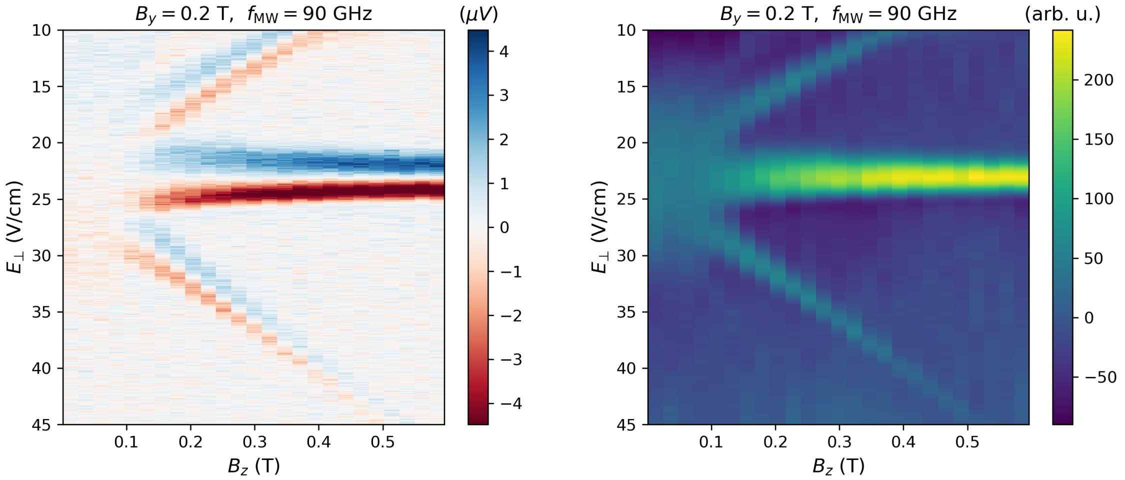

Figure 3.10: (left) Bolometer signal recorded for SE irradiated by 90 GHz microwave radiation while sweeping the perpendicular electric field $E_\perp$ for different values of $0 \leq B_z \leq 0.6$ T and a fixed value of the in-plane magnetic field $B_y = 0.1$ T. (right) MW absorption signal obtained by numerical integration of the bolometer signal shown on the left.

In particular, this can result in the absorption of the MW radiation due to the 'blue' sideband transition, $|1,0\rangle \rightarrow |2,1\rangle$, and the 'red' sideband transition, $|1,1\rangle \rightarrow |2,0\rangle$. Indeed, such sideband transitions can be observed in the experiment. Figure 3.10 (left) and Figure 3.10 (right) show the bolometer signal and the absorption signal, respectively, measured for SE irradiated with 90 GHz microwaves at fixed in-plane magnetic field $B_y = 0.2$ T and different values of the perpendicular magnetic field $0 \leq B_z \leq 0.6$ T. The absorption signal whose position in $E_\perp$-field does not depend on the magnetic field correspond corresponds to the resonant $|1,0\rangle \rightarrow |2,0\rangle$ transition line. Two branches whose position in $E_\perp$-field varies linearly with B_z correspond to the sideband transitions. It is convenient to replot the absorption signal as a function of the cyclotron frequency ω_c and the frequency detuning from the $|1,0\rangle \rightarrow |2,0\rangle$ transition $\Delta\omega_{21}$, where $\omega_{21} = (E_2^{(0)} - E_1^{(0)})$ see Fig. 3.11. As expected from Eq. (3.27), the frequencies of sideband transitions, $\omega_{21} \pm \omega_c$, vary linearly with ω_c with the slope equal to ±1.

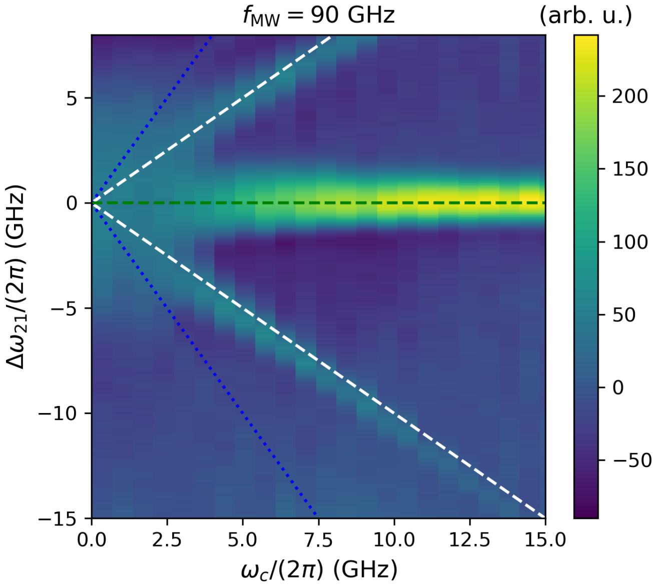

Figure 3.11: MW absorption signal shown in Fig. 3.10 replotted versus the cyclotron frequency (horizontal axis) and frequency detuning from the $n = 1 \rightarrow 2$ resonance in zero magnetic field (vertical axis). The white (blue) dashed lines plot the linear dependence $\Delta\omega_{21} = \pm\omega_c$ ($\Delta\omega_{21} = \pm 2\omega_c$).

Note that at low values of $B_z \lesssim 0.1$ T, the $n = 1 \rightarrow 2$ transition line is smeared in the non-zero in-plane magnetic field B_y. This effect has been described in the literature [141] and arises due to the broadening of the transition line in SE subject to a parallel magnetic field. As electrons move randomly along the surface of liquid helium with average thermal velocity v_x in x-direction, they experience the Lorentz force in z-direction due to the in-plane field B_y. This leads to the fluctuating effective electric field in z-direction with RMS amplitude $(E_\perp)_{\rm rms} = \sqrt{k_B T/m_e} B_y$, where T is the electron temperature. For typical temperature of the experiment $T \sim 1$ K, the RMS effective electric field in V/cm is $\sim 37 B_y$, where B_y is in T. Thus, an in-plane magnetic field $B_y = 0.2$ T leads to the large broadening of the transition line $\Delta E_\perp \approx 7$ V/cm, see Fig. 3.10 (right). At sufficiently large perpendicular magnetic field B_z, the electron in-plane motion becomes quantized, so he broadening of the transition line due to the electron thermal motion becomes suppressed.

In addition to the sideband transitions which are accompanied by change of the quantum number l by ±1, there should be also much weaker higher-order sideband transitions which are accompanied by change of the quantum number l by ±2, ±3, etc. These are indicated in Fig. 3.11 by the dashed blue lines.

3.4.3 Avoided level crossing and interference

Finally, we consider the effect of coupling between the eigenstates $|n, l\rangle$ and $|n', l \pm 1\rangle$ near their energy level crossing (the resonant regime). As discussed in Section 3.2.4, the coupling Hamiltonian H_I leads to the avoided crossing of the energy levels of the coupled (mixed) states. As shown in Fig. 3.3, such an avoided crossing is expected, for example, for the energy eigenstates with $n = 1$ and $n' = 2$ in the perpendicular magnetic field $B_z \sim 3$ T. Unfortunately, such a large field was beyond specification limits of our vector magnet. Instead, in our experiment we studied the avoided level crossing between eigenstates with $n = 2$ and $n' = 3$, see the energy level diagram in Fig. 3.3 (left). Some exemplary data sets are shown in Fig. 3.12, where the dependence of the MW absorption signal on the perpendicular magnetic field B_z is shown for several different values of the in-plane magnetic field: $B_y = 0$ (top left), 0.1 (top right), 0.2 (bottom left), and 0.4 T (bottom right). In this experiment, the electrons where excited from the ground $n = 1$ Rydberg state using MWs at the frequency $\omega/2\pi = 120.5$ GHz. At $B_y = 0$, see the top left panel in Fig. 3.12, we observe the absorption signal due to $|1,0\rangle \to |3,0\rangle$ transition, which frequency is independent of the perpendicular magnetic field B_z. At $B_y = 0.1$ T (top right), the 'blue' sideband $|1,0\rangle \to |2,1\rangle$ transition, whose frequency intersects that of the $|1,0\rangle \to |3,0\rangle$ transition at $B_z \approx 1.18$ T, becomes visible. The avoided crossing between the transition frequencies is clearly observed. As the coupling field B_y increases further, see the bottom panels in Fig. 3.12, the sideband transition becomes stronger and the splitting between two transition line at the level crossing increases.

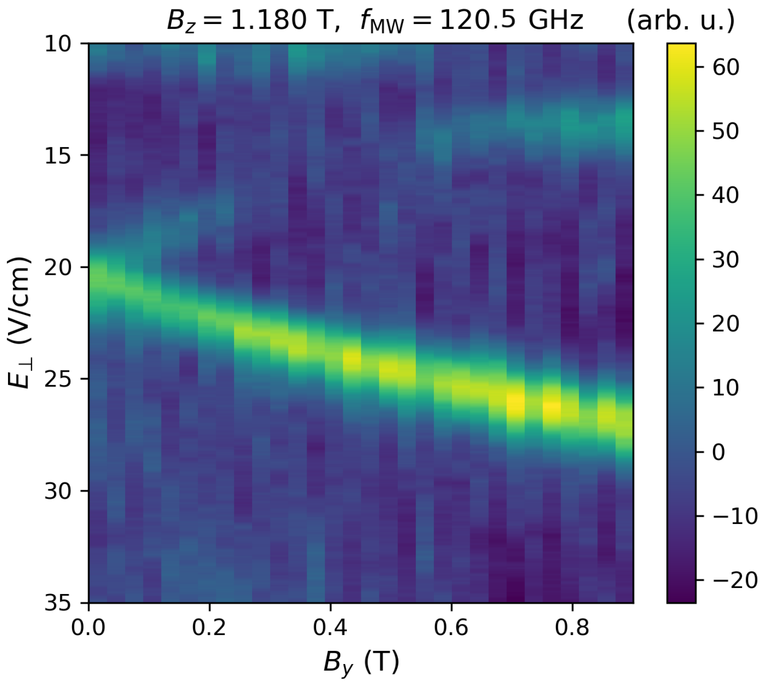

Figure 3.13: MW absorption signal measured at the level crossing point $B_z = 1.18$ T, see Fig. 3.12, for different values of the in-plane magnetic field $0 \leq B_y \leq 0.9$.

As it follows from our discussion in Section 3.2.4, the two transition lines at the avoided level crossing correspond (in zero-order perturbation limit) to the transitions from the ground $|1,0\rangle$ Rydberg state to two hybridized states $|\pm,1\rangle = \beta_{1,2}^{(\pm)} |2,1\rangle +$

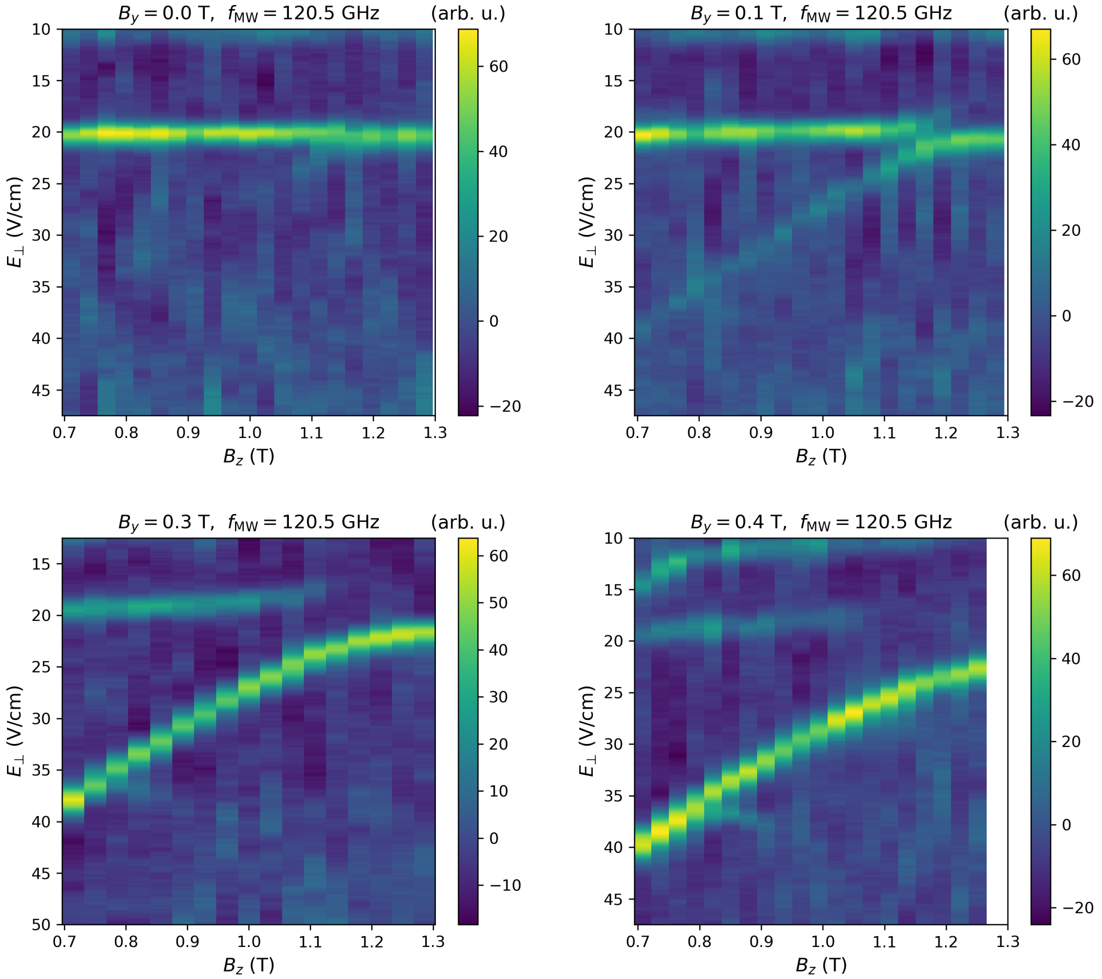

Figure 3.12: MW absorption signal measured for SE irradiated with MWs at the frequency $\omega/2\pi = 120.5$ GHz at four different values of the coupling field $B_y = 0$ (top left), 0.1 (top right), 0.2 (bottom left), and 0.4 T (bottom right).

$\beta_{3,0}^{(\pm)} |3,0\rangle$. The observed splitting of the transition line at the level crossing is reminiscent to the Auter-Townes effect. It is instructive to plot the split transition line measured exactly at the uncoupled level crossing, that is at $B_z = 1.18$ T, for different values of the coupling field B_y. Such a graph is shown in Fig. 3.13. Here, the absorption signal is plotted for different values of $0 \leq B_y \leq 0.9$. The splitting between two branches increases approximately linearly with B_y. An unusual feature of the data shown in Figs. 3.12 and 3.13 is apparent disappearance of the upper branch in a certain range of B_y. To understand this effect we have to discuss the transition matrix element (transition moment) which determines the transition rate according to the Fermi's golden rule, see Eq. 3.25. Assuming that in the experiment the MW radiation used to excite transitions in SE is linearly polarized in z direction, the transition rate is proportional to $|\langle i|z|f\rangle|^2$, where $|i\rangle$ is the initial state and $|f\rangle$ is the final state. In general, due to the coupling Hamiltonian H_I and the diamagnetic term $m_e\omega_y^2 z^2/2$, both the initial and final states are the mixtures of different state products $|n,l\rangle$. Let

$\alpha_{n,l} \equiv \langle n, l|i\rangle$ and $\beta_{n,l} \equiv \langle n, l|f\rangle$ be the complex coefficients in the expansions

$$|i\rangle = \sum_{n,l} \alpha_{n,l} |n, l\rangle , \quad |f\rangle = \sum_{n,l} \beta_{n,l} |n, l\rangle . \tag{3.28}$$

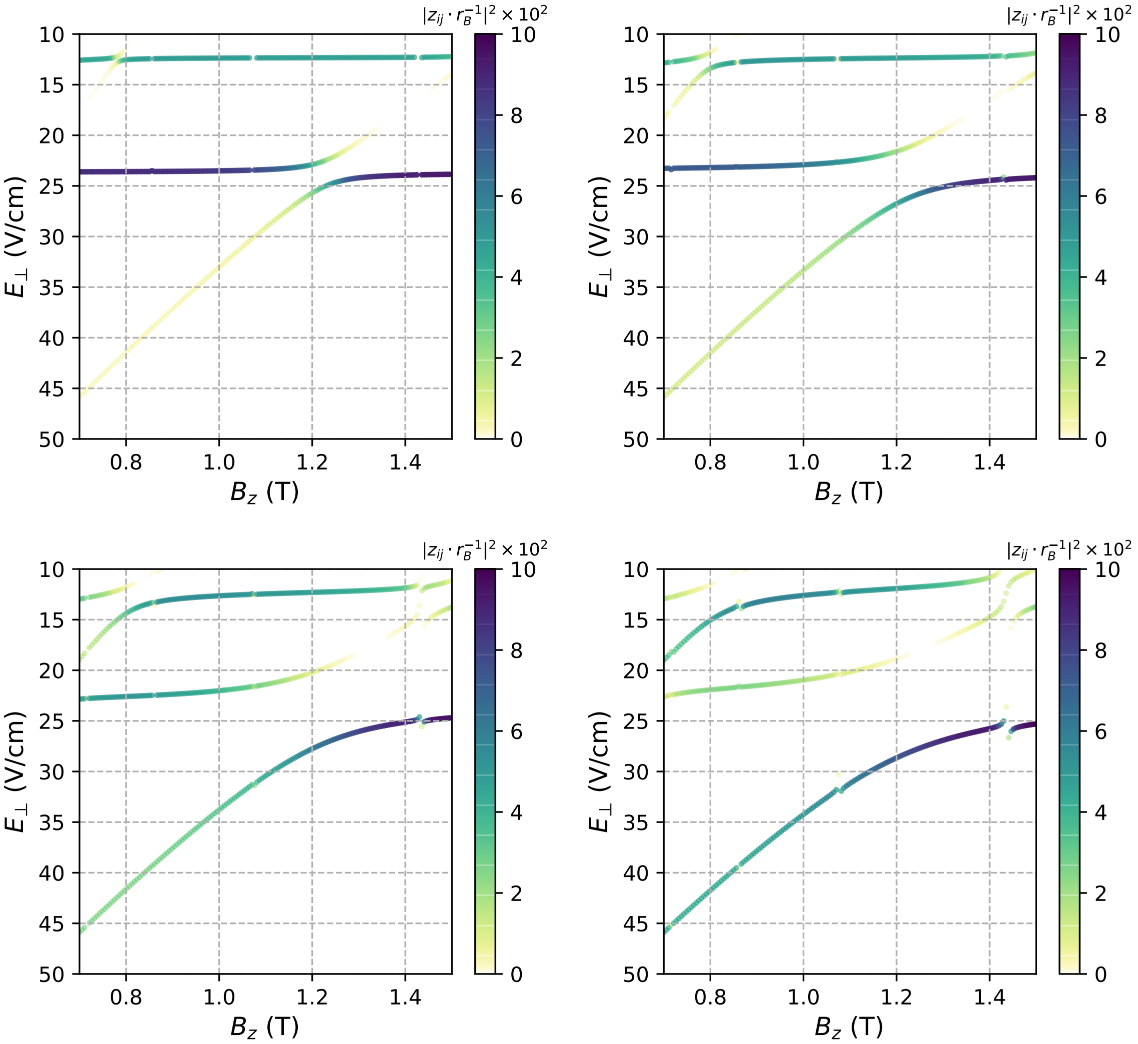

Figure 3.14: Calculated squares of the transition moments for transitions shown in Fig. 3.12. Parameters used for the simulation: $f_{\mathrm{MW}} = 120$ GHz, $B_y = 0.1$ T (top left), 0.2 (top right), 0.3 (bottom left), and 0.4 T (bottom right).

Correspondingly, the value of $|\langle i|z|f\rangle|^2$ is given by

$$|\langle i|z|f\rangle|^2 = \left| \sum_{n,n'} \alpha^*_{n,l} \beta_{n',l} z_{nn'} \right|^2 . \tag{3.29}$$

For two different branches in Fig. 3.13, that is for two different sets of complex coefficients $\beta_{n',l}$, the square of transition moment can be larger/smaller depending on the constructive/destructive interference of different terms in Eqs. (3.29). The transition

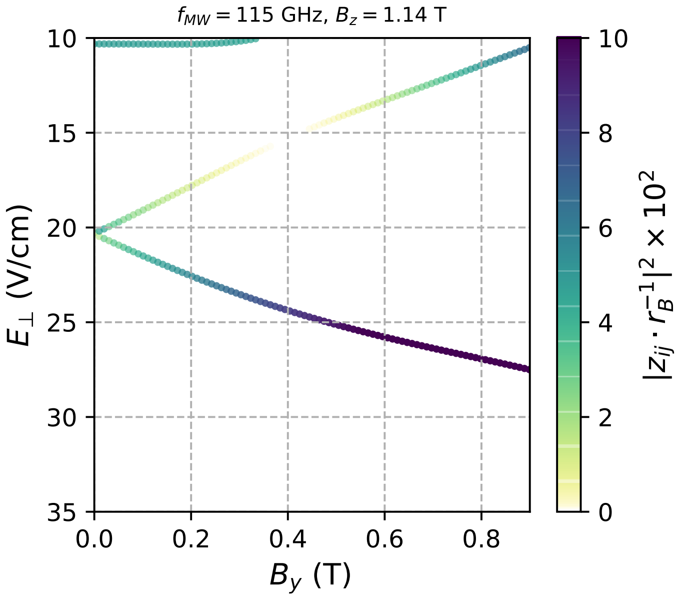

Figure 3.15: Calculated squares of the transition moments for transitions shown in Fig. 3.13. The value of f_{MW} and B_z are adjusted such that the two branches are at resonance when $B_y = 0$.

moments for transition lines in Figs. 3.12 and 3.13 obtained by numerical diagonalization of the full Hamiltonian (3.4) are shown in Figs. 3.14 and 3.15. In this figures, the calculated square of the transition moment is plotted as the color tone of the line for the corresponding transition. Our numerical calculations are able to reproduce main features of the experimental data quite well. In particular, the MW absorption, which is proportional to the transition rate, therefore the square of the transition moment, increases for the lower branch and decreases for the upper branch with the increasing coupling field B_y. Note that the calculated resonance are shifted towards somewhat higher values of $E_\perp$ comparing with the experimental data. This agrees with the fact that the approximate model of infinitely large potential barrier at the surface, which was used in our calculations, underestimates the transition energies between the Rydberg states, as was discussed in the Introduction.

Finally, in addition to the resonant (non-perturbative) avoided crossings between coupled states $|n, l\rangle$ and $|n', l \pm 1\rangle$, we also observed the higher-order (perturbative) avoided crossings. Fig. 3.16 shows an example of such effects. This data are taken for SE excited by the MW radiation with frequency $\omega/2\pi = 110$ GHz at a fixed value of the coupling field $B_y = 0.3$ T. The dark horizontal line at $E_\perp \approx 52$ V/cm corresponds to the $|1, 0\rangle \rightarrow |2, 0\rangle$ transition. several sideband transitions are also visible. In particular, the sideband transition $|1, 0\rangle \rightarrow |2, 1\rangle$ shows a pronounced avoided crossing at $B_z \approx 1$ T where it supposes to cross the $|1, 0\rangle \rightarrow |3, 0\rangle$ transition, which occurs at $E_\perp = 12$ V/cm. In addition, a much smaller avoided crossing is seen for a higher-order sideband transition $|1, 0\rangle \rightarrow |2, 2\rangle$ at $B_z \approx 0.5$ T where it is supposed to cross the $|1, 0\rangle \rightarrow |3, 0\rangle$ transition. This also agrees well with our calculations.

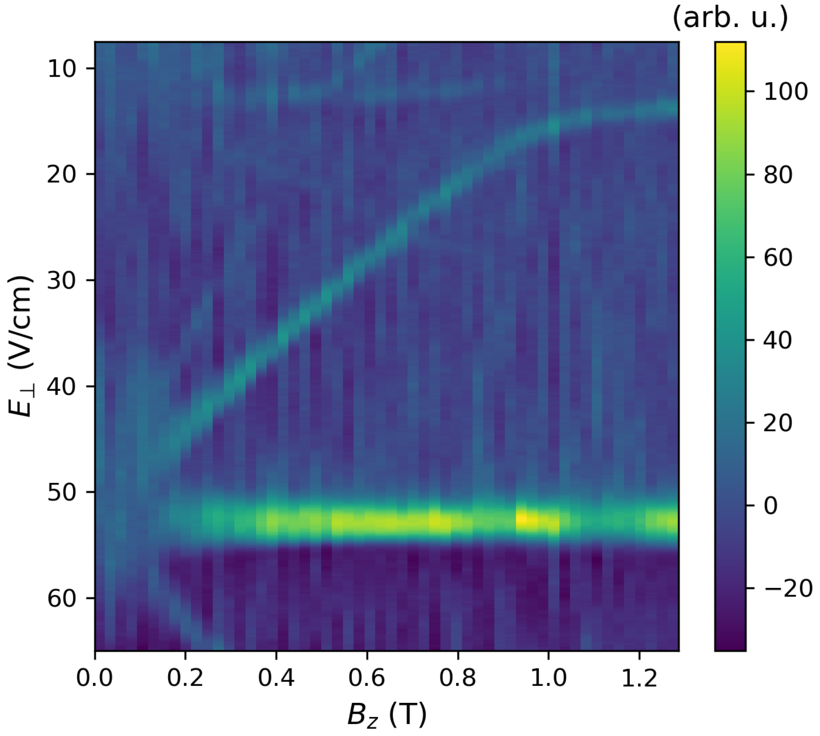

Figure 3.16: MW absorption signal measured for SE irradiated with MWs at the frequency $\omega/2\pi = 110$ GHz at a fixed value of the coupling field $B_y = 0.3$ T.

3.5 Chapter summary

In this Chapter, we demonstrated that the bound surface (Rydberg) states and the states of the in-plane motion of SEs on liquid helium can be coupled by an applying in-plane magnetic field. In case of a sufficiently strong applied perpendicular magnetic field, which causes quantization of the in-plane motion, this system realizes the famous Jaynes-Cummings Model from cQED. In our case, the Rydberg states with their non-equidistant energy levels represent an atom, while the Landau levels of the quantized cyclotron motion represent quantized EM field of the cavity mode. The coupling introduced by the in-plane magnetic field produces mixed (dressed) eigenstates of the orbital motion of SEs, which exhibit many phenomena familiar from AMO. We predicted this phenomena by our numerical calculations of the eigenstates and corresponding eigenvalues of the coupled orbital motion of SE, as well as confirmed them in the experiment.

These findings already provide some interesting possibilities, for example simulation of the cQED models using the orbital states of electrons on helium. As demonstrated by our experiments, the Stark spectroscopy of the energy levels can be used as a robust method to obtain information about eigenstates for such models. Another useful method can be measuring the electrical transport of SE using the conventional capacitive coupling (Sommer-Tanner) method, which was described in Chapter 1. However, the study of electrical transport of SE is beyond the scope of this work. Instead, our main interests in the coupled orbital motion of SE in a tilted magnetic field comes from the possibility to combine this system with our optical (Fabry-Perot) cavities to study coherent control of the orbital motion of electrons by light. This is briefly discussed in the next section, which will conclude this thesis.

Conclusions and Outlook

The results described in this thesis contribute to the current progress towards the goal of coherent control of charged particles, in particular the surface electrons on liquid helium, using quantized electromagnetic field. Here, I would like to highlight the main findings of this work, as well as outline some future directions.

The two experimental works presented here serve as proof-of-concept studies towards the coherent control of SEs on helium by employing the strong coupling regime of interaction between SEs and EM field of an optical cavity mode. In Chapter 1, we have demonstrated the strong coupling between the circularly polarized mode in a microwave (Fabry-Perot) resonator and the cyclotron motion of electrons in a perpendicular magnetic field. In Chapter 3, we have shown that in a tilted magnetic field, the surface bound (Rydberg) states of SEs couple to the cyclotron motion of electrons. These two experimental accomplishments open door to realizing the strong coupling regime of interactions between the Rydberg states of SEs and an EM mode in our cavity resonators. Owing to the inherent non-linearity of the Rydberg spectrum, it is a promising plan to realize some cQED-type of experiments using this new and extremely clean platform.

In the course of this experimental work I developed some comprehensive and useful theoretical models to describe this system. I confirmed that all predictions of these models agree well with the data obtained in the experiments. In Chapter 1, I showed that both the normal-mode splitting, as well as an anomaly appearing in the CR-passive circularly polarized mode, can be completely accounted by a full quantum mechanical model, even though in this particular case it is completely equivalent to the classical treatment. In Chapter 3, I used a physical model that is similar to the JCM to describe the electrons in a tilted magnetic field. In all theoretical models, there are no adjustable parameters needed, except the phenomenological scattering time which accounts for the interaction of SEs with the surface ripplons. Such a robustness and high reliability of the simple theoretical models stems from the fact that the electrons-on-helium system is extremely pure and well-defined.

In the future, one can drive the experimental work using this platform in two directions. Firstly, one must develop experimental techniques for the detection and manipulation of the quantum states of a single electron. This can lead to very interesting experiments, as well as to some real applications related to quantum information process. Secondly, one may include more complicated interactions in future experiments, as well as in our theoretical analysis, for example, the Coulomb interaction between electrons and the spin-orbit interaction. One can also extend the scope of this work to include the electrical transport properties of SEs. This could lead to new insights into many-body physics and new experimental realizations of many-body models.

Sometimes, one finds some new and surprising features in well-known theoretical models, such as the Jaynes-Cummings models, when one look at it from a different perspective. This was the case for the theoretical project discussed in Chapter 2. In this project, I developed a proposal to prepare squeezed states and spin-squeezed states in an abstract system that can be described by the driven JCM. This proposal can be experimentally tested in systems where the particle states are strongly coupled to light. Potentially, one may implement the squeezed state preparation protocol presented in Chapter 2 to the electrons-on-helium system in future work. However, some new experimental methods need to be developed to do that.

In this thesis, the interaction between the electrons and their environment, in particular the helium vapor atoms and surface ripplons, was neglected. This can be partially justified since the coupling strength of the electrons to the EM field is much stronger than the coupling strength to the environment. In future work, it will be desirable to also include the interaction term describing the coupling of SEs to the ripplons in order to account for such experimentally observed quantities as the linewidth of the quantum transitions and the electrical resistivity of SEs. To fully describe our system we have to use open quantum system methods such as the quantum master equations.

Bibliography

[1] D. P. DiVincenzo, D. Bacon, J. Kempe, G. Burkard, and K. B. Whaley, *Universal quantum computation with the exchange interaction*, Nature **408**, 339 (2000).

[2] M. A. Nielsen and I. Chuang, *Quantum computation and quantum information*, AAPT (2002).

[3] J. I. Cirac and P. Zoller, *Quantum computations with cold trapped ions*, Physical Review Letters **74**, 4091 (1995).

[4] N. Gisin and R. Thew, *Quantum communication*, Nature photonics **1**, 165 (2007).

[5] J. Esteve, C. Gross, A. Weller, S. Giovanazzi, and M. Oberthaler, *Squeezing and entanglement in a Bose–Einstein condensate*, Nature **455**, 1216 (2008).

[6] W. Wasilewski, K. Jensen, H. Krauter, J. J. Renema, M. Balabas, and E. S. Polzik, *Quantum noise limited and entanglement-assisted magnetometry*, Physical Review Letters **104**, 133601 (2010).

[7] L. Pezzè, A. Smerzi, M. K. Oberthaler, R. Schmied, and P. Treutlein, *Quantum metrology with nonclassical states of atomic ensembles*, Reviews of Modern Physics **90**, 035005 (2018).

[8] J. Q. You, X.-F. Shi, X. Hu, and F. Nori, *Quantum emulation of a spin system with topologically protected ground states using superconducting quantum circuits*, Physical Review B **81**, 014505 (2010).

[9] R. Blatt and C. F. Roos, *Quantum simulations with trapped ions*, Nature Physics **8**, 277 (2012).

[10] I. M. Georgescu, S. Ashhab, and F. Nori, *Quantum simulation*, Reviews of Modern Physics **86**, 153 (2014).

[11] J. Dalibard, *Introduction to the physics of artificial gauge fields*, Quantum Matter at Ultralow Temperatures, Proceedings of the International School of Physics "Enrico Fermi **191**, 1–61 (2015).

[12] S. Haroche and J. Raimond. *Radiative properties of Rydberg states in resonant cavities.* In *Advances in atomic and molecular physics*, volume 20, pages 347–411. Elsevier, (1985).

[13] C. Guerlin, E. Brion, T. Esslinger, and K. Mølmer, *Cavity quantum electrodynamics with a Rydberg-blocked atomic ensemble*, Physical Review A **82**, 053832 (2010).

[14] C. Blockley, D. Walls, and H. Risken, *Quantum collapses and revivals in a quantized trap*, EPL (Europhysics Letters) **17**, 509 (1992).

[15] J. Cirac, R. Blatt, A. Parkins, and P. Zoller, *Quantum collapse and revival in the motion of a single trapped ion*, Physical Review A **49**, 1202 (1994).

[16] M. Lukin, M. Fleischhauer, R. Cote, L. Duan, D. Jaksch, J. Cirac, and P. Zoller, *Dipole blockade and quantum information processing in mesoscopic atomic ensembles*, Physical Review Letters **87**, 037901 (2001).

[17] A. Wallraff, D. I. Schuster, A. Blais, L. Frunzio, R.-S. Huang, J. Majer, S. Kumar, S. M. Girvin, and R. J. Schoelkopf, *Strong coupling of a single photon to a superconducting qubit using circuit quantum electrodynamics*, Nature **431**, 162 (2004).

[18] A. Berkley, H. Xu, R. Ramos, M. Gubrud, F. Strauch, P. Johnson, J. Anderson, A. Dragt, C. Lobb, and F. Wellstood, *Entangled macroscopic quantum states in two superconducting qubits*, Science **300**, 1548–1550 (2003).

[19] A. Imamoğlu, *Cavity QED Based on Collective Magnetic Dipole Coupling: Spin Ensembles as Hybrid Two-Level Systems*, Physical Review Letters **102**, 083602 (2009).

[20] M. Aspelmeyer, T. J. Kippenberg, and F. Marquardt, *Cavity optomechanics*, Reviews of Modern Physics **86**, 1391 (2014).

[21] J. Q. You and F. Nori, *Quantum information processing with superconducting qubits in a microwave field*, Physical Review B **68**, 064509 (2003).

[22] M. Wallquist, K. Hammerer, P. Rabl, M. Lukin, and P. Zoller, *Hybrid quantum devices and quantum engineering*, Physica Scripta **2009**, 014001 (2009).

[23] Y. Kubo, C. Grezes, A. Dewes, T. Umeda, J. Isoya, H. Sumiya, N. Morishita, H. Abe, S. Onoda, T. Ohshima, et al., *Hybrid quantum circuit with a superconducting qubit coupled to a spin ensemble*, Physical Review Letters **107**, 220501 (2011).

[24] G. Kurizki, P. Bertet, Y. Kubo, K. Mølmer, D. Petrosyan, P. Rabl, and J. Schmiedmayer, *Quantum technologies with hybrid systems*, Proceedings of the National Academy of Sciences **112**, 3866–3873 (2015).

[25] Z.-L. Xiang, S. Ashhab, J. You, and F. Nori, *Hybrid quantum circuits: Superconducting circuits interacting with other quantum systems*, Reviews of Modern Physics **85**, 623 (2013).

[26] M. I. Dykman, P. M. Platzman, and P. Seddighrad, *Qubits with electrons on liquid helium*, Physical Review B **67**, 155402 (2003).

[27] S. A. Lyon, *Spin-based quantum computing using electrons on liquid helium*, Physical Review A **74**, 1–6 (2006).

[28] G. Yang, A. Fragner, G. Koolstra, L. Ocola, D. A. Czaplewski, R. J. Schoelkopf, and D. I. Schuster, *Coupling an Ensemble of Electrons on Superfluid Helium to a Superconducting Circuit*, Physical Review X **6**, 011031 (2016).

[29] D. I. Schuster, A. P. Sears, E. Ginossar, L. DiCarlo, L. Frunzio, J. J. L. Morton, H. Wu, G. A. D. Briggs, B. B. Buckley, D. D. Awschalom, and R. J. Schoelkopf, *High-Cooperativity Coupling of Electron-Spin Ensembles to Superconducting Cavities*, Physical Review Letters **105**, 140501 (2010).

[30] M. W. Cole and M. H. Cohen, *Image-potential-induced surface bands in insulators*, Physical Review Letters **23**, 1238 (1969).

[31] M. W. Cole, *Properties of Image-Potential-Induced Surface States of Insulators*, Physical Review B **2**, 4239–4252 (1970).

[32] V. Shikin, *Motion of helium ions near a vapor-liquid surface*, Sov. Phys. JETP **31**, 936–940 (1970).

[33] W. T. Sommer and D. J. Tanner, *Mobility of Electrons on the Surface of Liquid* ^{4}He, Physical Review Letters **27**, 1345–1349 (1971).

[34] C. C. Grimes and T. R. Brown, *Direct Spectroscopic Observation of Electrons in Image-Potential States Outside Liquid Helium*, Physical Review Letters **32**, 280–283 (1974).

[35] H. Isshiki, D. Konstantinov, H. Akimoto, K. Shirahama, and K. Kono, *Microwave Absorption of Surface-State Electrons on Liquid 3He*, Journal of the Physical Society of Japan **76**, 094704 (2007).

[36] E. Y. Andrei, *Two-Dimensional Electron Systems: On Helium and Other Cryogenic Substrates*, Springer Science & Business Media (2012).

[37] Y. Monarkha and K. Kono, *Two-dimensional Coulomb liquids and solids*, Springer Science & Business Media (2013).

[38] D. Konstantinov, M. I. Dykman, M. J. Lea, Y. Monarkha, and K. Kono, *Resonant Correlation-Induced Optical Bistability in an Electron System on Liquid Helium*, Physical Review Letters **103**, 096801 (2009).

[39] J. D. Pritchard, D. Maxwell, A. Gauguet, K. J. Weatherill, M. Jones, and C. S. Adams, *Cooperative atom-light interaction in a blockaded Rydberg ensemble*, Physical Review Letters **105**, 193603 (2010).

[40] S. Lyon, *Spin-based quatum computer using electrons on liquid helium*, Physical Review A **74**, 052338 (2004).

[41] J. Chen, A. A. Zadorozhko, and D. Konstantinov, *Strong coupling of a two-dimensional electron ensemble to a single-mode cavity resonator*, Physical Review B **98**, 235418 (2018).

[42] Y. Kaluzny, P. Goy, M. Gross, J. M. Raimond, and S. Haroche, *Observation of Self-Induced Rabi Oscillations in Two-Level Atoms Excited Inside a Resonant Cavity: The Ringing Regime of Superradiance*, Physical Review Letters **51**, 1175–1178 (1983).

[43] M. G. Raizen, R. J. Thompson, R. J. Brecha, H. J. Kimble, and H. J. Carmichael, *Normal-mode splitting and linewidth averaging for two-state atoms in an optical cavity*, Physical Review Letters **63**, 240–243 (1989).

[44] Y. Zhu, D. J. Gauthier, S. E. Morin, Q. Wu, H. J. Carmichael, and T. W. Mossberg, *Vacuum Rabi splitting as a feature of linear-dispersion theory: Analysis and experimental observations*, Physical Review Letters **64**, 2499–2502 (1990).

[45] R. J. Thompson, G. Rempe, and H. J. Kimble, *Observation of normal-mode splitting for an atom in an optical cavity*, Physical Review Letters **68**, 1132–1135 (1992).

[46] H. J. Carmichael, R. J. Brecha, M. G. Raizen, H. J. Kimble, and P. R. Rice, *Subnatural linewidth averaging for coupled atomic and cavity-mode oscillators*, Physical Review A **40**, 5516–5519 (1989).

[47] H. J. Carmichael, R. J. Brecha, and P. R. Rice, *Quantum interference and collapse of the wavefunction in cavity QED*, Optics Communications **82**, 73–79 (1991).

[48] O. O. Soykal and M. E. Flatté, *Strong Field Interactions between a Nanomagnet and a Photonic Cavity*, Physical Review Letters **104**, 077202 (2010).

[49] J. H. Wesenberg, A. Ardavan, G. A. D. Briggs, J. J. L. Morton, R. J. Schoelkopf, D. I. Schuster, and K. Mølmer, *Quantum Computing with an Electron Spin Ensemble*, Physical Review Letters **103**, 070502 (2009).

[50] I. Diniz, S. Portolan, R. Ferreira, J. M. Gérard, P. Bertet, and A. Auffèves, *Strongly coupling a cavity to inhomogeneous ensembles of emitters: Potential for long-lived solid-state quantum memories*, Physical Review A **84**, 063810 (2011).

[51] B. Julsgaard, C. Grezes, P. Bertet, and K. Mølmer, *Quantum Memory for Microwave Photons in an Inhomogeneously Broadened Spin Ensemble*, Physical Review Letters **110**, 250503 (2013).

[52] Y. Kubo, F. R. Ong, P. Bertet, D. Vion, V. Jacques, D. Zheng, A. Dréau, J.-F. Roch, A. Auffeves, F. Jelezko, J. Wrachtrup, M. F. Barthe, P. Bergonzo, and D. Esteve, *Strong Coupling of a Spin Ensemble to a Superconducting Resonator*, Physical Review Letters **105**, 140502 (2010).

[53] H. Wu, R. E. George, J. H. Wesenberg, K. Mølmer, D. I. Schuster, R. J. Schoelkopf, K. M. Itoh, A. Ardavan, J. J. L. Morton, and G. A. D. Briggs, *Storage of Multiple Coherent Microwave Excitations in an Electron Spin Ensemble*, Physical Review Letters **105**, 140503 (2010).

[54] R. Amsüss, C. Koller, T. Nöbauer, S. Putz, S. Rotter, K. Sandner, S. Schneider, M. Schramböck, G. Steinhauser, H. Ritsch, J. Schmiedmayer, and J. Majer, *Cavity QED with Magnetically Coupled Collective Spin States*, Physical Review Letters **107**, 060502 (2011).

[55] E. Abe, H. Wu, A. Ardavan, and J. J. L. Morton, *Electron spin ensemble strongly coupled to a three-dimensional microwave cavity*, Applied Physics Letters **98**, 251108 (2011).

[56] H. Huebl, C. W. Zollitsch, J. Lotze, F. Hocke, M. Greifenstein, A. Marx, R. Gross, and S. T. B. Goennenwein, *High Cooperativity in Coupled Microwave Resonator Ferrimagnetic Insulator Hybrids*, Physical Review Letters **111**, 127003 (2013).

[57] M. Goryachev, W. G. Farr, D. L. Creedon, Y. Fan, M. Kostylev, and M. E. Tobar, *High-Cooperativity Cavity QED with Magnons at Microwave Frequencies*, Physical Review Applied **2**, 054002 (2014).

[58] Y. Tabuchi, S. Ishino, T. Ishikawa, R. Yamazaki, K. Usami, and Y. Nakamura, *Hybridizing Ferromagnetic Magnons and Microwave Photons in the Quantum Limit*, Physical Review Letters **113**, 083603 (2014).

[59] X. Zhang, C.-L. Zou, L. Jiang, and H. X. Tang, *Strongly Coupled Magnons and Cavity Microwave Photons*, Physical Review Letters **113**, 156401 (2014).

[60] L. Bai, M. Harder, Y. P. Chen, X. Fan, J. Q. Xiao, and C.-M. Hu, *Spin Pumping in Electrodynamically Coupled Magnon-Photon Systems*, Physical Review Letters **114**, 227201 (2015).

[61] L. V. Abdurakhimov, Y. M. Bunkov, and D. Konstantinov, *Normal-Mode Splitting in the Coupled System of Hybridized Nuclear Magnons and Microwave Photons*, Physical Review Letters **114**, 226402 (2015).

[62] G. Scalari, C. Maissen, D. Turčinková, D. Hagenmüller, S. De Liberato, C. Ciuti, C. Reichl, D. Schuh, W. Wegscheider, M. Beck, and J. Faist, *Ultrastrong Coupling of the Cyclotron Transition of a 2D Electron Gas to a THz Metamaterial*, Science **335**, 1323–1326 (2012).

[63] Q. Zhang, M. Lou, X. Li, J. L. Reno, W. Pan, J. D. Watson, M. J. Manfra, and J. Kono, *Collective non-perturbative coupling of 2D electrons with high-quality-factor terahertz cavity photons*, Nature Physics **12**, 1005 (2016).

[64] L. V. Abdurakhimov, R. Yamashiro, A. O. Badrutdinov, and D. Konstantinov, *Strong Coupling of the Cyclotron Motion of Surface Electrons on Liquid Helium to a Microwave Cavity*, Physical Review Letters **117**, 056803 (2016).

[65] H. Kogelnik and T. Li, *Laser beams and resonators*, Applied Optics **5**, 1550–1567 (1966).

[66] V. B. Shikin, *Cyclotron resonace for electrons over helium confined in a resonator*, JETP Letters **75**, 29 (2002).

[67] D. F. Walls and G. J. Milburn, *Quantum optics*, Springer Science & Business Media (2007).

[68] M. J. Collett and C. W. Gardiner, *Squeezing of intracavity and traveling-wave light fields produced in parametric amplification*, Physical Review A **30**, 1386–1391 (1984).

[69] C. C. Grimes and G. Adams, *Observation of Two-Dimensional Plasmons and Electron-Ripplon Scattering in a Sheet of Electrons on Liquid Helium*, Phys. Rev. Lett. **36**, 145–148 (1976).

[70] V. Edel'man, *Nonlinear cyclotron resonance of electrons localized over the surface of liquid helium*, JETP Lett **25**, 118 (1977).

[71] V. Édel'man, *Investigation of the resonance properties of electrons localized above liquid 3He and 4He*, Soviet Journal of Experimental and Theoretical Physics **50**, 338 (1979).

[72] J. Chen, D. Konstantinov, and K. Mølmer, *Adiabatic preparation of squeezed states of oscillators and large spin systems coupled to a two-level system*, Physical Review A **99**, 013803 (2019).

[73] G. Kurizki, P. Bertet, Y. Kubo, K. Mølmer, D. Petrosyan, P. Rabl, and J. Schmiedmayer, *Quantum technologies with hybrid systems*, Proceedings of the National Academy of Sciences **112**, 3866–3873 (2015).

[74] J. Plebanski, *Wave functions of a harmonic oscillator*, Physical Review **101**, 1825 (1956).

[75] B. Mollow and R. Glauber, *Quantum theory of parametric amplification. I*, Physical Review **160**, 1076 (1967).

[76] H. P. Yuen, *Two-photon coherent states of the radiation field*, Physical Review A **13**, 2226–2243 (1976).

[77] R. W. Henry and S. C. Glotzer, *A squeezed-state primer*, American Journal of Physics **56**, 318–328 (1988).

[78] A. Bienfait, P. Campagne-Ibarcq, A. Kiilerich, X. Zhou, S. Probst, J. Pla, T. Schenkel, D. Vion, D. Esteve, J. Morton, et al., *Magnetic resonance with squeezed microwaves*, Physical Review X **7**, 041011 (2017).

[79] E. Jaynes and F. Cummings, *Comparison of quantum and semiclassical radiation theories with application to the beam maser*, Proceedings of the IEEE **51**, 89–109 (1963).

[80] P. Knight and P. Radmore, *Quantum origin of dephasing and revivals in the coherent-state Jaynes-Cummings model*, Physical Review A **26**, 676 (1982).

[81] G. Agarwal, *Vacuum-field Rabi splittings in microwave absorption by Rydberg atoms in a cavity*, Physical Review Letters **53**, 1732 (1984).

[82] G. Agarwal and R. Puri, *Collapse and revival phenomenon in the evolution of a resonant field in a Kerr-like medium*, Physical Review A **39**, 2969 (1989).

[83] H. J. Carmichael, *Photon Antibunching and Squeezing for a Single Atom in a Resonant Cavity*, Physical Review Letters **55**, 2790–2793 (1985).

[84] P. Meystre and M. Zubairy, *Squeezed states in the Jaynes-Cummings model*, Physics Letters A **89**, 390–392 (1982).

[85] V. Bužek, H. Moya-Cessa, P. Knight, and S. Phoenix, *Schrödinger-cat states in the resonant Jaynes-Cummings model: Collapse and revival of oscillations of the photon-number distribution*, Physical Review A **45**, 8190 (1992).

[86] C. Savage and H. Carmichael, *Single atom optical bistability*, IEEE Journal of Quantum Electronics **24**, 1495–1498 (1988).

[87] C. Wang and R. Vyas, *Fokker-Planck equation in the good-cavity limit and single-atom optical bistability*, Physical Review A **54**, 4453 (1996).

[88] A. Hutton and S. Bose, *Mediated entanglement and correlations in a star network of interacting spins*, Physical Review A **69**, 042312 (2004).

[89] K. Wodkiewicz and J. Eberly, *Coherent states, squeezed fluctuations, and the SU (2) am SU (1, 1) groups in quantum-optics applications*, JOSA B **2**, 458–466 (1985).

[90] M. Kitagawa and M. Ueda, *Squeezed spin states*, Physical Review A **47**, 5138 (1993).

[91] D. J. Wineland, J. J. Bollinger, W. M. Itano, F. L. Moore, and D. J. Heinzen, *Spin squeezing and reduced quantum noise in spectroscopy*, Physical Review A **46**, R6797–R6800 (1992).

[92] J. Janszky and A. V. Vinogradov, *Squeezing via one-dimensional distribution of coherent states*, Physical Review Letters **64**, 2771 (1990).

[93] A. S. Sørensen and K. Mølmer, *Entanglement and extreme spin squeezing*, Physical Review Letters **86**, 4431 (2001).

[94] D. Møller, L. B. Madsen, and K. Mølmer, *Quantum gates and multiparticle entanglement by Rydberg excitation blockade and adiabatic passage*, Physical Review Letters **100**, 170504 (2008).

[95] T. Opatrný and K. Mølmer, *Spin squeezing and Schrödinger-cat-state generation in atomic samples with Rydberg blockade*, Physical Review A **86**, 023845 (2012).

[96] J. J. Sakurai and J. Napolitano. *Fundamental Concepts*, page 1–65. Cambridge University Press, 2 edition, (2017).

[97] R. J. Glauber, *Coherent and Incoherent States of the Radiation Field*, Physical Review **131**, 2766–2788 (1963).

[98] R. J. Glauber, *Photon Correlations*, Physical Review Letters **10**, 84–86 (1963).

[99] R. J. Glauber, *The Quantum Theory of Optical Coherence*, Physical Review **130**, 2529–2539 (1963).

[100] S. M. Barnett and P. M. Radmore. *Operators and States.* In *Methods in Theoretical Quantum Optics*, pages 34–86. Oxford University Press, (2002).

[101] D. F. Walls and P. Zoller, *Reduced Quantum Fluctuations in Resonance Fluorescence*, Physical Review Letters **47**, 709–711 (1981).

[102] S. Barnett, *General criterion for squeezing*, Optics Communications **61**, 432 – 436 (1987).

[103] V. V. Dodonov, *`Nonclassical' states in quantum optics: a `squeezed' review of the first 75 years*, Journal of Optics B: Quantum and Semiclassical Optics **4**, R1–R33 (2002).

[104] U. L. Andersen, T. Gehring, C. Marquardt, and G. Leuchs, *30 years of squeezed light generation*, Physica Scripta **91**, 053001 (2016).

[105] M. M. Miller and E. A. Mishkin, *Characteristic States of the Electromagnetic Radiation Field*, Physical Review **152**, 1110–1114 (1966).

[106] D. Stoler, *Equivalence Classes of Minimum Uncertainty Packets*, Physical Review D **1**, 3217–3219 (1970).

[107] E. Wigner, *On the Quantum Correction For Thermodynamic Equilibrium*, Physical Review **40**, 749–759 (1932).

[108] K. Husimi, *Some formal properties of the density matrix*, Proceedings of the Physico-Mathematical Society of Japan. 3rd Series **22**, 264–314 (1940).

[109] J. J. Sanchez-Mondragon, N. B. Narozhny, and J. H. Eberly, *Theory of Spontaneous-Emission Line Shape in an Ideal Cavity*, Physical Review Letters **51**, 550–553 (1983).

[110] J. I. Cirac, R. Blatt, A. S. Parkins, and P. Zoller, *Preparation of Fock states by observation of quantum jumps in an ion trap*, Physical Review Letters **70**, 762–765 (1993).

[111] V. Peano and M. Thorwart, *Quasienergy description of the driven Jaynes-Cummings model*, Physical Review B **82**, 155129 (2010).

[112] L. S. Bishop, E. Ginossar, and S. M. Girvin, *Response of the Strongly Driven Jaynes-Cummings Oscillator*, Physical Review Letters **105**, 100505 (2010).

[113] R. Gutiérrez-Jáuregui and H. J. Carmichael, *Dissipative quantum phase transitions of light in a generalized Jaynes-Cummings-Rabi model*, Physical Review A **98**, 023804 (2018).

[114] P. Alsing, D.-S. Guo, and H. J. Carmichael, *Dynamic Stark effect for the Jaynes-Cummings system*, Physical Review A **45**, 5135–5143 (1992).

[115] J. Ma, X. Wang, C.-P. Sun, and F. Nori, *Quantum spin squeezing*, Physics Reports **509**, 89–165 (2011).

[116] R. H. Dicke, *Coherence in Spontaneous Radiation Processes*, Physical Review **93**, 99–110 (1954).

[117] B. Lücke, J. Peise, G. Vitagliano, J. Arlt, L. Santos, G. Tóth, and C. Klempt, *Detecting multiparticle entanglement of Dicke states*, Physical Review Letters **112**, 155304 (2014).

[118] F. T. Arecchi, E. Courtens, R. Gilmore, and H. Thomas, *Atomic coherent states in quantum optics*, Physical Review A **6**, 2211–2237 (1972).

[119] J. J. . Bollinger, W. M. Itano, D. J. Wineland, and D. J. Heinzen, *Optimal frequency measurements with maximally correlated states*, Physical Review A **54**, R4649–R4652 (1996).

[120] V. Giovannetti, S. Lloyd, and L. Maccone, *Quantum-Enhanced Measurements: Beating the Standard Quantum Limit*, Science **306**, 1330–1336 (2004).

[121] M. A. Rashid, *The intelligent states. I. Group-theoretic study and the computation of matrix elements*, Journal of Mathematical Physics **19**, 1391–1396 (1978).

[122] B. Yurke, S. L. McCall, and J. R. Klauder, *SU(2) and SU(1,1) interferometers*, Physical Review A **33**, 4033–4054 (1986).

[123] J. Schwinger. *Quantum mechanics of angular momentum. A collection of reprints and original papers, Editors LC Biedenharn and H. van Dam*, (1965).

[124] M. Born and V. Fock, *Beweis des adiabatensatzes*, Zeitschrift für Physik **51**, 165–180 (1928).

[125] M. V. Berry, *Quantal phase factors accompanying adiabatic changes*, Proceedings of the Royal Society of London. A. Mathematical and Physical Sciences **392**, 45–57 (1984).

[126] F. Wilczek and A. Zee, *Appearance of Gauge Structure in Simple Dynamical Systems*, Physical Review Letters **52**, 2111–2114 (1984).

[127] M. A. Rashid, *The intelligent states. II. The computation of the Clebsch–Gordan coefficients*, Journal of Mathematical Physics **19**, 1397–1402 (1978).

[128] D. M. Meekhof, C. Monroe, B. E. King, W. M. Itano, and D. J. Wineland, *Generation of Nonclassical Motional States of a Trapped Atom*, Physical Review Letters **76**, 1796–1799 (1996).

[129] D. Kienzler, H.-Y. Lo, V. Negnevitsky, C. Flühmann, M. Marinelli, and J. P. Home, *Quantum Harmonic Oscillator State Control in a Squeezed Fock Basis*, Physical Review Letters **119**, 033602 (2017).

[130] M. V. Berry, *Transitionless quantum driving*, Journal of Physics A: Mathematical and Theoretical **42**, 365303 (2009).

[131] R. Gutiérrez-Jáuregui and H. J. Carmichael, *Quasienergy collapse in the driven Jaynes–Cummings–Rabi model: correspondence with a charged Dirac particle in an electromagnetic field*, Physica Scripta **93**, 104001 (2018).

[132] F. F. Fang and P. J. Stiles, *Effects of a Tilted Magnetic Field on a Two-Dimensional Electron Gas*, Physical Review **174**, 823–828 (1968).

[133] T. Ando, A. B. Fowler, and F. Stern, *Electronic properties of two-dimensional systems*, Reviews of Modern Physics **54**, 437–672 (1982).

[134] K. M. Yunusova, D. Konstantinov, H. Bouchiate, and A. D. Chepelianskii, *Coupling between Rydberg states and Landau levels of Eeectrons trapped on liquid helium*, Physical Review Letters **122**, 176802 (2019).

[135] E. Collin, W. Bailey, P. Fozooni, P. G. Frayne, P. Glasson, K. Harrabi, M. J. Lea, and G. Papageorgious, *Microwave Saturation of the Rydberg States of Electrons on Helium*, Physical Review Letters **89**, 245301 (2002).

[136] A. Blias, R.-S. Huang, A. Wallraff, S. M. Girvin, and R. J. Schoelkopf, *Cavity quatum electrodynamics for superconducting electrical circuits: An architecure for quatum computation*, Physical Review B **69**, 062320 (2004).

[137] S. Haroche and J.-M. Raimond, *Exploring the quatum: atoms, cavities and photons*, Oxford University Press (2006).

[138] G. Baym, *Lectures on quantum mechanics*, Westview Press (1969).

[139] M. Dykman, D. Konstantinov, K. K., and M. J. Lea, *Ripplonic Lamb shift for electrons on liquid helium*, Physical Review Letters **119**, 256802 (2017).

[140] D. Konstantinov and K. Kono, *First study of intersubband absorption in electrons on helium under quantizing magnetics fields*, Journal of the Physical Society of Japan **82**, 043601 (2013).

[141] C. I. Zipfel, T. R. Brown, and C. C. Grimes, *Measurements of the velocity autocorrelation time in two-dimensional electron liquid*, Physical Review Letters **37**, 1760 (1976).